Tuning Strong Correlated Properties in $EuTiO_3$ Thin Films Grown by Pulsed Laser Deposition

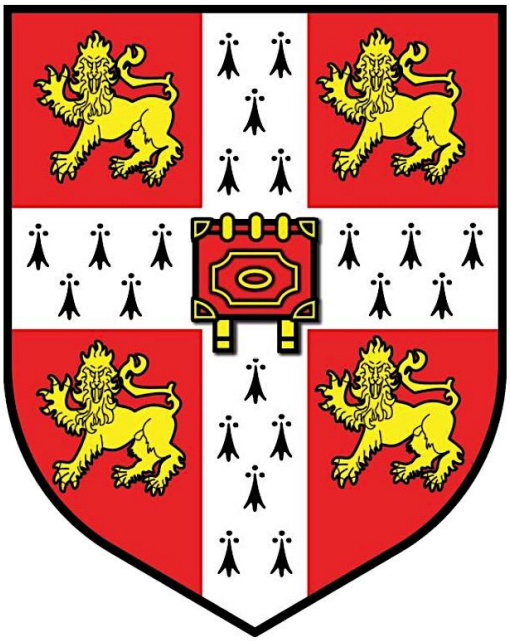

Yisong Lin

Jesus College

Department of Materials Science and Metallurgy

University of Cambridge

This dissertation is submitted for the degree of

Doctor of Philosophy

March 2019

For my beloved family

Declaration

I hereby declare that this dissertation, submitted for the degree of Doctor of Philosophy at the University of Cambridge, is a result of my own work carried out between October 2014 and January 2019 at the Device Materials Group, Department of Materials Science and Metallurgy, University of Cambridge under the supervision of Prof. Judith L. MacManus Driscoll.

No part of this dissertation has been submitted for a degree to this, or any other university and institution. This dissertation is my own work and includes nothing which is the outcome of work done in collaboration except as specified and referenced in the text.

The length of this dissertation is within the limit of 60,000 words.

Yisong Lin

March 2019

Cambridge, UK

Abstract

Tuning Strong Correlated Properties in $EuTiO_3$ Thin Films Grown by Pulsed Laser Deposition

Yisong Lin

Transition metal ABO_3 perovskite oxides possess many fascinating and technologically relevant phenomena such as superconductivity, multiferroicity, magnetoresistivity, and photovoltaics. To achieve and enhance these existing functionalities in perovskite oxides, control and tailor of strong coupling between structural degrees of freedom and correlated order parameters is required. One typical example of decently tuned functionalities in transition metal is perovskite $EuTiO_3$ (ETO). This compound has attracted intensive attention for achieving ferromagnetic-ferroelectric (or multiferroic) and magnetoelectric coupling via strain engineering. Besides phase transition induced by strain engineering, there is an increasing interest in exploring the magnetocaloric effect (MCE) in ETO-based bulk materials.

First, systematic studies for optimizing the growth condition for ETO-based self-assembled vertically alligned nanocomposite (VAN) thin films were carried out. We carried out investigations for finding a suitable binary oxide second phase to incoporate with ETO. It was challenging since the growth condition suitable for growing ETO would not always be compatible with that of the binary oxide. After various exploration, $(ETO)_{0.5}$-$(Eu_2O_3)_{0.5}$ was successfully fabricated on (0 0 1)-oriented STO under careful control of growth pressure, substrate temperature and laser repetition rate. The optimized growth condition (laser repletion rate of 3 Hz, substrate temperature of 710 ^oC and growth pressure of $1\text{-}2\cdot10^{-6}$ Torr) was confirmed to make the $(ETO)_{1-x}$-$(Eu_2O_3)_x$ (x = 0.2, 0.25, 0.33, 0.5) epitaxial thin film on STO substrate with preferred OOP orientation. Next, by controlling the molar ratio of Eu_2O_3 (EO) in $EuTiO_3$ (ETO) VAN films, from 20% to 50% (20%, 25%, 33% and 50%), vertical strain and hence local structure and magnetic properties were systematically changed in ETO. Using scanning transmission electron microscopy and atomic simulations, the Eu-Ti-Eu bond angle change along {111} direction was determined as a function of EO fraction and hence vertical strain level. On-going from 20 to 50% EO, the vertical strain was changed from 2.48% to 3.15%, and the Eu-Ti-Eu bond angle was decreased by more than 1^o to 178.70^o, leading to a progressive weakening of the antiferromagnetic interactions along {111} direction. This structural change caused the magnetic moment (*M*, measured at 2K, 500 Oe) to be

decreased from 5.15 μ_B /Eu to 1.46 μ_B /Eu and the coercivity filed (H_c) to be increased from 5.74 Oe to 26.23 Oe. At the same time, the ETO switched from being antiferromagnetic to ferromagnetic. Density functional theory calculations confirmed that the magnetism in ETO being modified by vertical strain. Moreover, giant magnetic entropy change ($-\Delta S_m$ = 31.4 J/kg·K at ΔH = 2T) was observed in $(ETO)_{0.8}$-$(Eu_2O_3)_{0.2}$ VAN thin film, which is higher than the literature reported single crystal bulk ETO or polycrystal bulk ETO. Finally, Gd-doped ETO, $Eu_{1-x}Gd_xTiO_3$ (x=0.3, 0.5), thin films were made and found to be ferromagnetic. The valence states change of Ti ions were demonstrated using XPS, showing that 13.41% (x=0.3) and 34.59% (x=0.5) of extra electrons were bonded to Ti^{4+} effectively. FM in $Eu_{1-x}Gd_xTiO_3$ (x = 0.3, 0.5) thin films was explained by magnetic interactions between localized Eu^{4+} 4f spins mediated by itinerant Ti 3d electrons (introduced by Gd doping).

Acknowledgments

Many people have been walked alongside me during my time in Cambridge, my dissertation could not have been completed without their help. I would like to thank every one of them.

Firstly, I would like to express my sincere gratitude to my supervisor, Professor Judith MacManus-Driscoll, for having offered me the opportunity to work on this project.

Special thanks to my graduate tutor and Jesus College, supports have always come in the moment of need through my entire journey.

Many thanks to Ping Lu (Sandia National Lab, U.S.), Xing Sun and Haiyan Wang (Purdue University, U.S.) for a collaboration providing TEM and STEM micrography. I am grateful to Jiawang Hong and Chao Yang (Nanjing University of Aeronautics and Astronautics, China) for a collaboration providing DFT calculations.

I am very grateful to Cambridge Commonwealth Trust and China Scholarship Council without whose financial support this work would not have been possible. Thanks to Cambridge Commonwealth Trust for extra funding because of extended duration of this work.

Within the Department of Materials Science and Metallurgy, I am grateful to the help from Dr. Ahmed Kursumovic and Dr. Nadia Stelmashenko for their technical supports in fixing broken lab equipment. Thanks to Ms. Mary Vickers and Mr. Andrew Moss for their supports in XRD. Precious help from Dr. Josee Kleibeuker and Dr. Ady Suwardi during my initial stages of this work will never be forgotten. Special thanks to Dr. Eun-Mi Choi, Dr. Weiwei Li for sharing their help and knowledge on VAN structure and magnetism. Thank you to Dr. Rui Wu for your support and discussions on the magnetocaloric effects. Thank you to Dr. Tuhin Maity for discussion on the strain-driven magnetic phase transition part. Thank you to Bonan Zhu for helping me in the beginning stage of setting up the Atomap tool. I would like to thank my friends and colleagues, especially Chao Yun, Tiesheng Wang, Zeyu Deng, and Jingwei Wang, for sharing great moments during my last few years.

Finally, thank you to my family because they don’t need a reason to be thanked for.

Contents

List of Abbreviations

AF	Antiferromagnetic
BE	Binding Energy
DC	Direct Current
EO	Eu_2O_3
ETO	$EuTiO_3$
FE	Ferroelectric
FM	Ferromagnetic
GTO	$GdTiO_3$
IP	In-plane
LSAT	$(La_{0.3}Sr_{0.7})(Al_{0.65}Ta_{0.35})O_3$
MBE	Molecular Beam Epitaxy
MCE	Magnetocaloric Effect
MOVPE	Metalorganic Vapor Phase Epitaxy
MS	Magnetron Sputtering
OOP	Out-of-plane
PE	Paraelectric
PDOS	Partial Density of States
PLD	Pulsed Laser Deposition
RSM	Reciprocal Space Map
$RTiO_3$	Rare Earth (orthorhombic) Titanates
SAED	Selected Area Electron Diffraction
SQUID	Superconducting Quantum Interface Device
STEM	Scanning Transmission Electron Microscopy
STO	$SrTiO_3$
T_c	Curie Temperature
T_N	Neel Temperature
TEM	Transmission Electron Microscopy
VAN	Vertically Aligned Nanocomposite
VASP	Vienna ab initio simulation package

XPS	X-ray Photoemission Spectroscopy
XRD	X-ray Diffraction
3D	Three Dimensional

List of Tables

List of Figures

Chapter 1. Introduction

Transition metal ABO_3 perovskite oxides possess many fascinating and technologically relevant phenomena such as superconductivity, multiferroicity, magnetoresistivity, and photovoltaics [1–4]. The wide variety of composition, as well as diverse structure induced by partial substitution and non-stoichiometry, provides a platform for researchers from vast fundamental and applied areas to explore the novel functionalities and understand the mechanism hidden behind. To achieve and enhance these existing functionalities in perovskite oxides, control and tailor of strong coupling between structural degrees of freedom and correlated order parameters is required. Chemical pressure [5–7] and biaxial strain [8–13] engineering have been widely applied to manipulate the spin, charge and orbital orderings, allowing one to enhancing and engineering functionalities in perovskite.

One typical example of decently tuned functionalities in transition metal is perovskite $EuTiO_3$ (ETO). ETO is a paraelectric (PE) and antiferromagnetic (AF) [14] with a strong spin-lattice coupling. This compound has attracted intensive attention for achieving ferromagnetic-ferroelectric and magnetoelectric coupling via strain engineering [15,16]. Through control of the magnetism of ETO by an electric field, ETO could be a promising candidate for novel storage devices [17–19]. Density functional theory (DFT) calculations proposed that by applying compressive strain ($\geq$ -1.2%), ETO can be changed from PE-AF phase into a ferroelectric (FE, spontaneous polarization, ~10$\mu C/cm^2$)-ferromagnet (FM, spontaneous magnetization, ~7 μ_B /Eu) [15]. These values are orders of magnitude higher than any known FE or FM materials and are at the same level as for materials that are solely ferroelectric or ferromagnetic, which makes ETO one of the most promising candidates for strain-tuned physical properties.

Besides phase transitions induced by strain engineering, there is an increasing interest in exploring the magnetocaloric effect (MCE) in ETO-based bulk materials in recent years [20–28]. Because they are very promising low temperature (T = 1-40K) magnetic refrigeration materials showing large adiabatic temperature change and magnetic entropy changes under low magnetic field and low temperature cryogenic system and quantum computing. There could also be specific technological applications such as, space science and liquefaction of hydrogen in fuel industry.

In this work, the ETO is revisited from an entirely new point of view-using 3D strain engineering instead of biaxial strain engineering. We demonstrate realizing phase transitions (AF to FM) and giant magnetic entropy changes in ETO using vertical strain. Furthermore, the magnetic properties change in ETO is investigated using chemical pressure induced by Gd doping.

1.1 Aims and objectives of this work

This work focuses on creating novel three-dimensional (3D) strain in ETO-based VAN thin films to achieve phase transitions and to unveil the fundamental mechanisms determining the magnetic ground states of ETO. Enhanced giant magnetic entropy change is also achieved in ETO-based VAN thin films, as compared to its bulk form. Moreover, by doping Gd into ETO (introducing itinerant electron), FM is realized in the otherwise AF ETO.

1.2 Overview

This work of tuning the strong correlated properties in ETO *via* 3D strain and chemical strain will be presented in this thesis as follows:

Chapter 1: *Introduction.*

Chapter 2: *Literature review*. This chapter gives a detail introduction on rare earth titanates and VAN structures. Magnetic phase transitions in ETO (realized by biaxial strain, volume expansion, and chemical doping), magnetic interactions in ETO, and magnetocaloric effect (MCE) in bulk ETO are also reviewed in detail in this chapter.

Chapter 3: *Experimental methods*. This chapter includes all the experimental method undertaken.

Chapter 4: *Results and discussion: Optimizing the growth of ETO-based VAN thin films*. The growth of ETO-based VAN by pulsed laser deposition (PLD) is reported. The different compositions that were explored are detailed, i.e. the reasons for these compositions and the results achieved in them. Optimization of growth conditions are presented. Eu_2O_3 (EO) is shown to produce the best achieve ETO-based VAN thin films.

Chapter 5: *Results and discussion: 3D strain-induced magnetic phase transition in ETO using VAN structure and giant cryogenic magnetic entropy changes in* $(ETO)_{0.8}$-$(EO)_{0.2}$ *VAN films*. 3D

strain-induced magnetic phase transitions are reported. Also, the mechanisms of magnetic ground state change are investigated. Magnetic entropy changes in $(ETO)_{1-x}$-$(EO)_x$ (x = 0.2, 0.5) films are investigated. Giant cryogenic magnetic entropy changes in $(ETO)_{0.8}$-$(EO)_{0.2}$ is reported.

Chapter 6: *Results and discussion: Magnetic properties of $Eu_{1-x}GdTiO_3$ (x=0.3, 0.5, 1) thin films*. The growth of $Eu_{1-x}GdTiO_3$ (x=0.3, 0.5, 1) thin films is reported. The strain states and magnetic properties of these films are reported. Valence states differences are investigated.

Chapter 7: *Conclusion and Future work*. In this chapter, the conclusions of the thesis and suggestion for future research are included.

1.3 Publication

Vertical strain-driven antiferromagnetic to ferromagnetic phase transition in $EuTiO_3$ nanocomposite thin films. Yisong Lin, Eun-Mi Choi, Ping Lu, Xing Sun, Rui Wu, Chao Yun, Bonan Zhu, Haiyan Wang, Weiwei Li, Tuhin Maity, Judith MacManus-Driscoll. *ACS Appl. Mater. Interfaces* **2020**. https://doi.org/10.1021/acsami.9b17887.

Chapter 2. Literature Review

2.1 Vertically aligned nanocomposite (VAN) epitaxial films

Many fascinating and technological relevant phenomena such as, superconductivity, multiferroicity, magnetoresistivity and photovoltaics [1–4] have been found in the strong correlated electron materials in the form of transition metal ABO_3 perovskite oxides. In this family, type 'A' atom, usually alkaline earth or rare-earth elements sit at the corners of the lattice, type 'B' atom, could be 3d, 4d and 5d transition metal elements, lies at the body center of the lattice and oxygen atom occupies face center position. This wide variety of composition, as well as diverse structural tunability, has enabled transition metal perovskite oxides to hold an unparalleled variety of physical properties. Comparing to traditional electronic materials, where only charge (semiconducting electronic) or charge and spin (spintronic) is active, strong correlated electron materials in the form of transition metal ABO_3 perovskite oxides offer additional lattice and orbital degrees of freedom, leading to giant responses to subtle extrinsic perturbations in such as, temperature, electric or magnetic field, or mechanical strain.

Much effort has been put into controlling and tailoring the couplings between structural degrees of freedom and correlated order parameters in transition metal perovskite oxides to achieve enhanced and novel functionalities. The modern development of thin film technology such as pulsed laser deposition (PLD) has enabled to impose epitaxial strain (from chosen substrates) onto thin film materials. In thin film materials, the strains induced by substrates are usually an order of magnitude higher than in which these materials would crack in the form of bulk. This has also led to the discovery of new phases, structures, and properties of these materials. For instance, in the study of ferroelectric materials (in which the polarization-strain coupling is strong), the Curie temperature (T_c) of $SrTiO_3$ (a material that is not ferroelectric at any temperature in its bulk form) tuned by a biaxial strain of order 1% has reached to room temperature [8]. This example also made the record of largest-ever reported enhancement of ferroelectric Curie temperature by inducing strain.

Another example lies in the strain tuning of magnetic properties in transition metal perovskite oxides. The A-B bond environment and d orbit polarization can be altered using substrate-induced strains, which would result in different thin films' magnetic properties comparing to their bulk

counterparts. Since magnetic ordering and transition temperature of transition metal ABO_3 perovskite oxides are in close relation with B-O lengths and B-O-B angles [6,29], tuning octahedral distortions and rotations in ABO_3 oxide thin films can engineer magnetism in them. Researchers have found that substrate-induced strain can significantly alter magnetic properties by suppressing ferromagnetism and altering the stability of magnetic ground states. Magnetic properties of mixed-valence manganites have been an interesting topic since they possess multiple magnetic ground states and competition between neighboring phases in phase diagrams can cause colossal responses [30]. Numerous studies have demonstrated the effect of strain on $La_{0.7}Sr_{0.3}MnO_3$ thin film's magnetic properties. In 2009, D.G. Schlom [31] demonstrated $La_{0.7}Sr_{0.3}MnO_3$ grown on different substrates, which applied biaxial strains ranging from -2.3% to 3.2%. These strain effects on T_c of $La_{0.7}Sr_{0.3}MnO_3$ thin film found out to have excellent agreement with Millis' analytical model, which demonstrated the effects of biaxial strain on the T_c of colossal magnetoresistance manganites were caused by lattice distortion on the Jahn-Teller splitting and electron hopping amplitude. In another article written by L. Schultz [32], it was suggested that a 0.1% change of strain state in $La_{0.7}Sr_{0.3}MnO_3$ would shift its T_c by 19 K. Besides T_c, strain can also play an irreplaceable role in tuning a film's magnetic anisotropy [33].

When it comes to multiferroism (a material that simultaneously possesses at least two ferroic orders) properties of transition metal ABO_3 perovskite oxide thin films, the couplings between structural degrees of freedom and correlated order parameters become so consequential that properties can be enhanced dramatically by applying appropriate strains. One example is strained-$BiFeO_3$ thin films [34]. $BiFeO_3$ is rhombohedral in its un-strained state (or in its bulk form) [35]. Under an in-plane biaxial compressive strain (the critical compressive strain is around -4.5% predicted by *ab initio calculation* [36] and is realized when $BiFeO_3$ thin film grown upon (110)-oriented $YAlO_3$ substrate [36,37]), $BiFeO_3$ thin films turn from a rhombohedral state to a super-tetragonal state [34,36,37]. When the thin film thickness increases, the epitaxial constraint would partially relax and lead to the formation of a mixed-phase nanostructure that consists both of rhombohedral phases and super-tetragonal phases [34,38–43]. This mixed-phase nanostructure consists of a highly distorted rhombohedral phases which enhances the ferromagnetism [38] in this material significantly (the highly distorted rhombohedral phases is the source of ferromagnetism enhancement is confirmed by a combination of photoemission electron microscopy with x-ray magnetic dichroism contrast and piezoresponse force microscopy images [38]). What is more, by applying an electric field, the

mixed phase would turn back into a super-tetragonal phase; and under a reversal electric field, the super-tetragonal phase would turn into a mixed phase [38].

As mentioned above, strain induced by the substrate has enabled researchers to tune the strong couplings between structural degrees of freedom and correlated order parameters. However, noting that conventional interfacial heterostructures such as superlattice and multilayers are grown in the fashion of layer-by-layer, strain relaxation limits the biaxial strain within a critical thickness and thus prevents the strain further tuning the properties when thin film thickness reaches a certain point (usually a few tens of nanometers). Hindered and inspired by this problem, researchers have come up with a new route, self-assembled vertically aligned nanocomposite [44] as shown in Figure 2.1, to reduce the substrate-clamping effect and enable strong interfacial coupling.

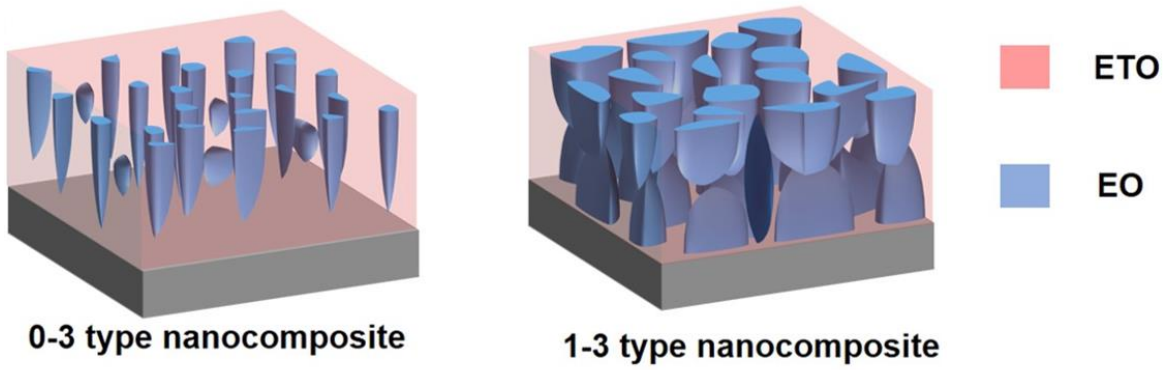

Figure 2.1 Schematic of all-oxide vertically aligned nanocomposites studied in this thesis.

2.1.1 Materials selection criteria of VAN epitaxial films

In order to grow self-assembled VAN thin films, important perspectives like compositional, structural, and processing factors needed to be considered. VAN oxide thin films consist of two intermixed materials as shown in Figure 2.1, grown (most commonly by pulsed laser deposition) on a single crystal substrate from a compound ceramic target.

First thing to be understood is the solubility limit of the respective phases. By careful selection of solid solubility of two phases, the inter-diffusion between two phases can be minimized. MacManus-Driscoll et al. carried out a systematic study on VAN for materials selection and put forward a practical guideline for selecting the two materials to be in VAN films, as follows [45]:

(1) both phases must be able to grow epitaxially on a single crystal substrate;

(2) the two phases involved must be immiscible with each the other;

(3) each of the two phases must be thermodynamically stable to prevent intermixing;

(4) Cations with a large difference in ionic radii are important to prevent intermixing between the two phases;

(5) the difference in elastic modulus is required to achieve strain control on one phase by the other and thus enabling coupling and tuning new properties.

2.1.2 Growth mechanism of VAN epitaxial films

During the deposition process, factors like surface diffusion of clusters, nucleation and film growth need to be considered. At the very early stages of self-assembled VAN thin films growth, different species will arrive at the substrate surface simultaneously and these atoms tend to attach to the substrate, shown in Figure 2.2 (a). In the following stages, atoms will nucleate with lowest energy fashion, which will minimize the free energy of the system, shown in Figure 2.2 (b). Subsequently, owing to the high cohesive energy compared to adhesive energy in both phases, adatoms of one phase will prefer to grow only on the existing same phase. When the thin film grows thicker, the columns of respective phase will be built up, as shown in Figure 2.2 (c), and the width of the columns will be determined by the adatoms' diffusion length on the substrate. For instance, if the difference between the interfacial energy of substrate-vacuum and substrate-island is small, islands with small dimensions will be formed at the initial stage, and the resulting width of phase column will be small. After all, the formed microstructure of the VAN thin films will depend on the materials system (such as volume fraction, elastic moduli and lattice mismatch strain can affect which phase grows into matrix and nanocolumns) and deposition parameters (a common growth window is needed for both phases). Several microstructures have been observed in self-assembled VAN thin films; for example, a perfect checkerboard structure can be obtained by careful materials system selection and growth control, circular columns, rectangular columns, T-shape columns or biaxial domain walls structure can also be performed by tuning thermodynamic parameters, choosing proper substrates and materials selection [46].

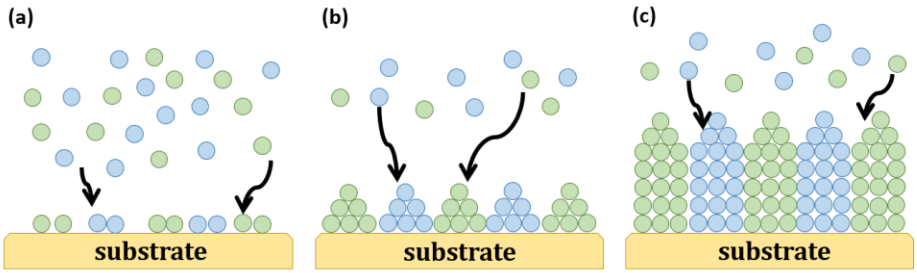

Figure 2.2 Schematic showing the growth process of VAN thin films. (a) Adatoms diffusion. (b) Adatoms growth. (c) Columnar formation.

2.1.3 Functionalities tuned by VAN structure

Since K. Samwer demonstrated the first self-assembled binary phase oxide $(La_{0.7}Ca_{0.3}MnO_3)_{1-x}$-$(MgO)_x$ structure in 2003 [47], the follow-on VAN structures have attracted intense research interest since they exhibit several unique characteristics allowing control and tailoring the functionalities in oxide films, via achieving unique strain states. First, vertical strain can be maintained in both composite phase in VAN structures going beyond the critical thickness that strain provided by the planar structure can give. Second, unique microstructures (columns, rectangle nanodomains) embedded in a matrix can be designed by selecting proper material composites and growth parameters. Third, defects such as oxygen vacancies accumulated at the vertical interface between two phases can be used to tailor functionalities. VAN structures have been reported in various systems showing enhanced functionalities, such as very high ferroelectric T_c [48], strong improved dielectric tunability [49], reducing dielectric loss [50], enhanced multiferroic coupling [51], photostriction-magnetostriction coupling [52], strong enhanced current densities in superconductors [53], new kinds of memristors [54], and strongly enhanced ionic conduction at lower temperature [55]. Three of the functionalities tuned by VAN structure will be introduced in the following paragraphs.

In VAN thin films consisting of $BaTiO_3$ matrix and vertically Sm_2O_3 columns [48], the thin film was grown up to 1.25 μm on $SrTiO_3$ substrate. The ferroelectric T_c was increased at least 330 ^oC and the tetragonal-to-cubic structural transition temperature to beyond 800 ^oC was obtained in this system owing to stiff Sm_2O_3 columns throughout the film thickness. Comparing to horizontal strain induced by the substrate in parallel thin film systems, vertical strain induced by nanocomposite phases throughout the thin film in VAN structure can prevent $BaTiO_3$ from

undergoing deleterious surface reconstruction and allows the system maintaining a stable nanoscale ferroelectric. In other words, there is no degradation of ferroelectricity when the thin films thickness increases.

In VAN thin films containing $Ba_{0.6}Sr_{0.4}TiO_3$ and vertically Sm_2O_3 columns [49], high electric tunability and low dielectric loss were obtained. When the materials system operated from room temperature to above 150 ^oC, high tunability and low-temperature coefficient of tunability still maintained. Tunability values of 75% were achieved at room temperature in micrometer thick films at temperature, while the temperature went up to 160 ^oC, the value remaining still being higher than 50%. Additionally, a dielectric loss value of less than 0.01 was achieved (lower than pure $Ba_{0.6}Sr_{0.4}TiO_3$ thin film).

In La_2CoMnO_6-ZnO VAN thin film systems [51], at the temperatures of 120 K, an electric field applied to the system can alter the magnetic properties of La_2CoMnO_6, as shown in Figure 2.3. In this figure, different positive electric field values were applied to the system at 120K. From 0 to 289 KV/cm, a reduction of the coercive field by 35% is observed. The reductions went further for the larger electric field. When the electric field dropped back to 0 KV/cm, the coercive field went back to high value. Also, from this figure, magnetization value decreased with increasing electric field. From 0 to 305 KV/cm, the reduction of magnetization value was 60% suggesting a magnetoelectric coefficient of $\Delta M/\Delta E$ near 3 Oe/cm/KV.

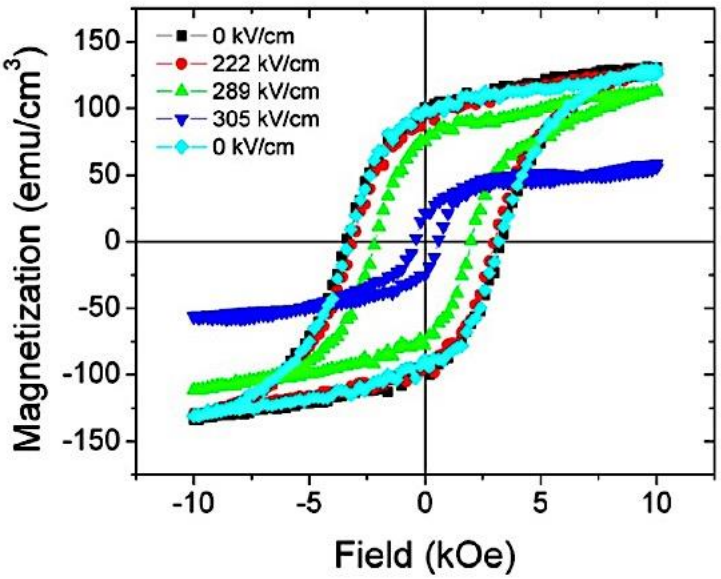

Figure 2.3 Magnetization curves of La_2CoMnO_6-ZnO VAN thin film under different electric fields at 120 K. (Adapted from [51])

For the many different functional enhancements, vertical strain induced by VAN played a significant role in tuning the functionalities of oxide thin films. Compared to planar films, self-assembled VAN structures do not have an intrinsic thickness limitation for strain control. It is because strain in VAN is controlled by large area vertical interfaces than the single interface with the substrate. For typical VAN systems, column diameters are in the value of 20 nm or less, so there is no enough column width to allow full relaxation by misfit dislocation formation. What is more, the recent effort has been made to understand how and why auxetic-like strain effects can be achieved in VAN thin films. Auxetic-like strains were generated in $(Ba_{0.6}Sr_{0,4}TiO_3)_{1-x}$-$(Sm_2O_3)_x$ ($x \leq 0.5$) [56]. For x = 0.25 and 0.5 (as shown in Figure 2.4 (a) and (b)), the *out-of-plane* lattice parameters of $Ba_{0.6}Sr_{0,4}TiO_3$ are increased (compared to that of bulk $Ba_{0.6}Sr_{0,4}TiO_3$) by stiffer Sm_2O_3 nanopillars, while the *in-plane* lattice parameters of $Ba_{0.6}Sr_{0,4}TiO_3$ are increased due to the thermal shrinkage upon cooling after growth ($Ba_{0.6}Sr_{0,4}TiO_3$ is prevented from contracting due to the epitaxial anchoring of the $Ba_{0.6}Sr_{0,4}TiO_3$ to the Sm_2O_3, while Sm_2O_3 pillars can contract freely). For x = 0.75 (as shown in Figure 2.4 (a) and (c)), where soft $Ba_{0.6}Sr_{0,4}TiO_3$ forms the columns (nanopillars) and stiff Sm_2O_3 forms the matrix, the *in-plane* lattice parameters of $Ba_{0.6}Sr_{0,4}TiO_3$ are decreased (compared to its bulk form) due to the thermal shrinkage strain from enveloping (the stiffer Sm_2O_3 matrix squeezes the columns upon cooling after growth), the *out-of-plane* lattice parameter of $Ba_{0.6}Sr_{0,4}TiO_3$ is increased due to compression of its *in-plane* shrinkage, the overall lattice volume of $Ba_{0.6}Sr_{0,4}TiO_3$ is decreased (compared to its bulk form). This work created an unusual auxetic-like strain in the VAN system thus allowing new functional physical properties to be tuned in thin films.

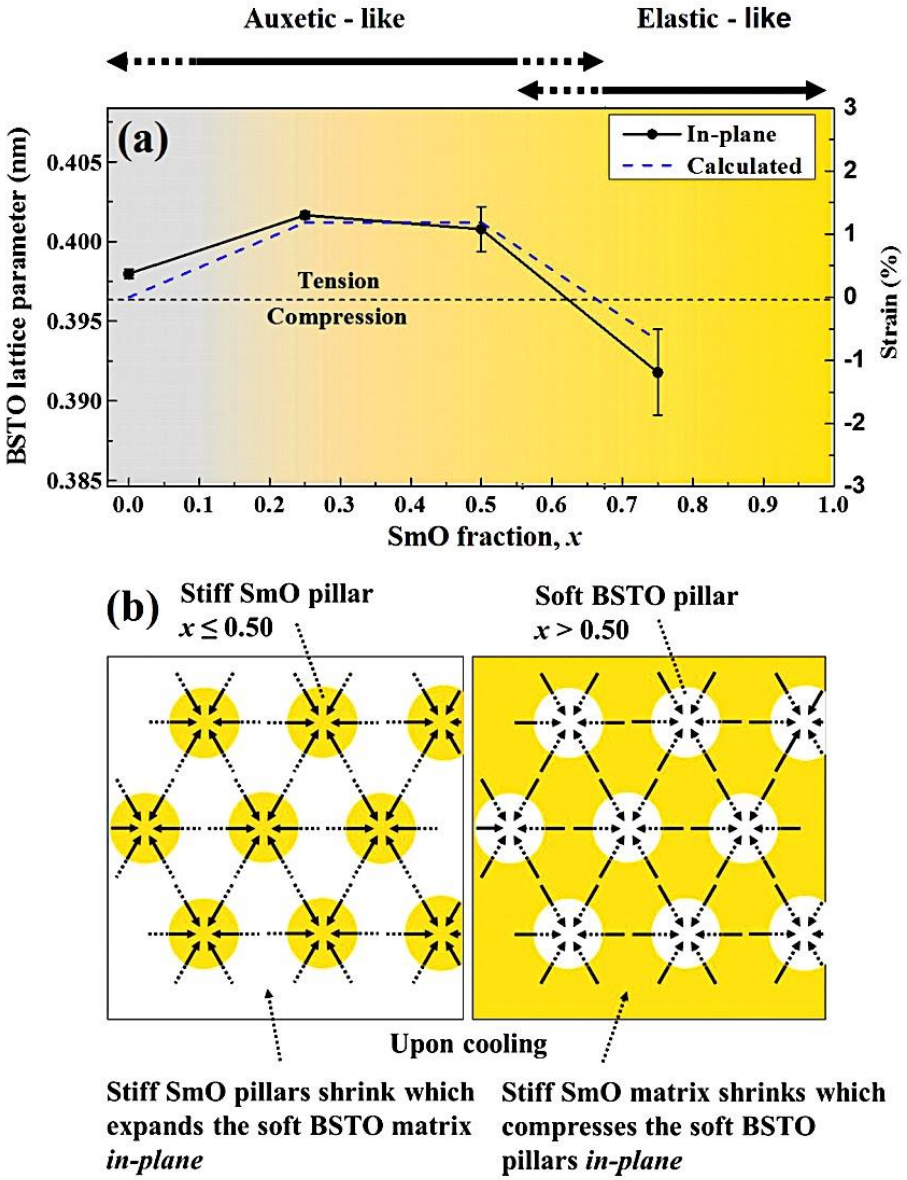

Figure 2.4 Second phase's fraction influences strain type in VAN thin films. (Adapted from [56])

2.2 Rare earth orthorhombic titanates and $EuTiO_3$ (ETO)

The ABO_3 perovskite oxide was first discovered in mineral calcium titanate, $CaTiO_3$, in the Ural Mountains of Russia in 1839 by G. Rose and named after Russian mineralogist L.A. Perovski. The crystal structure of perovskite oxide was first investigated by V. Goldschmidt in 1926[57]. It is also in this work the famous Goldschmidt tolerance factor was proposed to describe the perovskite structure. In 1946, the crystal structure of perovskite oxide was characterized using X-ray diffraction by H.D. Megaw[58].

From the perspective of functional properties, it was in 1950 that G.H. Jonker and J.H. Van Santen discover the ferromagnetic ordering in the $(La_{1-x}Sr_x)MnO_3$ perovskite oxide[59]. In 1986, high Curie T_c superconductivity was reported in the perovskite related cuprates, $La_{5-x}Cu_5O_{5(3-y)}$, by J.G. Bednorz and K.A. Müller [60]. In 1993, colossal negative magnetoresistance was found in $La_{2/3}Ba_{1/3}MnO_x$ by R.von Helmot [61]. In 2003, multiferroicity was realized in bismuth ferrite, $BiFeO_3$, by R. Ramesh [2].

Pursuing functionalities using careful design in perovskite oxides has continued to be an intensive research area. Among various perovskite oxides, titanates possess peculiar physical properties. Multiple ferroic phases, such as ferromagnetic (FM), antiferromagnetic (AF), ferroelectric (FE), quantum paraelectric, and even cross-couplings between them, can be found in perovskite titanates. More recently, rare earth orthorhombic titanates $RTiO_3$ (R = La… Lu or Y, the valence states of the R are 3+) have emerged as a particularly interesting family of Mott insulator [62–65]. While the rare earth cubic titanates $EuTiO_3$ (the valence state of Eu is 2+) have been theoretically predicted [15] and later experimentally confirmed [16] to be FM and FE. In the following sections, we will discuss these two separately.

2.2.1 Rare earth orthorhombic titanates $RTiO_3$ (R = La… Lu or Y, the valence states of the R are 3+)

The rare earth orthorhombic titanates $RTiO_3$ has attracted attention since they are the key materials for investigating the coupling of magnetism and orbitals in strong correlated perovskite oxide. The most stable valence state of Ti in the rare earth orthorhombic titanates system is 3+, which means Ti is in a spin ½ $3d^1$ electronic state. The couplings between spins in the $3d^1$ state and Ti t_{2g} orbitals

result in a variety of orbital-spin phases and phase transitions among them. This unique character has made the rare earth orthorhombic titanates the key class of materials for the understanding of the orbital physics [63].

The crystal structure of $RTiO_3$ is orthorhombic with a $GdFeO_3$-type distortion as shown in Figure 2.5 (a). The $GdFeO_3$-type distortion is induced by the tilting of TiO_6 octahedron around the [110] axis and [001] axis. As the ionic radii of R changes, the magnitude of this distortion changes. For R ion with a small ionic radius, the TiO_6 octahedron tilts (more $GdFeO_3$-type distorted) more significantly and the bond angle of Ti-O-Ti decreases more from 180°. This has a great influence on the subtle competitive exchange interactions in the $RTiO_3$ family. As shown in Figure 2.5 (b), the magnetic ground states of $RTiO_3$ changes from G-type AF (both intra-plane and inter-plane of neighboring atoms are coupled antiferromagnetically) to FM as the ionic radius decreases (and $GdFeO_3$-type distortion increases). It is explained from the perspective of orbital physics [63]. For $RTiO_3$ with strong $GdFeO_3$-type distortion, where R = Gd and Y, FM ground state was shown in these compounds since the electronic structure is dominantly determined by the crystal field from the O ions with large distorted TiO_6 octahedra. The depression of T_N and T_c near the AF-FM phase boundary is observed since both AF and FM states have a two-dimensional anisotropy. For $RTiO_3$ with small $GdFeO_3$-type distortion, where R = La, Ce, Pr and Nd, AF ground state was shown in these compounds since the electronic structure is dominantly determined by the crystal field from the R ions with small distorted TiO_6 octahedra.

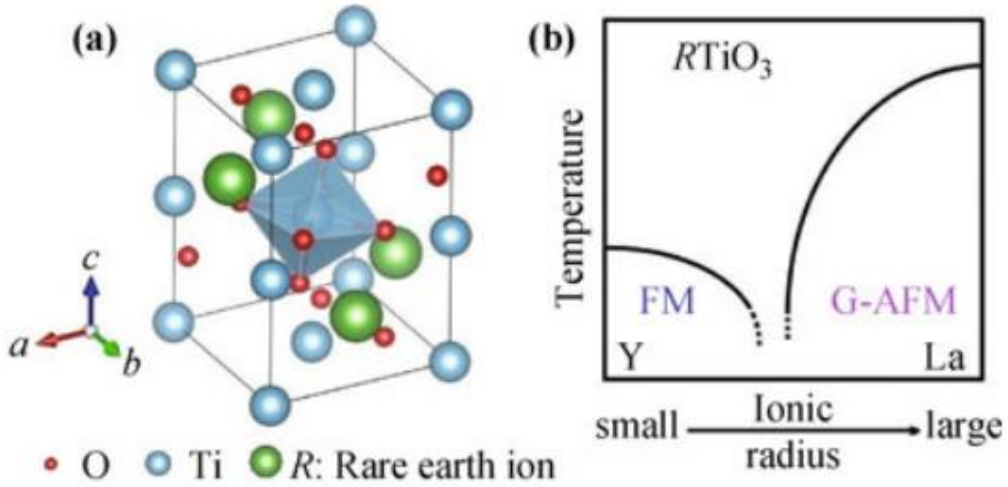

Figure 2.5 (a) Crystal structure of $RTiO_3$ with a $GdFeO_3$-type distortion. (b) Schematic magnetic phase diagram of $RTiO_3$ family. (Adapted from [66])

Though the relative roles of orbital-lattice coupling and structural distortion hidden behind this AF to FM transition is still a debated subject [63,67–70], researchers have tried to control orbital-lattice coupling (and thus the magnetic properties) of this $RTiO_3$ family in their thin film form.

In 2013, S. Stemmer reported the magnetic interactions of $GdTiO_3$ coupled to the TiO_6 octahedral tilts using the $(GdTiO_3)_n/(SrTiO_3)_{13}$ (n=3.5, 2.4, and 2 nm) superlattices samples grown by Molecular Beam Epitaxy (MBE) [71]. The magnetization of the samples *vs* temperature (and magnetic field) is shown in Figure 2.6. The magnetic properties of $GdTiO_3$ in the superlattice structure is different to those in bulk $GdTiO_3$ (or 20nm $GdTiO_3$ thin film), indicating that FM behavior can still present in $GdTiO_3$ superlattice layers even where the distortions are quenched (by TiO_6 distortions in $SrTiO_3$) to magnitudes comparable to those of bulk AF $LaTiO_3$, this results support the direct orbital-lattice coupling. Later in 2018, S. Stemmer reported another result to support this idea [72].

Recently, the study of magnetism in rare earth titanates has attracted much attention not only in the orthorhombic $RTiO_3$ family (mainly AF-FM crossover behavior of the ground states in their bulk materials [68,70] and $GdTiO_3/SrTiO_3$ heterostructures with a mixture of Ti $3d^1/3d^0$ electronic configurations [71,72]), but also in the strain-induced ferroelectric ferromagnetism in $EuTiO_3$ thin films [15,16].

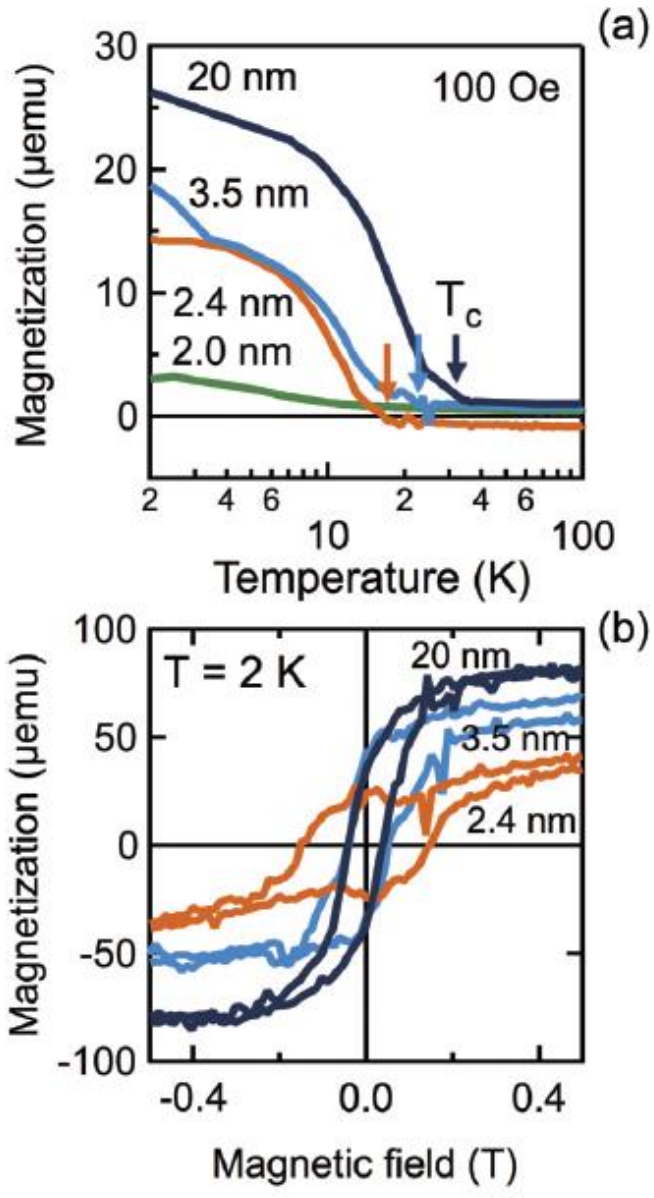

Figure 2.6 (a) Magnetization of $(GdTiO_3)_n/(SrTiO_3)_{13}$ (n=3.5, 2.4, and 2 nm) superlattices samples as a function of temperature. (b) Magnetization of $(GdTiO_3)_n/(SrTiO_3)_{13}$ (n=3.5, 2.4, and 2 nm) superlattices samples as a function of magnetic field. (Adapted from [71])

2.2.2 Rare earth cubic titanate ETO

Different to the orthorhombic $RTiO_3$ family, ETO is cubic perovskite structure with lattice parameters (at room temperature) equal to that of $SrTiO_3$. In ETO, Eu is in the 2+ valence state while the valence state of Ti is 4+.

The first recorded report about ETO was in 1952, E. Banks [73] attempted to substitute Eu^{2+} into the lattice site of the Sr^{2+} or Ba^{2+} in $SrTiO_3$ or $BaTiO_3$, both of them were under intensive investigation for their ferroelectric properties. They chose europium (Eu) since it was the only one which was found to be sufficiently stable in the divalent state among the rare earth elements. Later in 1965, M. W. Shafer [74] carried out susceptibility measurements on ETO to study the magnetic interaction of the Eu^{2+} ion as a function of its crystal structure. In 1966, a more detailed study on the magnetic structure of ETO [75] was carried out by S. J. Pickart. In 1974, the magnetic property of ETO was again studied using the technique of ^{151}Eu Mössbauer spectroscopy by F. De S. Barros [76].

In 2001, under the background discovery of colossal magnetoresistance in perovskite manganites [77], ETO was revisited and the coupling between magnetism and dielectric properties was studied by H. Takagi [14]. In this report, the dielectric constants of ETO were changed under different magnetic field as shown in Figure 2.7. As shown in the inset figure, the change of dielectric constant reached 7% at the magnetic field of 1.5 T. A coupling between the configuration of the Eu spins and a soft-phonon mode in ETO was proposed at the end of this report.

Only a few years later (around 2005), there was a flurry of research interest in multiferroic and magnetoelectric materials [53] since they can combine electronic and magnetic properties into multifunctional materials, which satisfies the needs towards device miniaturization under the big picture of information technology development. However, multiferroic materials are rare. There are several limiting microscopic factors, including symmetry, electronic properties, and chemistry, proposed in articles [78,79] that prevent the simultaneous existence of ferromagnetism and ferroelectricity. From the perspective of symmetry, there are only 13-point groups that allow both spontaneous electric polarization and spontaneous magnetic polarization to exist in a single-phase material. Considering the electrical properties, ferroelectric materials are meant to be insulating while ferromagnetic materials are often metals. However, if taken ferromagnets, weak ferromagnets or antiferromagnets into consideration, these electronic property restrictions no longer hold. What is more, common perovskite ferroelectric oxides possess B cations (in ABO_3 perovskite oxide) that have a formal d^0 electronic state while d^0 electronic state means that there is no d electron to create localized magnetic moments; magnetic ordering of any type would no longer exists.

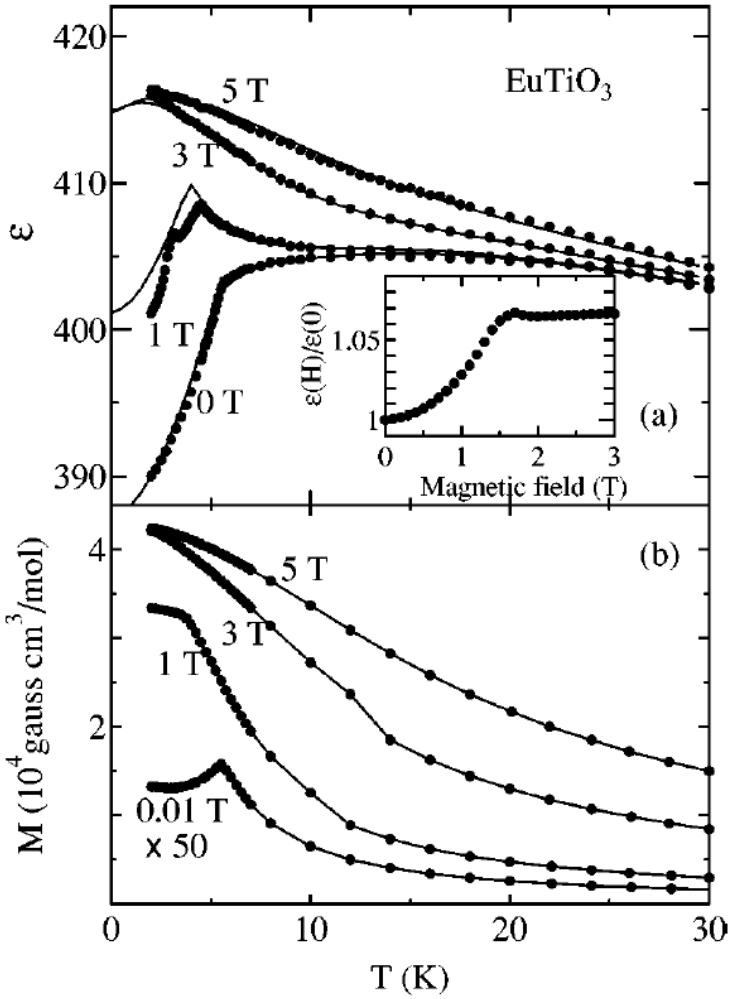

Figure 2.7 (a) Dielectric constants of ETO under different magnetic field. (b) Magnetization *vs* temperature under different magnetic fields. Inset shows the dielectric constant of ETO (normalized to the value at zero field) under different magnetic field at the temperature of 2K. (Adapted from [75])

The need of multiferroic materials, or more precisely, magnetoelectric materials (the magnetization of these materials could be tuned by the electric field or vice versa) with stronger coupling effects, had pushed researchers to investigate thin film materials (possess unique characters which are not found in their bulk counterparts). As mentioned before, strain plays an important role in tuning the strong couplings between structural degrees of freedom and correlated order parameters of the thin films. In 2006, C. J. Fennie and K. M. Rabe [15] proposed a design

strategy basing on the coupling of spins, optical phonons, and strain for achieving magnetoelectricity (or FM-FE multiferroicity) in ETO. By using first-principles density-functional theory calculation, they suggested that under biaxial compressive strain, ETO can transform from a dielectric antiferromagnetic insulator (bulk properties) into a strong FE (spontaneous polarization, ~ 10 μC/cm^2) - FM (spontaneous magnetization, ~7 μ_B) multiferroic material. The compressive epitaxial strain phase diagram of calculated results of ETO is shown in Figure 2.8. The spontaneous polarization and magnetization values were orders of magnitude higher than any known FE-FM materials and were at the same level as for materials that are solely FE or FM.

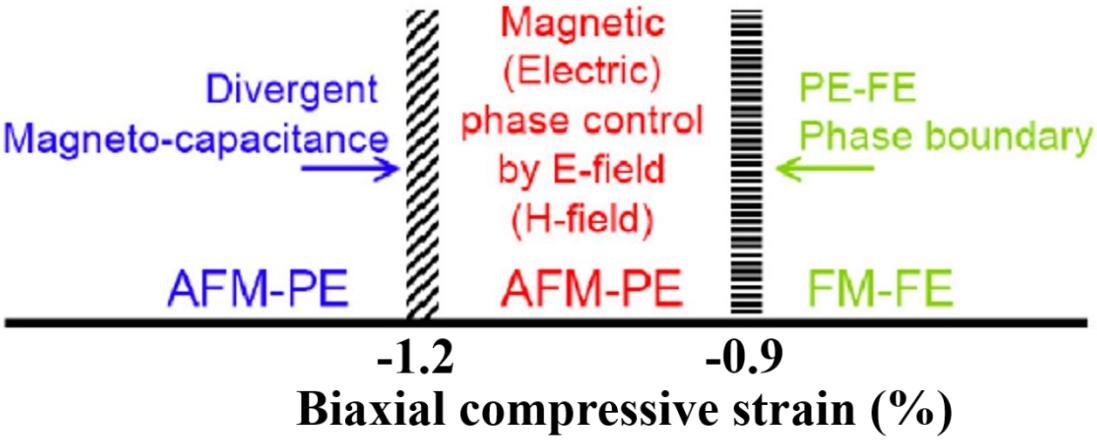

Figure 2.8 Compressive epitaxial strain phase diagram of ETO. (Adapted from [15])

To verify the theory calculation and make strained-ETO FM-FE, experimental work was carried out. However, to achieve the compressive strain boundary (critical value is around -1.2% compressive strain) in ETO was difficult due to lack of an appropriate substrate while maintaining a high-quality crystalline ETO. In 2010, D. G. Schlom [16] changed the strategy by extending the phase diagram to biaxial tensile strain region using density-functional theory calculation. The extended biaxial strain phase diagram of ETO is shown in Figure 2.9. In this article, 22nm of ETO films were grown on (0 0 1)-oriented $(La_{0.3}Sr_{0.7})(Al_{0.65}Ta_{0.35})O_3$ (LSAT), (0 0 1)-oriented $SrTiO_3$ and (1 1 0)-oriented $DyScO_3$ substrates, which induced biaxial strain of -0.9% (compressive strain), 0% and +1.1% (tensile strain), respectively. A FM-FE phase was realized in ETO grown on (1 1 0)-oriented $DyScO_3$ substrates (with FE T_c =250K and FM T_c =4.24K). A year later, an estimated polarization of 29 μC/cm^2 strained-ETO (+1.1% tension) was given by D. G. Schlom in addendum

in some journal. To the best of our knowledge, direct measurement of ferroelectric hysteresis loop and electric field control of magnetism on the 22nm strained-ETO thin film (+1.1% tension) are yet to be done, possibly due to the leakage issues.

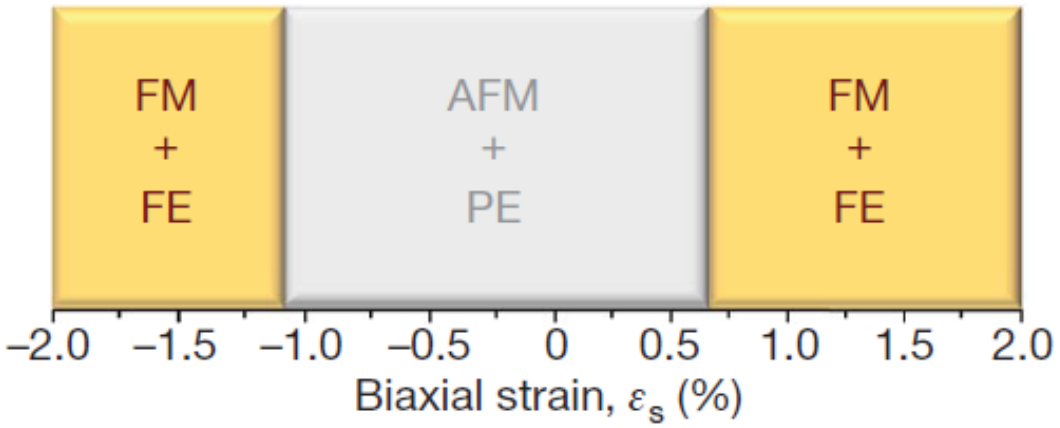

Figure 2.9 Phase diagram of ETO strained from -2% (biaxial compression) to +2% (biaxial tension). (Adapted from [16])

Before 2013, Researchers had been led to believe that it was necessary to have proposed strain-induced polar instability [15,16] to realize a dramatic magnetoelectric effect in ETO thin films until D. G. Schlom discovered that even under moderate compressive strain state (-0.9% compressive strain) ETO could be tuned into the FM region under proper electric field [80]. This unexpected result suggested the exploring the magnetic interactions and underlying mechanism of emergent FM in strained ETO films would be critical to fully understand the mechanisms of electrical field-controlled magnetism in ETO. Efforts made from this perspective will be reviewed in next section.

2.3 Tuning magnetic phase transition in ETO

Bulk or unstrained ETO thin film shows AF with a T_N of around 5.5 K [76,81]. Previous experimental works have reported that the magnetic ground state of ETO could be switched to FM by biaxial strain, volume expansion, and electric field.

2.3.1 Strain from substrate

In the last section, a 22nm ETO film grown on (1 1 0)-oriented $DyScO_3$ substrate [16] exhibited clear FM behavior with T_c at around 4.2K as shown in Figure 2.10. The transition to FM region was explained a spin-phonon-driven destabilization of the lattice (strain) induced FM phase with a low-lying state competing with AF [15]. Comparing to proposed spontaneous magnetization of $7\mu_B$ in strain-induced FM ETO [15], the magnetization in this ETO on $DyScO_3$ thin film showed only around $3\mu_B/Eu^{2+}$. This missing moment phenomenon was later explained by local magnetic inhomogeneity in the strained film [82].

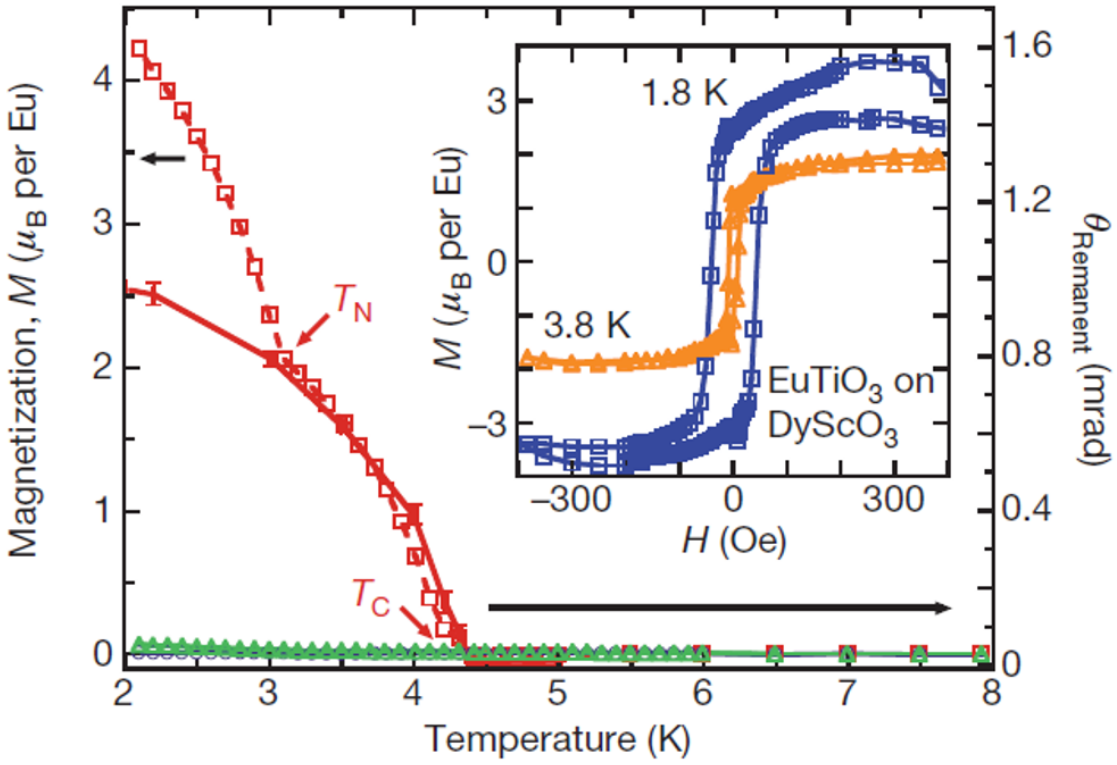

Figure 2.10 Temperature dependence of the magnetization for ETO on $DyScO_3$ measured by MOKE and SQUID. Inset shows isothermal SQUID magnetization curves. (Adapted from [16])

2.3.2 Volume expansion

ETO was switched from AF to FM when grown on $LaAlO_3$, $SrTiO_3$ and $DyScO_3$ substrates [83]. Large lattice volume expansions of 1.56%, 2.41% and 3.92% were caused by the lattice mismatch between ETO and the substrates. Clear FM behaviors could be observed in this series of samples

as depicted in Figure 2.11. In this report, it was further suggested that in C. J. Fennie and K. M. Rabe's calculation work [15], the biaxial compressive strain was introduced in the surface of ETO films while the lattice volume was kept constant, so the lattice was elongated in the out-of-plane direction. A correlation between the strain or the lattice volume and the magnetic structure was thus proposed. Based on the hybrid Hartree-Fock density function theory calculation, indirect exchange interactions via 5*d* states of Eu^{2+} changed from AF interaction to FM interaction as the lattice volume increased and thus induced FM in the volume expanded-ETO.

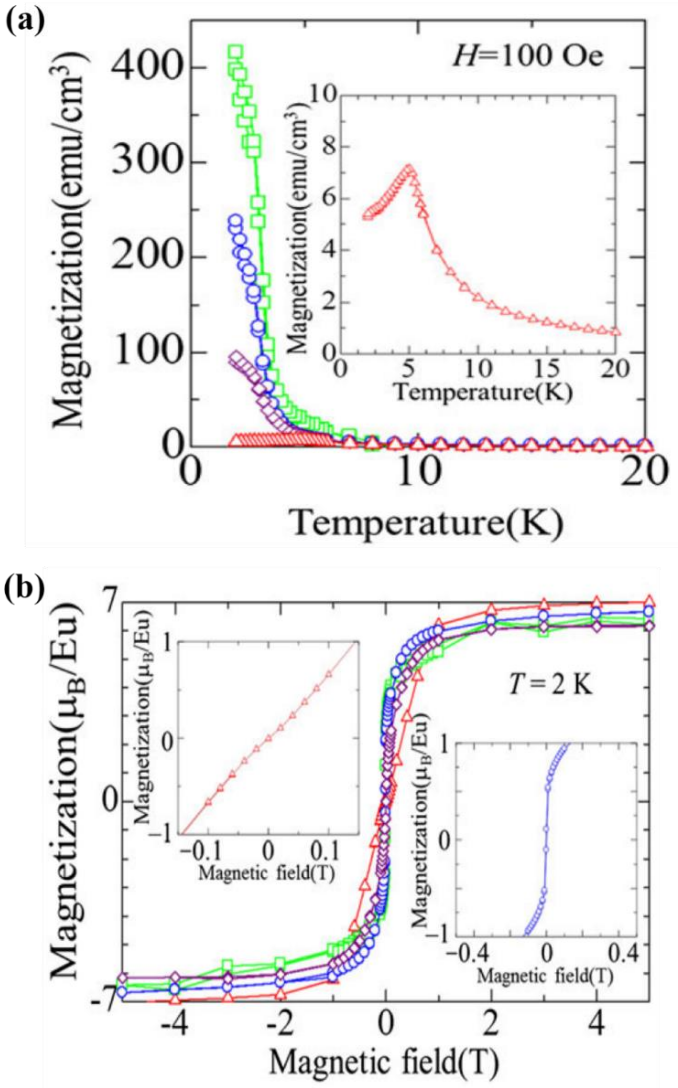

Figure 2.11 (a) Temperature dependence and (b) Magnetic field dependence of magnetization for ETO grown on $LaAlO_3$ (diamond), $SrTiO_3$ (circle) and $DyScO_3$ (square) substrates. Triangle curve for bulk ETO. (Adapted from [83])

2.3.3 Electric field

Under moderate compressive strain, an applied filed was found to eliminate long-range AF order in ETO films grown on (0 0 1)-oriented LSAT substrate, inducing a magnetic state with nanometer-sized FM clusters [80]. In this article, X-ray resonant magnetic scattering was used to determine the magnetic structure of ETO. Without an electric field, compressive strained (-0.9%, not reaching the critical compressive strain value of -1.2% as mentioned above) ETO grown on LSAT showed AF character with T_N of 4.96 K as shown in Figure 2.12 (a). With an increasing electric field, the AF signature in compressive strained ETO was suppressed and finally eliminated by an electric field of 10^5 V/cm as shown in Figure 2.12 (b). It was suggested in this article that by applying the electric field, the Ti atom position could be changed thus affecting superexchange interaction between the third nearest neighbor Eu ions, which in turn change the balance of coexisting FM and AF strength in ETO. In other words, by applying a large electric field, the Ti atom position was shifted, superexchange interaction between the third nearest neighbor Eu ions was weakened, thus AF order dissipated, and FM interaction emerged.

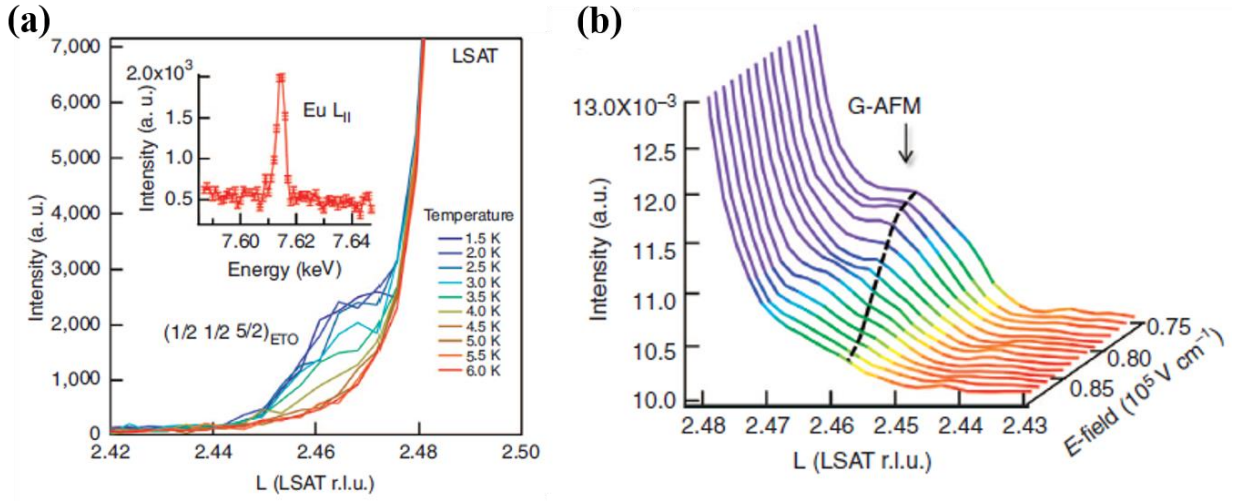

Figure 2.12 (a) X-ray resonant magnetic scattering showing G-type AF order in compressive strained ETO film grown on LSAT. (b) Electric field control of the magnetic state for ETO grown on LSAT. With an increasing electric field, AF signature was suppressed and finally eliminated. (Adapted from [80])

2.3.4 Magnetic interactions in ETO

Theory calculations were carried out to explain and understand the above-mentioned FM ETO. Different scenarios were used for explaining the FM phase obtained in ETO, and there is no clear consensus of its origin. The earlier opinion was strain-induced polar instability that pushes the ETO into the FM region [15]. Later, magnetic interactions between first nearest neighbor Eu ion was considered critical in determining the magnetic ground states of ETO [84,85], and this opinion was used to explain the FM induced by volume expansion [83]. More recently, the superexchange interaction between third nearest-neighbor Eu ion was proposed to explain the FM emergence induced by electric field [80].

Except for the strain-induced polar instability proposal, others indicated that there co-exists both AF and FM interaction in the bulk ETO or un-strained ETO, and by applying either lattice change (strain or volume expansion) or electric field, the balance of AF and FM could be tuned and thus giving different magnetic ground states. As shown in Figure 2.13, there are three major magnetic interactions [80] co-existing in the un-strained ETO: 1^{st} nearest neighbour (1^{st} NN) refers to AF interaction, 2^{nd} nearest neighbour (2^{nd} NN) refers to FM interaction (Eu^{2+} -Eu^{2+} indirect exchange), 3^{rd} nearest neighbour (3^{rd} NN) refers to AF interaction (Eu^{2+}-Ti-Eu^{2+} superexchange *via* Ti 3d states). DFT calculations have proposed that the AF interaction can originate from superexchange interactions between Eu^{2+} ions via Ti^{4+} ions which play a crucial role in switching ETO from AF to FM [84]. Inspired by DFT calculations, D.G. Schlom further suggested that the 3^{rd} NN interactions play an unneglectable role in determining the magnetic ground state and that the strength of the superexchange interaction relies upon the bond angle and the bond length of Eu-Ti-Eu along the {111} direction. Based on this scenario, they realized the switching of magnetism from AF to FM by the application of an electric field [80].

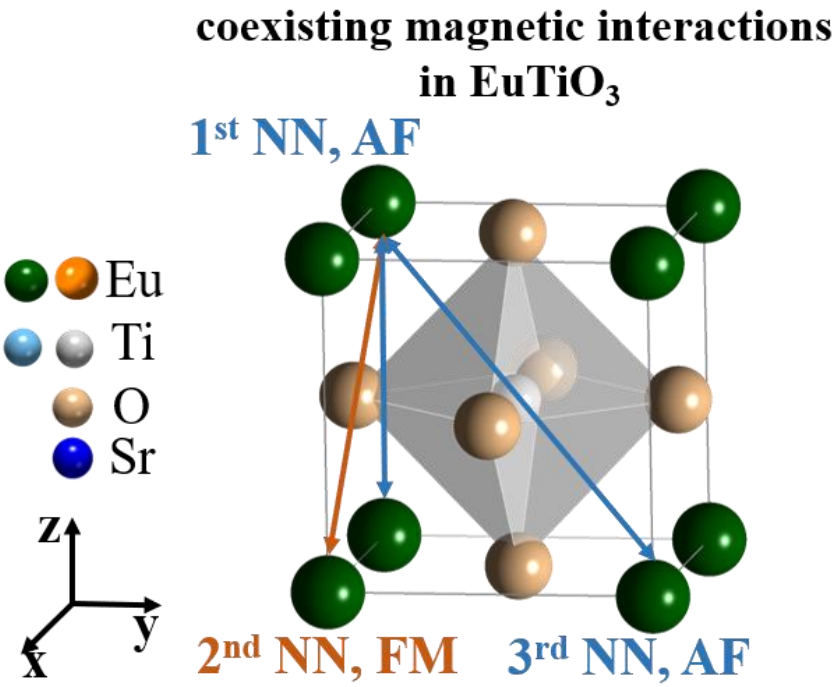

Figure 2.13 Schematic of magnetic interactions in $EuTiO_3$. 1st nearest neighbour (1st NN) refers to AF interaction, 2nd nearest neighbour (2nd NN) refers to Eu^{2+}-Eu^{2+} indirect exchange (FM interaction), 3rd nearest neighbour (3rd NN) refers to Eu^{2+}-Ti-Eu^{2+} superexchange *via* Ti 3*d* band (AF interaction).

2.4 Magnetocaloric effects (MCE) in ETO

The magnetocaloric effect (MCE) is an isothermal magnetic-entropy change or an adiabatic temperature change of a magnetic material under a magnetic field [86]. When the applied magnetic field increases, the magnetic entropy in the magnetic system decrease, heat radiates from the magnetic system into the environment isothermally. When the applied magnetic field decreases, the magnetic entropy in the magnetic system increase, heat is absorbed from the environment into the magnetic system isothermally [87].

It was widely accepted that the MCE was first experimentally observed by E. Warburg in 1881 [88]. However, according to recent reports [89,90], E. Warburg did not discovered magnetocaloric effects since he ascribed the observed irreversible heating to magnetic hysteresis. A. Smith [89] pointed out that the observation of heat evolved in iron samples subject to a varying magnetic field

started in 1843 and widely accepted by the 1880s. It was also in this report [89] that they argued that P. Weiss and A. Piccard were the first experimentally discovered the MCE effect by observing a sizable and reversible temperature change in nickel near its Curie temperature. In 1933, W. F. Giauque and D. P. MacDougall [91] achieved temperatures below 1K by using the magnetic refrigeration technique (basing on MCE effect). Nowadays, magnetic refrigeration has become an effective method to achieve ultralow temperatures. In 1976, G. V. Brown [92] demonstrated magnetic refrigeration near room temperature by using gadolinium (Gd). In 1997, V. K. Pecharsky and K. A. Gschneidner [93] discovered an extremely large magnetic entropy change (or giant MCE) in $Gd_5(Si_2Ge_2)$ (phase transition temperature at 276K), showing that magnetic cooling can compete with vapor compression technology. This discovery has attracted interest because of great potential impact on energy savings and environmental concerns.

2.4.1 The thermodynamics of MCE

In this section, a brief description of how to define the MCE will be given [87,94]. The total differential of the Gibbs free energy *G* of a system in relation with volume *V*, magnetic field *H*, pressure *P* at temperature *T* is given as,

$$dG = VdP - SdT - MdH \tag{1}$$

where *S* is the entropy of the system. Based on this standard thermodynamics' equation, the Maxwell relation can be obtained (since we are not applying pressure, $VdP = 0$) as,

$$\Delta S\,(T,H) = S(T,H) - S(T,H=0) = \int_0^H \left(\frac{\partial M}{\partial T}\right)_H dH \tag{2}$$

where *M* is the magnetization. By this equation, the entropy change (ΔS) can be calculated from measured magnetic data. Noting that experimental magnetic data is usually discrete, the numerical approach can be described as,

$$\Delta S = \sum_i \frac{M_{i+1} - M_i}{T_{i+1} - T_i} \Delta H_i \tag{3}$$

Alternatively, when the material's heat capacity (*C*) is measured (usually temperature dependent), the entropy change can be calculated by:

$$\Delta S\ (T, H, P) = \int_0^T \frac{(C_{H,P} - C_{0,P})}{T} dT \quad (4)$$

where $C_{H,P}$ and $C_{0,P}$ are the heat capacities in the magnetic field H and zero under constant pressure P. The adiabatic temperature change (ΔT_{ad}) is another parameter that used in describing the MCE of a material and can be given by differentiate entropy in the standard thermodynamic equation:

$$dS = (\frac{\partial S}{\partial T})_{H,P}\ dT + (\frac{\partial S}{\partial H})_{T,P}\ dH + (\frac{\partial S}{\partial P})_{T,H}\ dP \quad (5)$$

When dS =0 under adiabatic condition, the adiabatic temperature change is:

$$dT = -\frac{T}{C_{H,P}} \left(\frac{\partial M}{\partial T}\right)_{H,P} dH \quad (6)$$

where $C_{H,P} = T(\frac{\partial S}{\partial T})_{H,P}$ denotes heat capacity. By integrating Equation 6 from magnetic field H =0 to H, ΔT_{ad} could be obtained.

The method described above is one of the indirect methods of obtaining values of isothermal ΔS and adiabatic ΔT_{ad}. The other indirect method to obtain values of isothermal ΔS is the Clausius-Clapeyron method, it should be noted that this method only applied to materials with first-order transition. Besides indirect methods, quasidirect methods (such as heat-capacity and heat-flux methods) are available for obtaining the values of ΔS. More details about the Clausius-Clapeyron method and quasidirect methods can be found in a well written review [90].

2.4.2 MCE in bulk ETO

Since 2014, there is an increasing interest in exploring the magnetocaloric effect in ETO-based bulk materials, such as $EuTiO_3$ [20,21], $Eu_{1-x}Ba_xTiO_3$ [22], $Eu_{1-x}La_xTiO_3$ [23], $Eu_{1-x}Sr_xTiO_3$ [24], $EuTi_{1-x}Cr_xO_3$ [25], $EuTi_{1-x}Nb_xO_3$ [26], $EuTi_{1-x}Fe_xO_3$ [27], $EuTi_{0.9}V_{0.1}O_3$ [28]. Since they are very promising at low temperature (temperature range 1 - 40K) magnetic refrigeration materials showing large adiabatic temperature changes and magnetic entropy changes under low magnetic field. They could be used for basic research, such as cryogenic systems, and specific technological applications, such as space science and liquefaction of hydrogen in fuel industry.

In 2012, theorical calculations were carried out to investigate the MCE on ETO [95]. Experimentally, magnetic entropy changes in $Eu_{1-x}Ba_xTiO_3$ ($0.1 \leq x \leq 0.9$) [22] polycrystalline samples

were reported in 2014, as shown in Figure 2.14. A giant magnetic entropy change $-\Delta S_m$ = 36.12 J/kg·K was observed in $Eu_{0.9}Ba_{0.1}TiO_3$ sample at 4.5 K under magnetic field change ΔH = 5 T. This value is higher than the maximum value reported in Eu-based materials and $RTiO_3$ (R= Dy, Ho, Er, Tm, Yb) series.

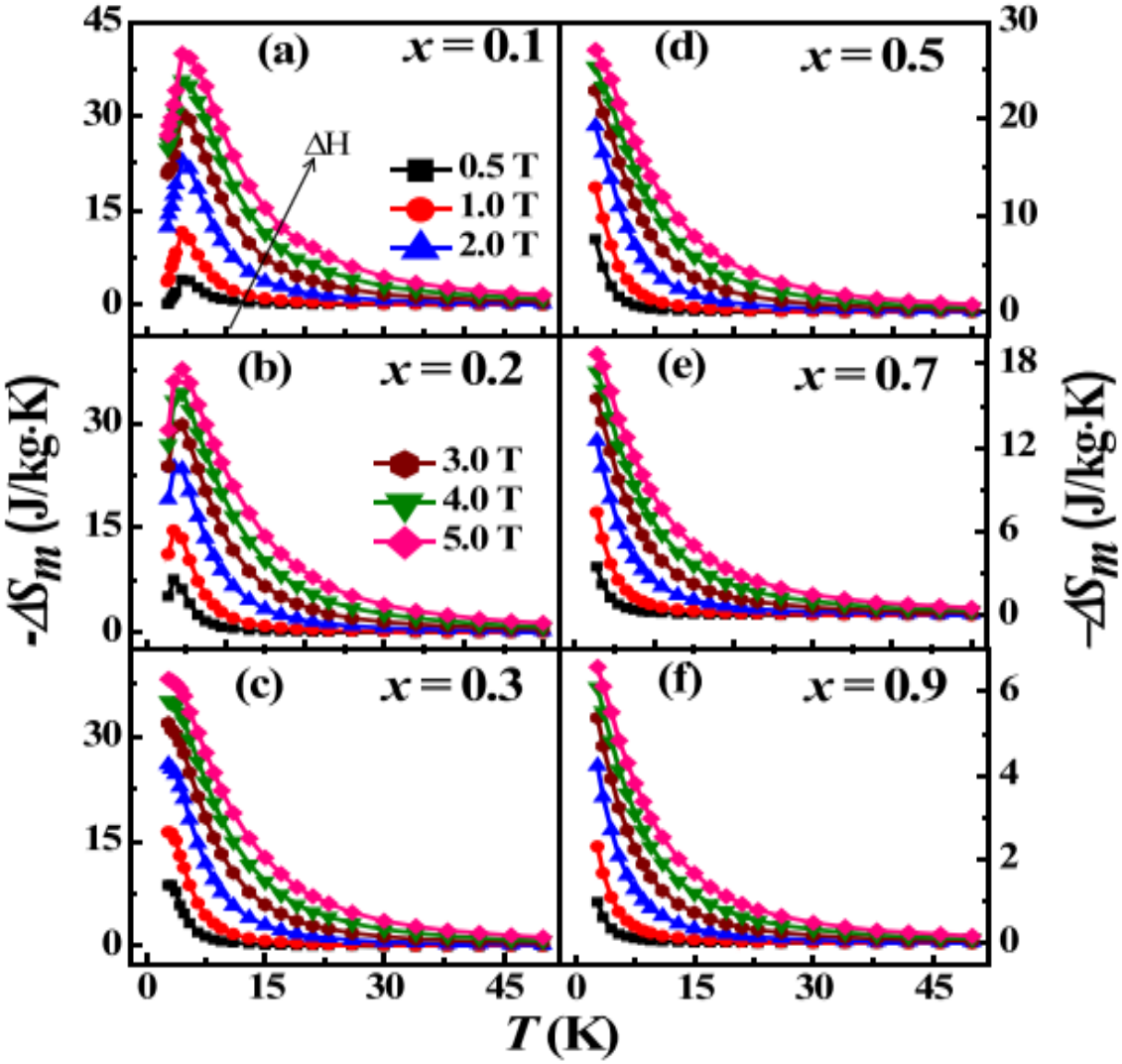

Figure 2.14 Magnetic entropy change ($-\Delta S_m$) under different temperature for $Eu_{1-x}Ba_xTiO_3$ (a) x=0.1, (b) 0.2, (c) 0.3, (d) 0.5, (e) 0.7, and (f) 0.9 for a magnetic field change of ΔH= 0.5, 1, 2, 3, 4, and 5T. (Adapted from [22])

In 2015, B. G. Shen [20] reported a giant reversible MCE effect in ETO, as shown in Figure 2.15. A giant magnetic entropy change $-\Delta S_m$ = 44.4 J/kg·K at 5.5 K under magnetic field change ΔH = 5T was reported. A large refrigerant capacity (*RC*) of 328 J/kg under magnetic field change ΔH = 5T was calculated using $RC = \int_{T_1}^{T_2} \Delta Sm\, dT$ (where T_1 and T_2 were the temperatures at half maximum of peak of $-\Delta S_m$-T curves). In the same year, MCE in $EuTi_{1-x}Cr_xO_3$ (x=0, 0.02, 0.04,0.1) was also investigated by B. G. Shen [25]. Interestingly, with more Cr^{3+} ions substituting Ti^{4+}, Eu^{2+} ions were changed to Eu^{3+}, under magnetic field changes, ΔH = 5 T, the maximum values of $-\Delta S_m$ reached 40.3 J/kg·K for ETO, 40.3 J/kg·K for $EuTi_{0.98}Cr_{0.02}O_3$, 36.2 J/kg·K for $EuTi_{0.96}Cr_{0.04}O_3$ at 5.5 K and 30 J/kg·K for $EuTi_{0.9}Cr_{0.1}O_3$ at around liquid helium temperatures.

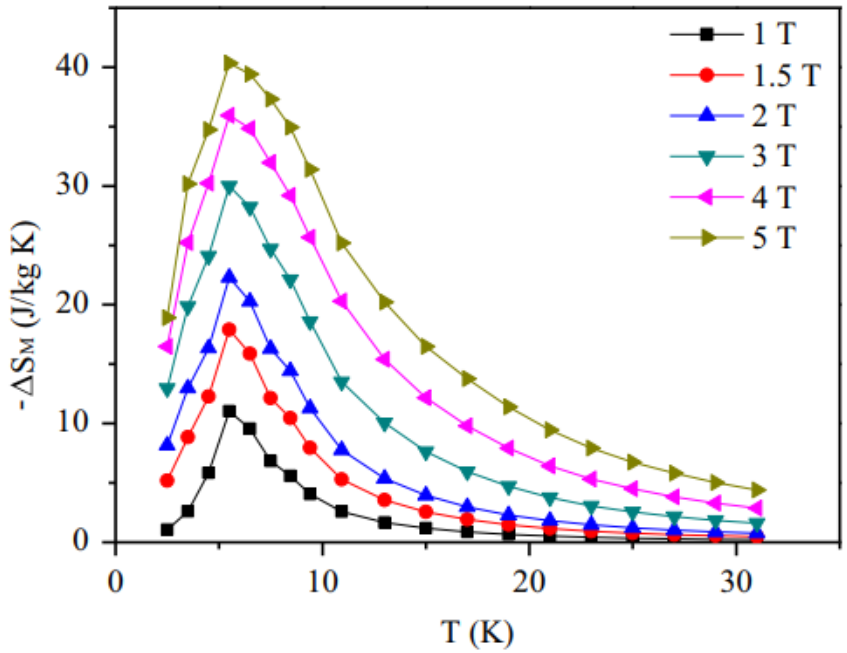

Figure 2.15 Temperature dependence of magnetic entropy change for ETO. (Adapted from [20])

In 2016, R. Mahendiran [21] reported MCE in both single and polycrystalline ETO. Different to previous reports, this report added a mean field treatment of the Heisenberg model and fitted the experimental data of magnetic entropy change for single crystal ETO, as shown in Figure 2.16. A giant magnetic entropy change $-\Delta S_m$ = 42.4 J/kg·K, adiabatic temperature change ΔT_{ad} = 16.6 K and refrigerant capacity *RC* = 353 J/kg at 5.6 K under magnetic field change ΔH = 5 T was reported in single crystal ETO; Magnetic entropy change $-\Delta S_m$ = 40.4 J/kg·K, adiabatic temperature change

ΔT_{ad} = 16.5 K and refrigerant capacity RC = 300 J/kg at 5.4 K under magnetic field change ΔH = 5 T was reported for polycrystalline ETO. Comparing these values to the values obtained from EuO, $DyTiO_3$ and metal-organic framework $Gd(HCOO)_3$, they suggested that ETO could be a great candidate for a refrigerant material below 40K.

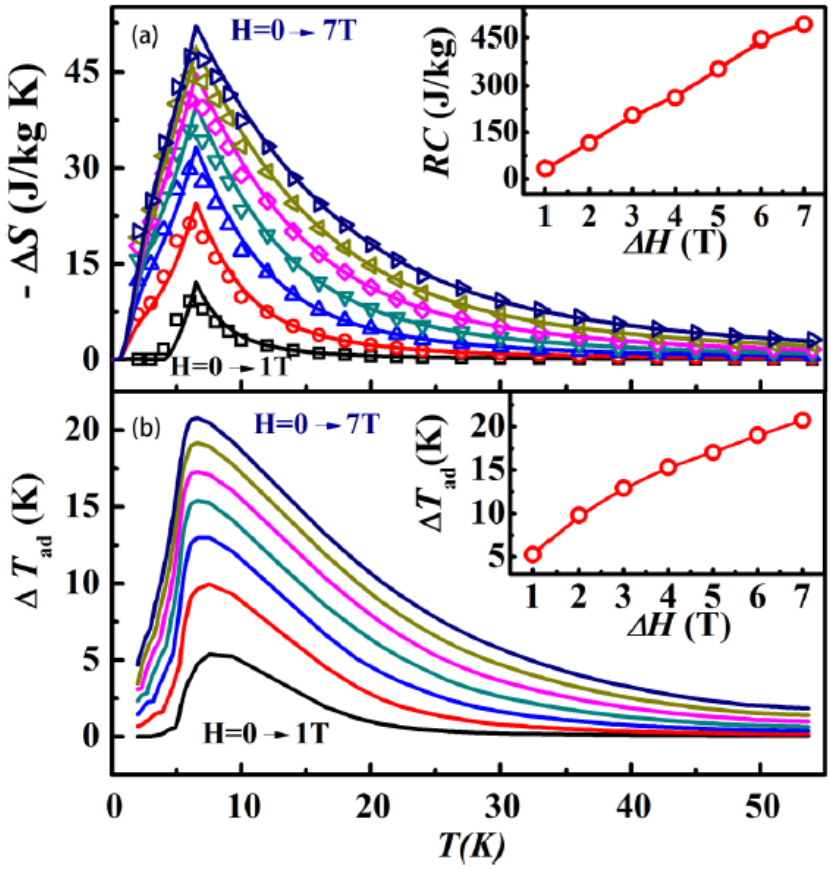

Figure 2.16 (a) Temperature dependence of magnetic entropy change for single crystal ETO. Symbols are calculated from magnetization data; Solid lines are calculated from mean field theory. Inset: Refrigerant capacity as a function of magnetic field. (b) Temperature dependence of adiabatic temperature change for single crystal ETO. Inset: Maximum values of adiabatic temperature change as a function of magnetic field. (Adapted from [21])

Similar reports on MCE in ETO-based materials have been carried out on $Eu_{1-x}La_xTiO_3$ [23], $Eu_{1-x}Sr_xTiO_3$ [24], $EuTi_{1-x}Nb_xO_3$ [26], $EuTi_{1-x}Fe_xO_3$ [27], $EuTi_{0.9}V_{0.1}O_3$ [28]. The reported ETO-based compounds show large magnetic entropy change in low temperature range. There are compounds

other than oxides show large (giant) magnetic entropy change near (or away from) room temperature range, such as Gd [96], $Gd_5Si_2Ge_2$ [93], $Gd_5Si_1Ge_3$ [97], MnAs [98], $MnFeP_{0.45}As_{0.55}$ [99], $Ni_{52.6}Mn_{23.1}Ga_{24.3}$ [100], $Ni_{50}Mn_{37}Sn_{13}$ [101], $Ni_{50}Mn_{34}In_{16}$ [102], $CoMnSi_{0.95}Ge_{0.05}$ [103], $MnCoGeB_{0.02}$ [104], $LaFe_{11.7}Si_{1.3}$ [105] and $LaFe_{11.57}Si_{1.43}H_{1.3}$ [105]. A summarization of selected ETO-based materials and other selected materials (not oxides, but also show large or giant magnetic entropy change near their magnetic transition temperature) are listed below (Table 2.1). From this comparation, we can see that ETO-based compounds are promising low temperature magnetic refrigeration materials showing large magnetic entropy change under low magnetic field change.

Table 2.1 Comparing the ETO-based compounds with materials showing large (giant) magnetic entropy change.

Compound	T_N/T_c **(K)**	$-\Delta S_m$ **(J/kg·K)** (ΔH **= 5 T)**	**Reference**
$EuTiO_3$	5.7	40.4	[20]
$EuTiO_3$	5.4	40.4	[21]
$Eu_{0.8}Ba_{0.2}TiO_3$	2.8	35	[22]
$Eu_{0.8}La_{0.2}TiO_3$	7.5	31.4	[23]
$Eu_{0.9}Sr_{0.1}TiO_3$	5.7	37.8	[24]
$EuTi_{0.9}Cr_{0.1}O_3$	9.7	30	[25]
$EuTi_{0.85}Nb_{0.15}O_3$	9.5	36.3	[26]
$EuTi_{0.9}Fe_{0.1}O_3$	6	31	[27]
$EuTi_{0.9}V_{0.1}O_3$	4.54	36	[28]
Gd	294	11	[96]
$Gd_5Si_2Ge_2$	276	14.8	[93]
$Gd_5Si_1Ge_3$	136	68	[97]
MnAs	318	32	[98]
$MnFeP_{0.45}As_{0.55}$	310	18	[99]
$Ni_{52.6}Mn_{23.1}Ga_{24.3}$	300	18	[100]
$Ni_{50}Mn_{37}Sn_{13}$	299	19	[101]
$Ni_{50}Mn_{34}In_{16}$	190	12	[102]
$CoMnSi_{0.95}Ge_{0.05}$	215	9	[103]
$MnCoGeB_{0.02}$	287	47.5	[104]
$LaFe_{11.7}Si_{1.3}$	184	30	[105]
$LaFe_{11.57}Si_{1.43}H_{1.3}$	291	11	[105]

2.4.3 MCE in thin film and nanocomposite structure

MCE in thin films have drawn considerable attention since it is very interesting from the perspective of understanding the basic phenomena and tailoring the performance. In 1989, the first MCE in thin film was reported in Fe_2O_3 films by E. V. Babkin and Kh. O. Urinov [106]. In 1996, A. L. Micheli [107] reported the MCE in 2.4 *um* thick $La_{0.67}M_{0.33}MnO_3$ (M= Ca, Ba, Sr) films on $LaAlO_3$ substrates. The entropy changes in these films were smaller than the values of their bulk counterparts. The reduction of magnetic entropy change accompanied with enhanced temperature width in thin films was later explained by a combination of finite size effects and defects when materials were scaled down. Similar phenomena were observed in Gd films [108], Gd/W multilayers on MgO substrate [109] and $Gd_5(Si, Ge)_4$ thin films [109].

As mentioned before, strain plays an important role in tailoring thin films' functionalities. Investigations on strain's tuning the MCE in thin film have been carried out. In 2005, E. E. Fullerton [110] reported MCE in FeRh films grown on (0 0 1)-oriented Al_2O_3 and (0 0 1)-oriented MgO substrates. Different transition temperatures were observed since films on MgO in a different strain state.

In 2008, V. H. Etgens [86] investigated the impact of anisotropic strain on the MCE of MnAs. MnAs thin films (~70 nm thickness) were grown on (0 0 1)-oriented GaAs and (1 1 1)-oriented GaAs substrates. Different transition temperatures, different maximum magnetic entropy changes and different curve shapes (which would cause different RC since $RC = \int_{T_1}^{T_2} \Delta Sm\, dT$, where T_1 and T_2 were the temperatures at half maximum of peak of ΔS_m-T curves) were observed as shown in Figure 2.17.

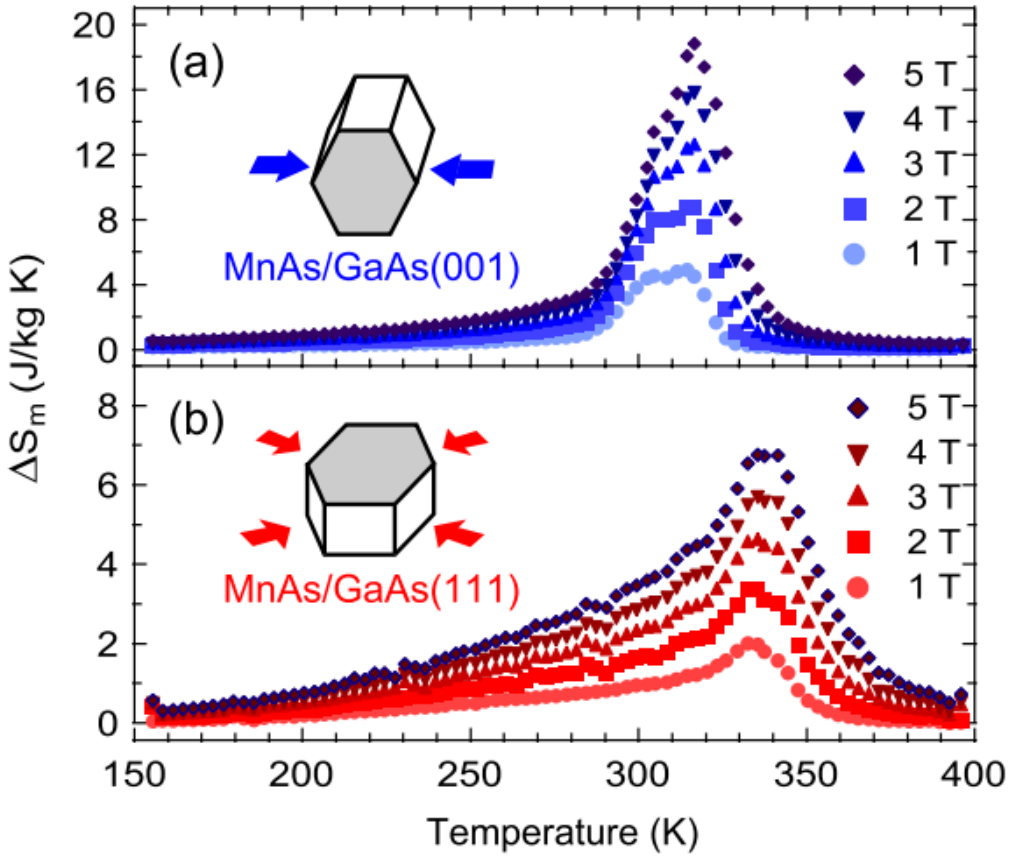

Figure 2.17 Temperature dependence of magnetic entropy change for MnAs thin films grown on (a) (0 0 1)-oriented GaAs substrate. (b) (1 1 1)-oriented GaAs substrate. (Adapted from [86])

In 2013, L. Chen [111] studied the MCE in ~20 nm $La_{0.67}Sr_{0.33}MnO_3$ thin films grown on (0 0 1)-oriented $LaAlO_3$, (0 0 1)-oriented $SrTiO_3$ and (0 0 1)-oriented LSAT substrates. Different transition temperatures were also observed in $La_{0.67}Sr_{0.33}MnO_3$ thin films under different strain states. In the same year, X. Moya and N. D. Mathur [112] reported MCE of ~34 nm $La_{0.7}Ca_{0.3}MnO_3$ grown on (0 0 1)-oriented $BaTiO_3$. Giant and reversible extrinsic MCE in $La_{0.7}Ca_{0.3}MnO_3$ was created using strain-mediated feedback from a first-order structure phase transition in $BaTiO_3$ substrate as shown in Figure 2.18.

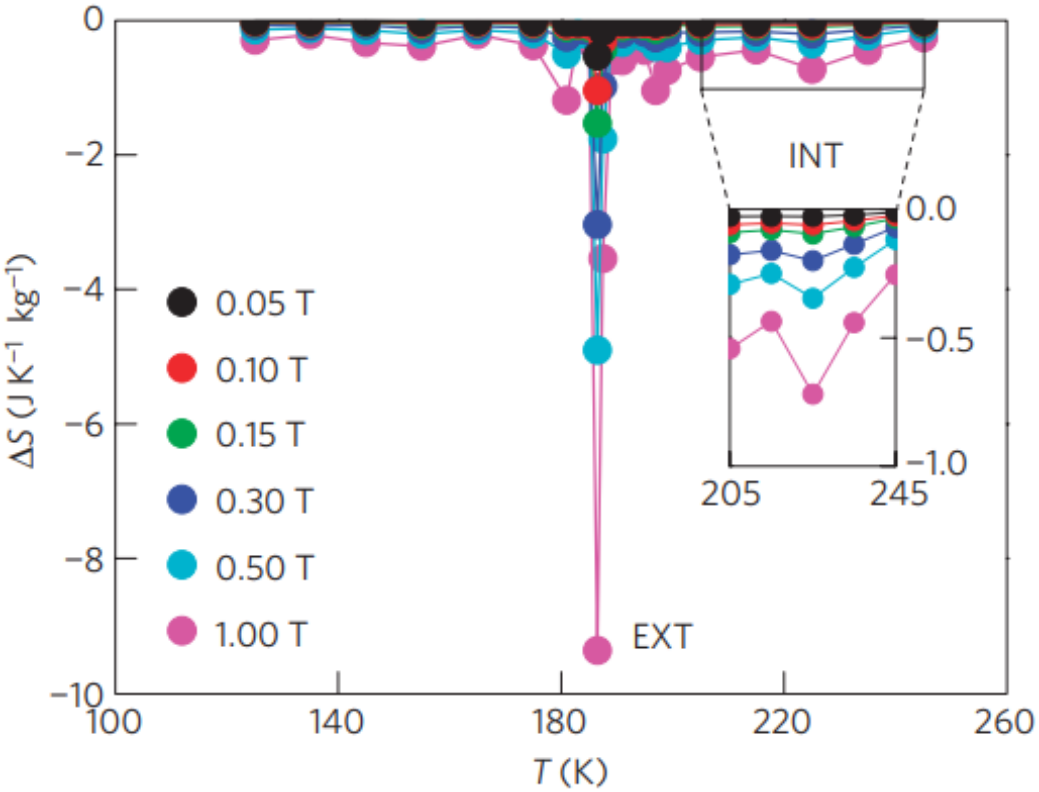

Figure 2.18 Temperature dependence of magnetic entropy change for $La_{0.7}Ca_{0.3}MnO_3$ grown on (0 0 1)-oriented $BaTiO_3$. Extrinsic (EXT) MCE in $La_{0.7}Ca_{0.3}MnO_3$ arises near first-order structure phase transition temperature of $BaTiO_3$ and intrinsic (INT) MCE in $La_{0.7}Ca_{0.3}MnO_3$ arises near Curie temperature of $La_{0.7}Ca_{0.3}MnO_3$. (Adapted from [112])

Another method to tailor MCE in thin films is interface engineering. In 2011, W. Prellier [113] reported the MCE in ($La_{0.7}Sr_{0.3}MnO_3$/$SrRuO_3$) superlattices. Comparing to $La_{0.7}Sr_{0.3}MnO_3$ bulk, a reduction of transition temperature of $La_{0.7}Sr_{0.3}MnO_3$ in the superlattices form was observed due to the finite size effect. Maximum value of magnetic entropy changes of $La_{0.7}Sr_{0.3}MnO_3$ in the superlattices form remained similar with a wider working temperature range. The microscopic mechanism was explained by the effect of the interfaces induced by superlattice structure and higher nanostructural disorder. In 2012, C. W. Miller [114] compared the MCE in $La_{0.56}Sr_{0.44}MnO_3$ alloy thin film and $[(SrMnO_3/LaMnO_3)_4/LaMnO_3]_9$ superlattices (both were 31 nm). The magnetic entropy changes and relative cooling power in alloy thin film were larger than those of superlattices. The La and Sr cations on the A-sites were more disordered in alloy thin film thus giving an

increased variation in the Mn-O-Mn bond angles and lattice distortions. Consequently, the spin coupling was weakened, and magnetic entropy changes enhanced.

In 2015, Y. H. Chu [115] reported MCE in the Mn_3O_4-$La_{0.7}Sr_{0.3}MnO_3$ nanocomposite thin film grown on $SrTiO_3$, as shown in Figure 2.19. Dy doping 10%, 13%, 17% and 20% of Mn_3O_4 second phase into the $La_{0.7}Sr_{0.3}MnO_3$ matrix, a homogeneous dispersed Mn_3O_4 nanocrystal, instead of nanopillars (frequently seen in VAN structure), was formed. An enhanced magnetic entropy change was observed in the Mn_3O_4-$La_{0.7}Sr_{0.3}MnO_3$ nanocomposite thin film compared to those $La_{0.7}Sr_{0.3}MnO_3$ in bulk or thin film forms. Interfacial magnetic coupling between Mn_3O_4 and $La_{0.7}Sr_{0.3}MnO_3$ was proposed to explain the MCE enhancement in the nanocomposite thin films.

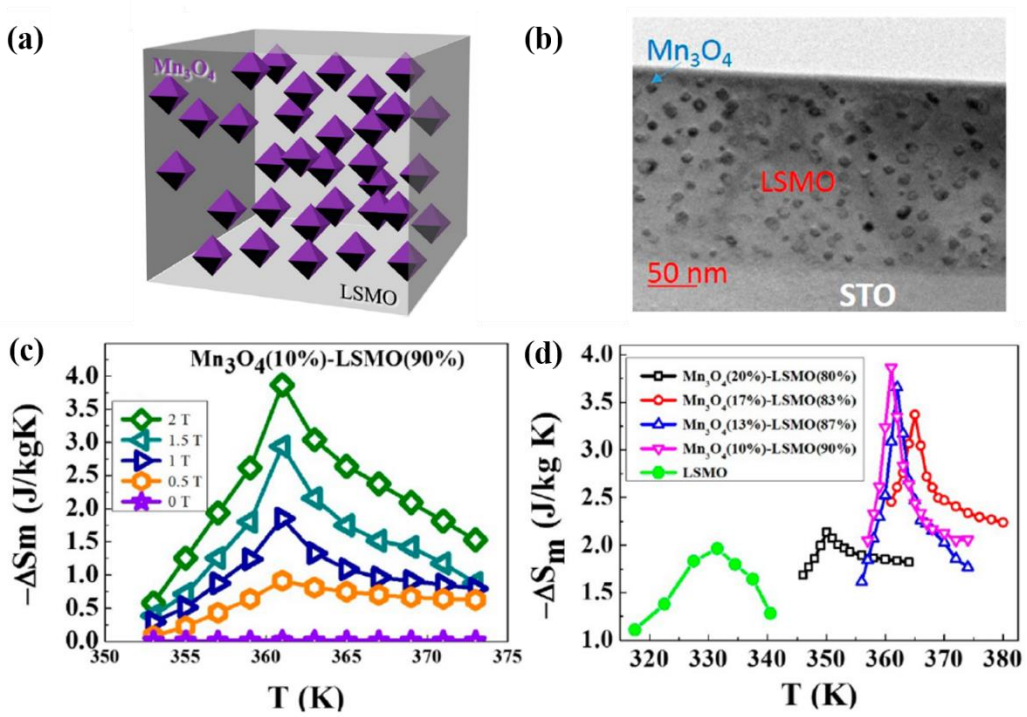

Figure 2.19 (a) Schematic of self-assembled Mn_3O_4-$La_{0.7}Sr_{0.3}MnO_3$ nanocomposite. (b) Cross-sectional TEM image of Mn_3O_4-$La_{0.7}Sr_{0.3}MnO_3$ nanocomposite thin film grown on $SrTiO_3$ substrate. (c) Temperature dependence of magnetic entropy change in (10%) Mn_3O_4-(90%) $La_{0.7}Sr_{0.3}MnO_3$ nanocomposite. (d) Temperature dependence of magnetic entropy change in (x%) Mn_3O_4- (100-x%) $La_{0.7}Sr_{0.3}MnO_3$ (x=0, 10, 13, 17, 20) nanocomposite under magnetic field change of 2T. (Adapted from [115])

2.5 Summary

From the literature reviews presented above, there are several interesting points waiting to be explored about ETO. To fully understand and control the mechanism of electrical field control of magnetism via the spin-lattice coupling, it is important to explore the magnetic interactions and underlying mechanisms of emergent FM in strained ETO films. Previous works trying to solve this challenge are focused on biaxially strained ETO films with a thickness less than 25 nm and different scenarios were used for explaining the FM phase obtained, but there has been no clear consensus of its origin. The latest proposal reckoned that the 3rd NN interactions play an unneglectable role in determining the magnetic ground state of ETO (as mentioned in Section 2.3). To systematically tune the strain along 3rd NN interaction is challenging using the method of conventional biaxial strain (induced by substrates, due to Poisson effect), under this circumstance, VAN approach is promising since the vertical out-of-plane strain is tuned independently of the in-plane strain. Furthermore, systematic strain tuning is enabled simply by changing the ratios of the second phases in the VAN system. ETO shows promising properties as a magnetic refrigeration material to work under low temperature range. Though there are several reports about the magnetic entropy change (or MCE) about ETO-based compounds in their bulk form (either single crystalline or polycrystalline), to the best of my knowledge, the magnetic entropy changes in ETO-based (nanocomposite) thin films is not reported so far. It would be interesting to explore the magnetic entropy change in ETO-based nanocomposite thin films. To realize the FM state in ETO, another approach is by chemical doping (mechanism based on Ruderman-Kittel-Kasuya-Yosida interaction between localized moments of nearest-neighbor Eu^{2+} spins mediated by conduction electrons). It would be interesting to explore the magnetic ground state of Gd-doped ETO thin films and the mechanism hidden behind. In all, this thesis focuses on creating novel three-dimensional strain in ETO-based VAN thin films to achieve phase transitions and to unveil the fundamental mechanisms determining the magnetic ground states of ETO. Enhanced magnetic entropy change is also achieved in ETO-based VAN thin films, as compared to its bulk form. Moreover, by doping Gd into ETO (introducing itinerant electron), FM is realized in otherwise AF ETO.

Chapter 3. Experimental Methods

This chapter presents the experimental techniques used to fabricate and characterize the self-assembled $(ETO)_{0.5}$-$(CeO_2)_{0.5}$, $(ETO)_{1-x}$-$(Eu_2O_3)_x$ and $Eu_{1-x}Gd_xTiO_3$ thin films. The first section focuses on thin films fabrication using pulsed laser deposition (PLD). The structural characterization and automated analysis of atomic resolution images techniques are described in the second section. The last two section of this chapter describes magnetic properties and valence states characterization using SQUID (Section 3.3) and XPS (Section 3.4).

3.1 Thin film fabrication

$(ETO)_{0.5}$-$(CeO_2)_{0.5}$, $(ETO)_{1-x}$-$(Eu_2O_3)_x$ and $Eu_{1-x}Gd_xTiO_3$ thin films were grown and studied in this work. Films were grown using PLD from ceramic targets. A brief description of target fabrication and the process of PLD is described in the next two parts.

3.1.1 Fabrication of targets

The ceramic targets used in this work were fabricated through conventional solid-state reaction. Pure powders of Eu_2O_3 (nanopowder, <150 nm particle size, 99.5% trace metal basis, Sigma-Aldrich), TiO_2 (powder, 99.9% metal basis, Alfa Aesar), CeO_2 (powder, 99.9% trace metal basis, Sigma-Aldrich), and Gd_2O_3 (powder, 99.9% trace metal basis, Sigma-Aldrich) were used to fabricate $(ETO)_{0.5}$-$(CeO_2)_{0.5}$, $(ETO)_{1-x}$-$(Eu_2O_3)_x$ and $Eu_{1-x}Gd_xTiO_3$ ceramic targets. These powders were weighed in the required proportions and ground for around 30 minutes until a homogenous mixture was formed. The mixtures were then pressed into pellets of diameter 3 cm under a hydraulic press with a pressure of 10 tons for 30 minutes. Those pressed pellets were then sintered in a furnace in air environment: heated from room temperature to 1400 ℃ with 5 ℃/min, kept it at 1400 ℃ for 24 hours, followed by slow-cooling with 1 ℃/min to room temperature. The dense pellets thus obtained for later use as the targets for PLD.

3.1.2 Pulsed Laser Deposition (PLD)

Transition metal ABO_3 perovskite oxides' broad properties are closely related to their structures. For instance, as shown in previously (Chapter 2, Section 2.2), the strain (induced from single crystalline substrate) has great influence on ETO's magnetic ground state, from other perspective, if the crystal structure of ETO is properly tuned (cubic to tetragonal), the FM (instead of AF) ground state will emergy in ETO. As mentioned in Chapter 2, Section 2.5, in order to systematically tune the strain along the {1 1 1} path, the VAN approach is ideal since the vertical out-of-plane strain can be tuned independently of the in-plane strain under the condition that ETOs are in high quality and are epitaxially grown on a single crystalline substrate.

Besides choosing a proper substrate and a suitable second phase, the thin film's growth technique used to grow the VAN structure thin film needs careful consideration. Many advanced techniques have been applied to sythesize single-crystalline oxide thin films of high qualities. For instances, Magnetron Sputtering (MS) [116], Metalorganic Vapour Phase Epitaxy (MOVPE) [117], (electron beam) Evaporation [118], Molecular Beam Epitaxy (MBE) [117], Pulsed Laser Deposition (PLD) [119], and others .

Among this techniques, PLD [120] is ideal for growing ETO-based VAN thin films (as well as Gd-doped ETO thin films), for the reason that it has the merit of offering good stoichiomety, good epitaxial quality (from single crystalling substrate). PLD is a physical vapor deposition process, carried out in vacuum, consists of a vacuum chamber equipped with pumps, a target holder and rotator (motor), substrate heater, and is typically equipped with various pressure gauges, controllers, and other instruments to control the deposition environment of the system, as shown in Figure 3.1.

During deposition process, a pulsed laser was focused onto the target of the materials (in this case, it is composite ceramic target) to be deposited. For sufficiently high laser energy density, ablated material was ejected from the target in a highly directed plume. The ablation plum provides material flux for film growth. Through choosing proper deposition parameters, epitaxial thin films will be able to grow by this system. Compared to other deposition techniques, PLD has the merits of preserving complex stoichiometries, easy to use multiple materials and easy to replace the targets, cost effective process (compared to MBE for growing the same kind of complex oxide materials) for exploring a wide range of complex oxide materials, and excellency in rapid

prototyping of materials and investigating various phases [120]. When it comes to the point of stoichiometry transfer character of the PLD, it is worth to emphasize here that for the deposition of multi-cation or VAN thin films, the phase of the target does not need to be precisely the same as that of the desired film and only the cation stoichiometry need be identical to that of the films [120]. This character is ideal for the VAN thin films growth, especially for the ETO-Eu_2O_3 composite, since it will not be necessary to obtain $EuTiO_3$ phase in the ceramic target (which is rather challenging to keep valence state of Eu to be 2+ after normal sintering process).

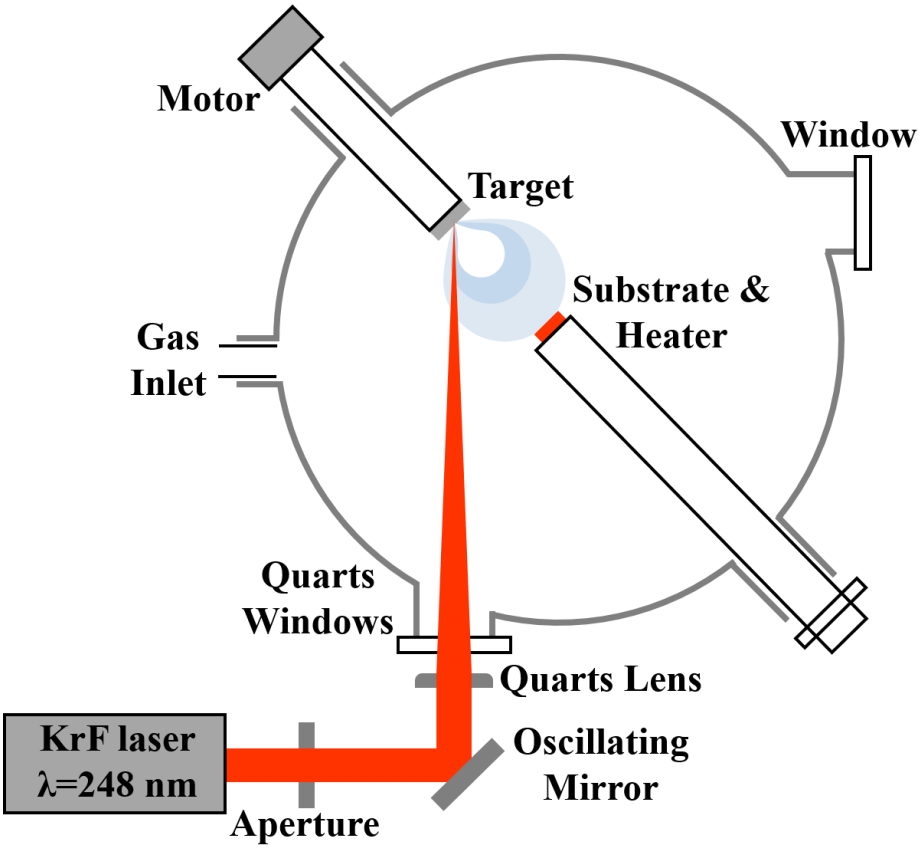

Figure 3.1 Schematic of PLD system.

Before deposition, the substrates were cleaned by bathing and ultrasonication in acetone, isopropanol and still water for 15 minutes, respectively, and finally dried with nitrogen gas. During deposition, the ETO-based thin film deposition was normally done in high vacuum environment to minimize oxygen content and prevent unwanted second phase from forming. A base pressure of $1\sim2*10^{-6}$ to $1*10^{-7}$ torr was usually introduced to grow the films. In a normal process, the

substrate was heated up to a growth temperature before deposition (when the substrate temperature was heated up to around 710 ℃, the chamber pressure was about $2*10^{-6}$ Torr). A high-power pulsed laser beam generated by a Lambda Physik® KrF excimer laser with a wavelength of 248 nm was used to strike the composite target. Parameters like laser beam energy and laser pulse rate were adjusted during growth. Also, the target was rotated during deposition process to ensure optimal usage of target material.

3.2 Structural characterization

In this section, structural characterization and automated analysis of atomic resolution images techniques are described.

3.2.1 X-Ray Diffraction (XRD)

XRD is a laboratory technique that reveal materials' information, such as chemical composition, crystal structure, crystallite size, strain, preferred orientation and layer thickness. The basic idea of XRD is as follows: The spacing between the crystal lattices is on the order of a few angstroms and it is comparable to the wavelength of X-ray, thus crystalline atoms will cause a beam of incident X-rays to diffract into many directions. According to Bragg's law [121]:

$$n\lambda = 2dsin\theta \tag{7}$$

where n is an integer number, λ is the wavelength of X-ray source, d is material's lattice spacing and θ is the angle between incident beam and the material's crystallographic plane. The law demonstrates that the path length difference between X-rays reaching the atomic planes must be a multiple of their wavelength to undergo constructive interference; otherwise they will interfere destructively, as shown in Figure 3.2.

By detecting the angles and intensities of these diffracted beams, a crystallographer can produce a three-dimensional picture describing the density of electrons. From this picture, structure information of this material can be determined.

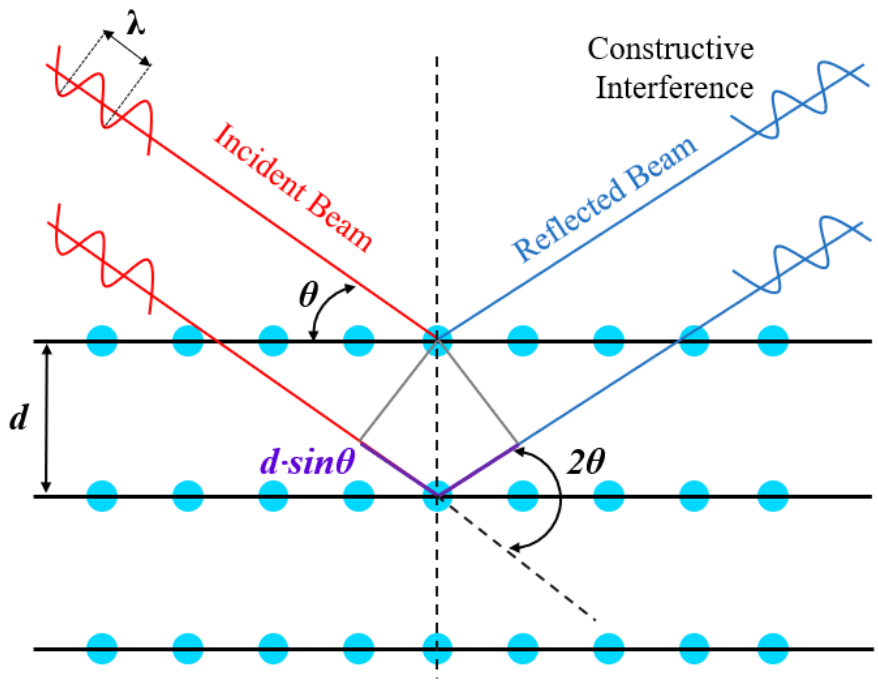

Figure 3.2 Schematic of the constructive interference according to Bragg's law.

In this work, a PANalytical Empyrean® High-resolution X-ray diffractometer using Cu-Ka_1 radiation (λ = 1.5406 Å), a hybrid two bounce monochromator, programmable anti-scatter slits and a scintillation counter . Four circles geometry-omega (ω), theta (θ), chi (χ) and phi (Ψ) was used to obtain diffraction signals of the thin films, as shown in Figure 3.3 (a).

In this work, 2θ-ω scans were performed to detect the thin films' phase composition and epitaxial orientation. As shown in Figure 3.3 (b), 2θ-ω scans were performed in Bragg-Brentano geometry, in which the diffracted angle (2θ) moved twice as the incident angle (ω). Thus, the d spacing of the crystalline planes (oriented parallel to the surface) of the investigated film can be obtained. And by using the Bragg's law (Equation 7), the out-of-plane lattice parameters of thin films can be determined.

Reciprocal space map (RSM) scans were performed to quantify the degree of strain in the thin film and the mismatch between thin films and substrate. A series of 2θ-ω scans *versus* ω were collected, as shown in Figure 3.3 (c). All these data formed a contour map in q_x and q_z coordinates at a given reflection. The q_x and q_z coordinates can reveal the reciprocal spacing of the in-plane

and out-of-plane lattice parameters (in ETO and STO, $q_x = h/a$, $q_z = l/c$). The lattice mismatch and strain of a phase with respect to the substrate were acquired by the position of diffracted peaks. The strain caused by lattice mismatch between thin films and substrates can be calculated from the following equations:

$$\text{In-plane strain} = \%\ \text{In-plane lattice mismatch} = \frac{\alpha_{\text{film}} - \alpha_{\text{substrate}}}{\alpha_{\text{substrate}}} \times 100\% \quad (8)$$

$$\text{Out-of-plane strain} = \%\ \text{Out-of-plane lattice mismatch} = \frac{c_{film} - c_{bulk}}{c_{bulk}} \times 100\% \quad (9)$$

In these equations, α_{film} was the in-plane lattice parameters of the thin film, c_{film} was the out-of-plane lattice parameters of the thin film, $\alpha_{substrate}$ was the in-plane lattice parameters of the substrate, and c_{bulk} was the out-of-plane lattice parameters of the material in bulk, respectively.

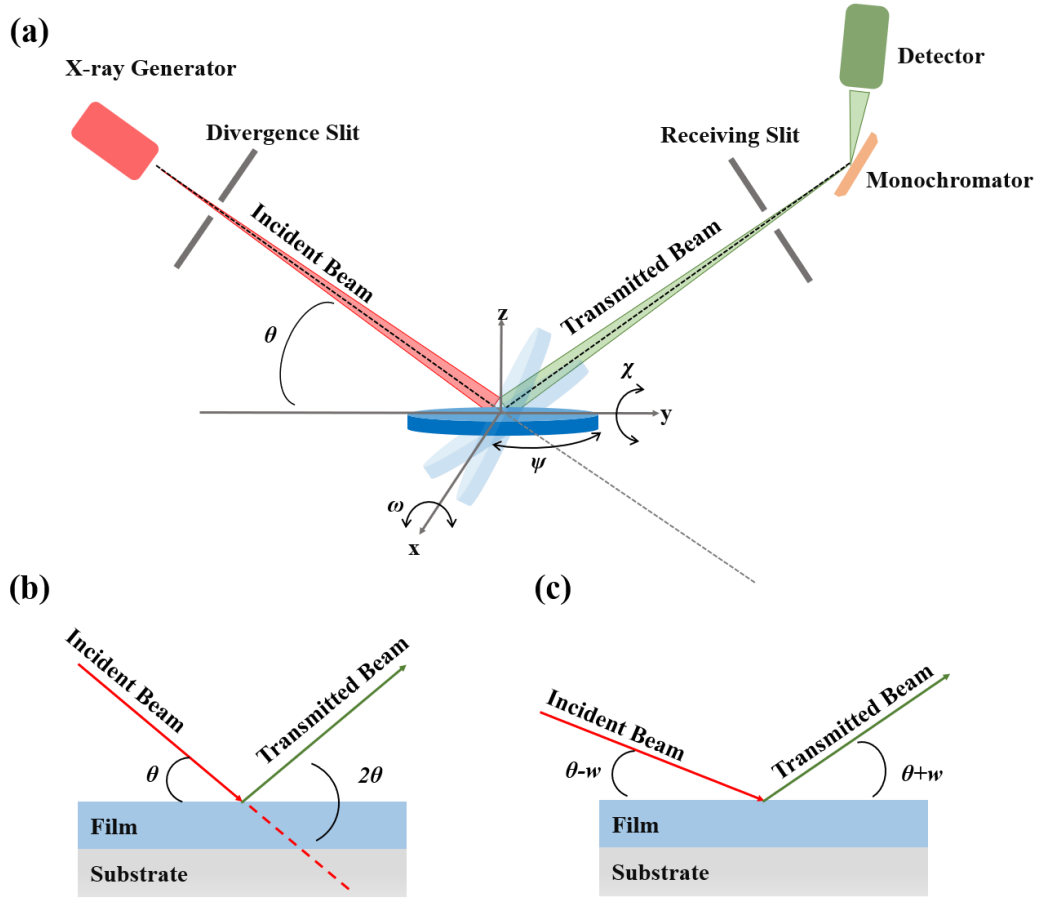

Figure 3.3 (a) Schematic of X-ray diffraction system; (b) 2θ-ω scan; (c) Reciprocal space mapping.

3.2.2 Transmission Electron Microscopy (TEM) and Scanning Transmission Electron Microscopy (STEM)

TEM and STEM can provide very detailed information in analyzing the crystallographic structure at atomic level and phase morphologies. The TEM and STEM characterizations in this work were carried out by Ping Lu (Sandia National Laboratory, U.A.), Xing Sun and Haiyan Wang (Purdue University, U.S.). TEM can provide conventional bright field and dark field high resolution images, while STEM can provide clear Z-contrast images, elemental mapping contrast thus can be performed. Besides the morphological images, the selected area electron diffraction (SAED) was carried out as well. In this thesis, (high-resolution) transmission electron microscopy and scanning transmission electron microscopy were conducted on $(EuTiO_3)_{0.8}$-$(Eu_2O_3)_{0.2}$ and $(EuTiO_3)_{0.5}$-$(Eu_2O_3)_{0.5}$ VAN thin films (grown on $SrTiO_3$ substrates). A FEI Titan^{TM} G2 800-200 STEM with a Cs probe corrector was used in this study. The film microstructures were studied by STEM imaging using high-angle annular dark-field (HAADF) detector, and elemental mapping by energy-dispersive x-ray spectroscopy.

3.2.3 Atomap- Analyzing atomic resolution scanning transmission electron microscopy

In this work, Atomap® software [122] tool was used to perform atomic column simulations on local STEM images. After removing the image background (noise filtered with 1-D PCA [123]), the Eu and Ti atomic columns of $EuTiO_3$ perovskite in STEM images were recognized in the following steps:

(1) Find the position of all Eu cations atomic columns since Eu cations are the heaviest element and have the strongest intensity;

(2) Refine the positions using center-of-mass until they are close enough for the 2-D Gaussian fitting to work effectively;

(3) Refine the positions again by locating with nearest neighbor;

(4) Fit the Eu cations atomic columns using the 2-D elliptical Gaussian function $I(x, y)$, which is defined as [122]:

$$I(x,y) = I_0 + A\exp\{-[a(x-x_0)^2 - 2b(x-x_0)(y-y_0) + c(y-y_0)^2]\} \quad (10)$$

$$a = \frac{cos^2\theta}{2\sigma_x^2} + \frac{sin^2\theta}{2\sigma_y^2}$$

$$b = -\frac{sin2\theta}{4\sigma_x^2} + \frac{sin2\theta}{4\sigma_y^2}$$

$$c = \frac{sin^2\theta}{2\sigma_x^2} + \frac{cos^2\theta}{2\sigma_y^2}$$

where I_0 is the background, A is the amplitude, x_0 and y_0 are the centre positions, σ_x and σ_y are the standard deviations, and θ is the rotation.

(5) Remove Eu cations from the images and repeat the above-mentioned steps again to find and fit the column positions of Ti cations (Ti cations are heavier than oxygen thus can be located after removing the Eu cations).

After knowing the positions of both Eu and Ti cations atomic columns, structure information (Eu-Ti-Eu bond angle) thus can be obtained.

3.3 Magnetic measurements using the Superconducting Quantum Interface Device (SQUID)

The SQUID is a sensitive magnetometer used to detect small magnetic fields (~10^{-14} T), which consists of two superconductors separated by thin insulating layers to form two parallel Josephson junctions, as shown in Figure 3.4.

In this work, the temperature dependence of magnetization (*M-T*) and magnetic field dependence of magnetization (*M-H*) were measured using Quantum Design's MPMS® 3 (SQUID magnetometry) and MPMS® XL system. These systems use a direct current (DC) scan method to measure magnetic flux in a superconducting loop as the sample moves in the magnetic field. The sample was initially located in the center of the superconducting detection coil, inductively coupled to the magnetic field. When it moved through the coil, the magnetic moment of the sample induced an electric current in the detection coil. By measuring the voltage oscillation, a change of magnetic flux can be quantized. This system can generate a magnetic field up to ±7 T and provide the temperature control from 400 K to 1.8 K.

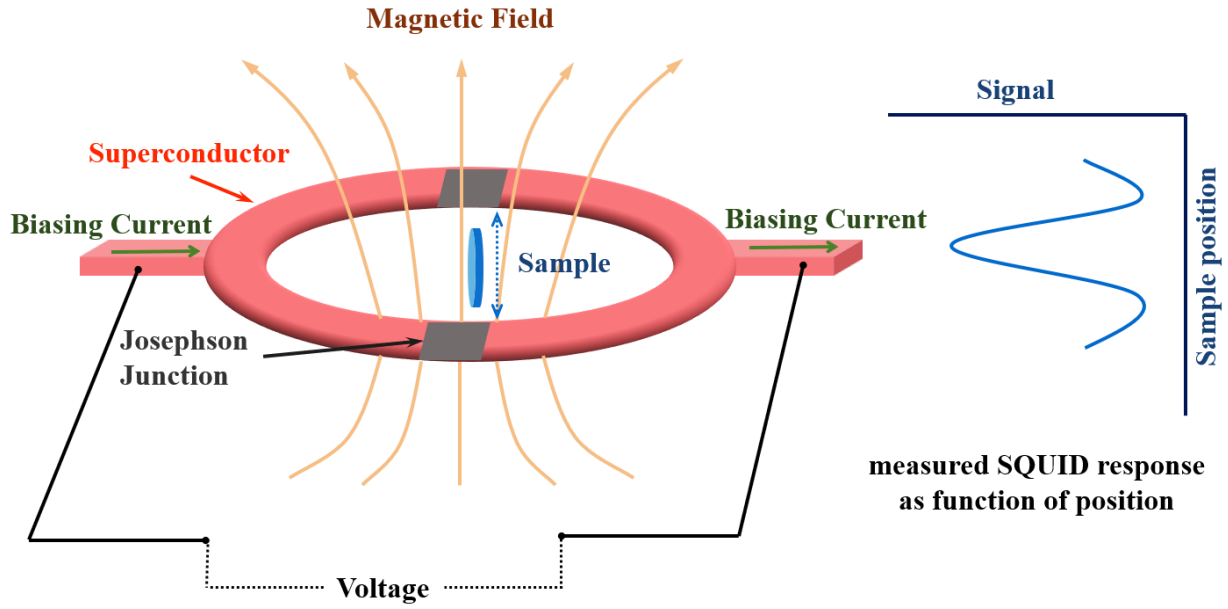

Figure 3.4 Schematic of SQUID setup.

3.4 Valence states measurements using X-ray Photoemission Spectroscopy (XPS)

Valence states of chemical cation at the surface of the films was investigated by XPS, a surface sensitive quantitative spectroscopic technique that can measure elemental composition, empirical formula, chemical state and electronic state of the elements within the surface of a material.

In XPS, a monochromatic beam of X-ray photons with energy *hv* is used to irradiate the measured sample. After receiving the X-ray photons, the core electrons with binding energy (*BE*) less than *hv* are ejected according to the photoelectric emission effect proposed by Einstein [124], as shown in Figure 3.5 (a):

$$BE = hv - (E_k + W_0) \tag{11}$$

where E_k is the kinetic energy of photoelectric emitted electron (referenced to E_{vac}); W_0 is the work function which is defined by the energy difference between Fermi level (E_F) and vacuum (E_{vac}); *BE* is the binding energy of core electrons being promoted to material's Fermi level. For different elements, atomic orbital and chemical environment of atoms, their *BE* are different. Thus, a typical

XPS spectrum, as shown in Figure 3.5 (b), including the intensity of detected photoelectric emitted electrons versus their *BE*, can be obtained. By investigating these peak intensity, position and shape, elemental type and their chemical environment (or valence state) can be identified and quantified.

In this work, a schematic of the XPS setup is shown in Figure 3.5 (c). The X-ray source adopted was a SPECS XR 50, which consists of high intensity twin anode made of Al and Ag coating on silver. Results shown in this work were collected by using an Al-K_a source (1486.6 eV). The ultra-high vacuum provided a pressure of 10^{-9} Torr. The obtained data was further analyzed using the CasaXPS software.

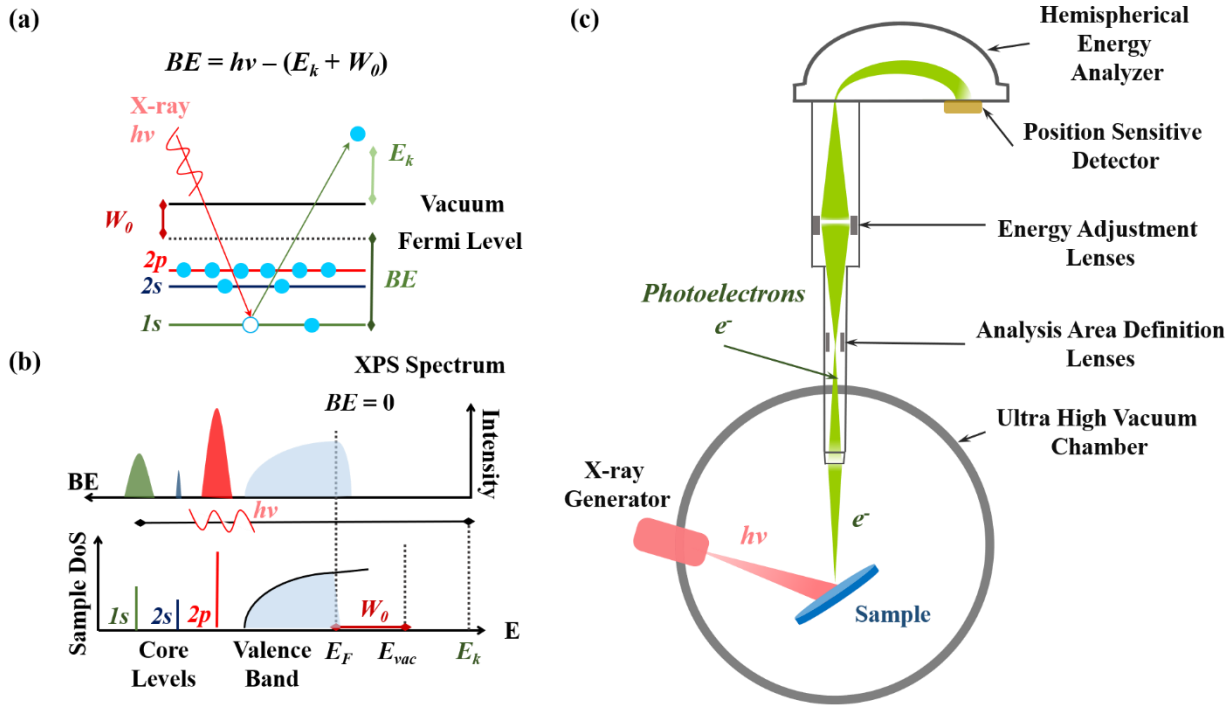

Figure 3.5 (a) The photoelectric emission effect. (b) XPS spectrum. (c) Schematic of the XPS system.

Chapter 4. Optimizing the growth of ETO-based VAN thin films – Results and discussion

This chapter presents the optimization of growth parameters searched in our PLD system, aiming to obtain high quality ETO-based VAN thin film. Attempts to find suitable binary oxide second phases to form the ETO-based VAN nanostructured thin film are carried out. After the suitable binary oxide Eu_2O_3 is confirmed, the possibility of changing the ratios of the Eu_2O_3 phase as well as changing the substrates of ETO-based VAN thin film is carried out in the last section.

4.1 Fabrication of $(ETO)_{0.5}$-$(CeO_2)_{0.5}$ VAN films

In this part, experiments were carried out aiming to find a proper second phase to incorporate with ETO to form self-assembled VAN films, thus introducing vertical strain to tune the strong correlated properties in ETO. The first attempt was CeO_2, a rare-earth fluorite oxide, which had been successfully served as second phase in $BaTiO_3$-CeO_2 VAN thin film grown on STO substrates [125].

4.1.1 Target fabrication and substrate temperature

The ceramic target used here was fabricated through conventional solid-state reaction. Pure powders of Eu_2O_3 (nanopowder, <150 nm particle size, 99.5% trace metal basis, Sigma-Aldrich), TiO_2 (powder, 99.9% metal basis, Alfa Aesar), CeO_2 (powder, 99.9% trace metal basis, Sigma-Aldrich) were used to fabricate $(ETO)_{0.5}$-$(CeO_2)_{0.5}$ ceramic target. The powders were weighed in the required proportions and ground for 30 minutes. The powder mixtures were then pressed into pellets (3 cm diameter) under hydraulic press with a pressure of 10 tons for 30 minutes. The pressed pellets were then sintered in a furnace in air environment: heated from room temperature to 1400 ℃ with 5℃/min, kept at 1400℃ for 24 hours, followed by slow cooling (1 ℃/min) to room temperature.

XRD 2θ-ω scans were carried out on the target to check the phases, as shown in Figure 4.1. Only $Eu_2Ti_2O_7$ and CeO_2 phases were identical [126,127]. As mentioned in Section 3.1.2, preserving

stoichiometries only requires the cation stoichiometry to be identical to that of targeted film, in other words, the phase of the target does not need to be precisely the same. We will prove this point in the latter section (for fabrication of $EuTiO_3$-Eu_2O_3 VAN films). The reason for the absence of $EuTiO_3$ phases is the easy oxidization of Eu^{2+} in $EuTiO_3$ when annealing in room atmosphere [117].

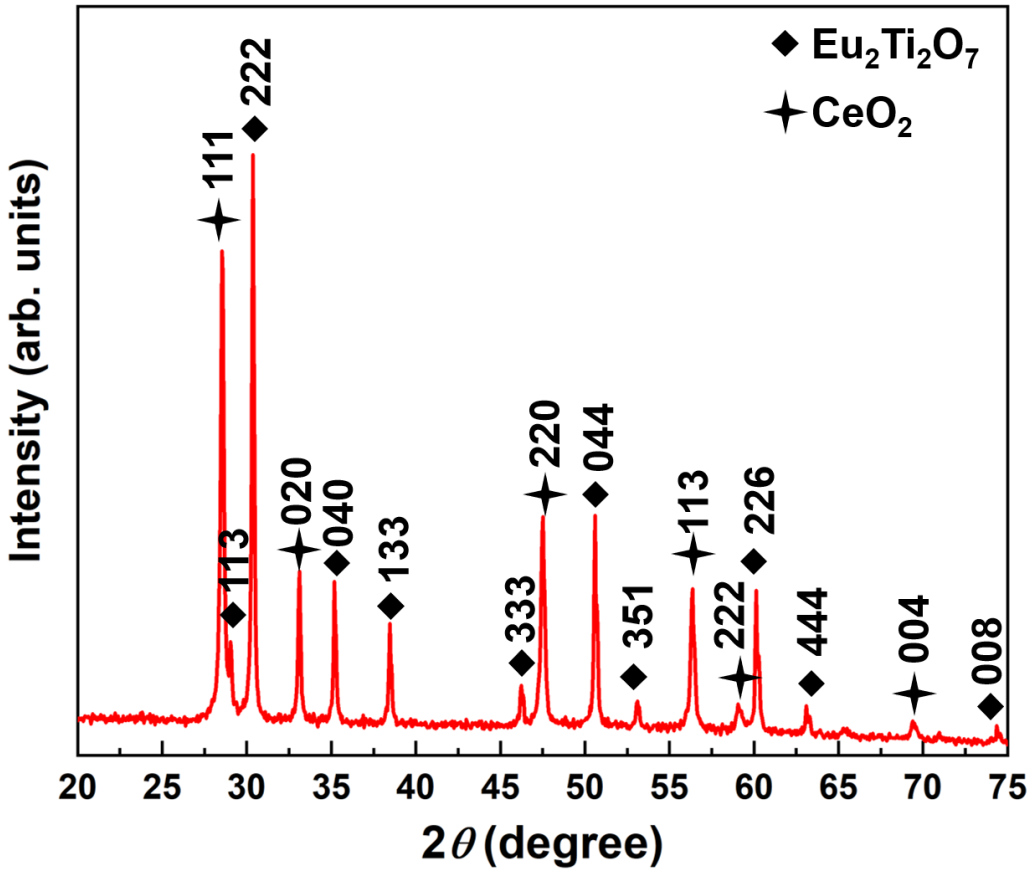

Figure 4.1 XRD 2θ-ω scan of ceramic target.

Thin films were grown under different substrate temperatures as shown in Table 4.1. A laser fluence of 2 J/cm^2 with a repetition rate of 3 Hz was used to ablate the ceramic target. During deposition, the samples were kept at $2 \cdot 10^{-6}$ Torr in vacuum. The samples were cooled down to room temperature with a cooling rate of 5 ^{o}C/min without extra post-annealing.

Table 4.1 $(ETO)_{0.5}$-$(CeO_2)_{0.5}$ thin film deposited varying substrate temperatures.

Sample Number	Substrate	Temperature (°C)	Growth Pressure (Torr)	In-situ post-annealing
1	(0 0 1)-oriented STO	710	$2 \cdot 10^{-6}$ in vacuum	No
2		720		
3		750		
4		780		

XRD 2θ-ω scans were carried out on these samples to identify the phases as shown in Figure 4.2. 0 0 l, 0 0 2 and 0 0 3 peaks of ETO and STO (substrate) could be observed. However, there were no clear CeO_2 peaks in these samples (CeO_2 did exist in target). At the position of 2θ around 28 °, small peaks which intensity nearly close to that of background could be observed. These peaks were suspected to be 1 1 1 peaks of CeO_2. So far, no clear evidence showing the co-existence of both ETO and CeO_2 phases under these growth condition.

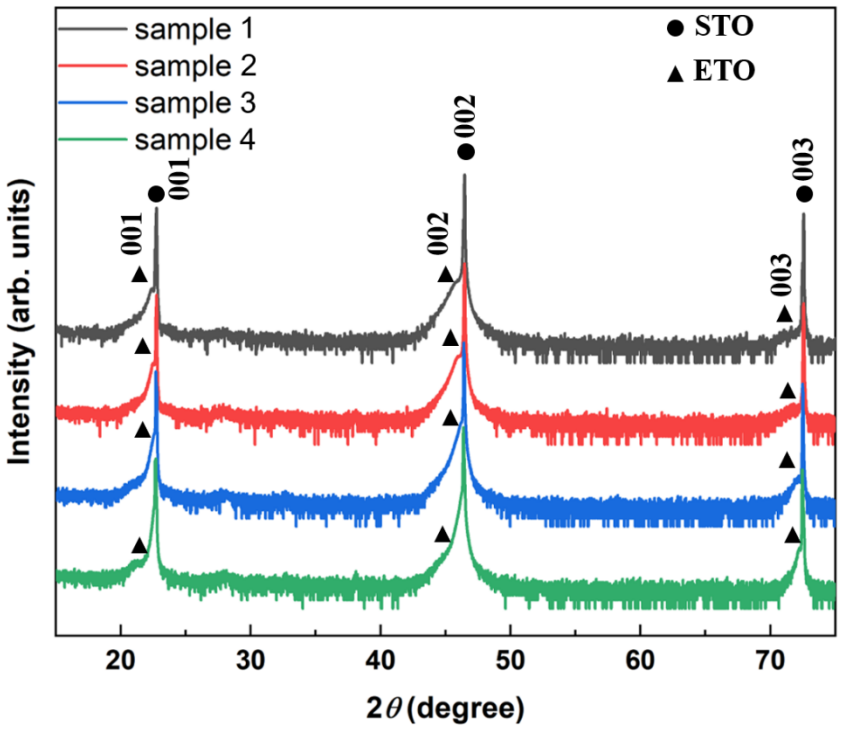

Figure 4.2 XRD 2θ-ω scans of $(ETO)_{0.5}$-$(CeO_2)_{0.5}$ thin film on (0 0 1)-oriented STO using differnet substrate temperatures during deposition.

4.1.2 Post-annealed under O_2 atmosphere

Among sample 1 to sample 4, the most promising one was sample 2, since its XRD 2θ-ω scan showed clear 0 0 *l* peaks of ETO and suspected 1 1 1 CeO_2 peak. In the literature reported $BaTiO_3$-CeO_2 VAN thin film grown on STO substrates [125], substrate temperature was set at 700 ^oC, which is very closed to our substrate temperature condition (sample 2). The major growth condition difference to ours was post-annealing the sample at a temperature of 500 ^oC for 30 mins at an oxygen partial pressure of 500 Torr. The purpose of post-annealing the $BaTiO_3$-CeO_2 VAN thin film was to compensate the oxygen loss during deposition in high vacuum. Inspired by this, sample 5 was made using the same growth parameter as sample 2 and post-annealed in O_2 at a temperature of 500 ^oC for 3 hours once deposition was finished.

XRD 2θ-ω scan was carried out on sample 5 and the 2θ-ω data of sample 2 and 5 is plotted together for better comparison, as shown in Figure 4.3. The intensity of suspected (1 1 1) CeO_2 peak maintained the same level while there were no detectable 0 0 *l* ETO peaks in sample 5. For the missing 0 0 *l* ETO peaks, one possibility was that oxygen vacancies been compensated and ETO showed bulk-like structure. However, this can be ruled out since in order to gain high quality ETO thin film (which lattice parameter same as STO), the only way is to anneal it in H_2+Ar atmosphere at a temperature of near 1000 ^oC from previous report [128]. From 2θ-ω scan of sample 5, there existed no $Eu_2Ti_2O_7$ impurity phases (refer to Figure 4.1), since the post-annealed temperature for sample 5 was 500 ^oC, which was not high enough for $Eu_2Ti_2O_7$ to crystalize [129,130].

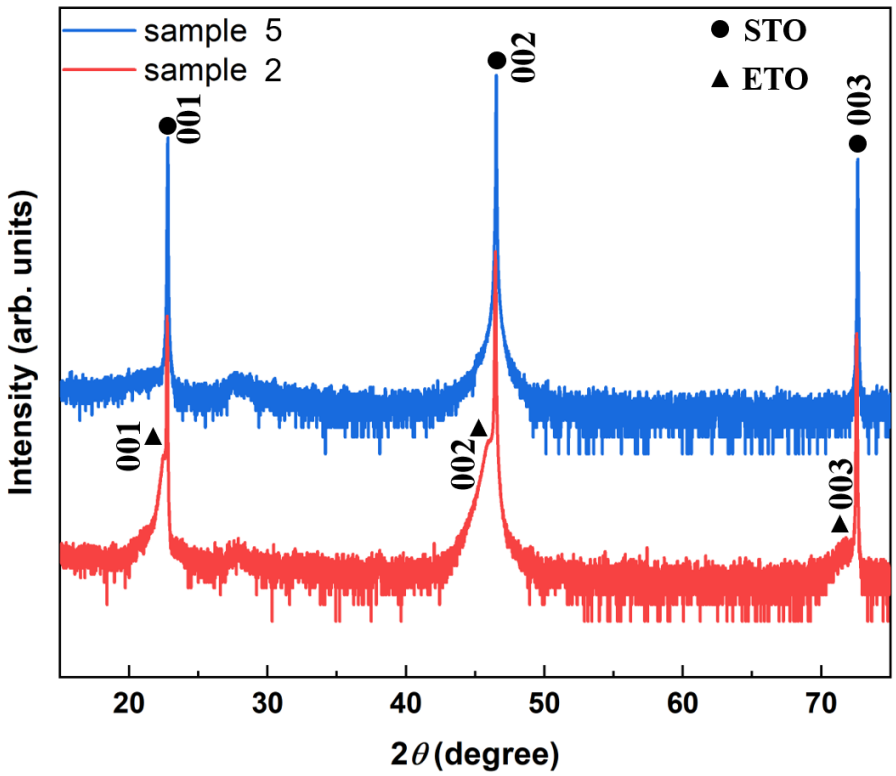

Figure 4.3 XRD 2θ-ω scans of $(ETO)_{0.5}$-$(CeO_2)_{0.5}$ thin film with O_2 post-annealing (sample 5) and without O_2 post-annealing (sample 2).

4.1.3 Buffer Layer

The above experimental trails on making the $(ETO)_{0.5}$-$(CeO_2)_{0.5}$ thin film suggested a possibility of poor crystallinity CeO_2. By inserting a very thin CeO_2 layer (served as seeding layer of CeO_2) before growing the $(ETO)_{0.5}$-$(CeO_2)_{0.5}$ thin film, the situation might be improved. Here we used two targets for this process, one was the $(ETO)_{0.5}$-$(CeO_2)_{0.5}$ composite ceramic target used for sample 1 to sample 4, the other was pure CeO_2 ceramic target. After the STO substrate was heated up to 700 ^oC, oxygen pressure was kept at $2.2 \cdot 10^{-1}$ mbar for growing the CeO_2 seeding layer. After growing CeO_2 thin layer, the chamber was pumped down again to base pressure ($2 \cdot 10^{-7}$ Torr in vacuum). When the system condition was stable, $(ETO)_{0.5}$-$(CeO_2)_{0.5}$ thin film was grown following the growth condition of sample 2. Thus the $(ETO)_{0.5}$-$(CeO_2)_{0.5}$/CeO_2/STO thin film was made (named sample 6). XRD 2θ-ω scan of sample 6 was carried out as shown in Figure 4.4. 1 1 0 and 0 0 2 CeO_2 peaks were identical, however there were no 0 0 *l* ETO peaks in sample 6.

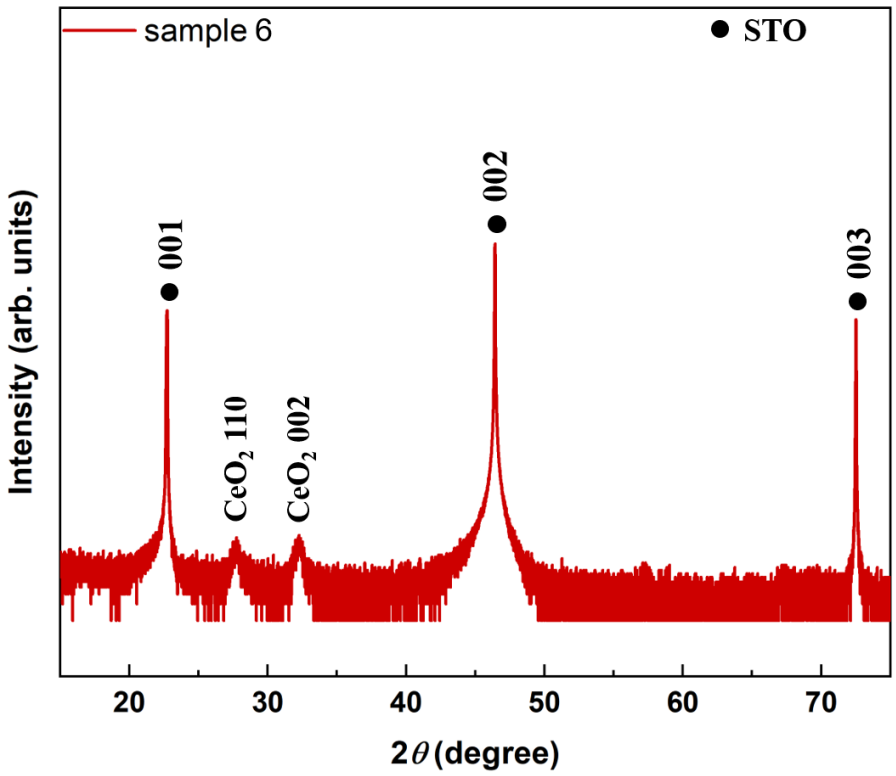

Figure 4.4 XRD 2θ-ω scans of $(ETO)_{0.5}$-$(CeO_2)_{0.5}$/CeO_2/STO.

4.2 Fabrication of $(ETO)_{0.5}$-$(Eu_2O_3)_{0.5}$ VAN films on STO substrate

To find a proper binary oxide second phase to form ETO-based self-assembled nanocomposite thin film using PLD was challenging since ETO needed to be grown in relatively high vacuum (or reducing atmosphere) to prevent the oxidization of Eu^{2+}. Based on the experimental results from last section, it would be ideal if the binary oxide second phase could be crystalline in relative high vacuum. Eu_2O_3 thin film grown on Si substrates under vacuum of around 10^{-6} Torr with a substrate temperature of 750 ^oC using PLD was reported [131].

Besides the growth condition compatibility, the non-magnetic Eu_2O_3 [132] second phase in ETO-based self-assembled nanocomposite thin film owns the following merits:

(1) it will not poison or modify the composition of ETO as it has the same elemental constituents.

(2) it is mechanically stiffer than ETO (Eu_2O_3 elastic modulus: 150 GPa [133], ETO elastic modulus: 76 GPa [134]).The difference in elastic modulus is required to achieve strain control on one phase by the other and thus enabling coupling and tuning new properties.

(3) it has cubic structure with a larger lattice parameter (a = 10.859 Å for bulk Eu_2O_3 [135]) and so, ideally if Eu_2O_3 nanopillars form in an ETO matrix with [001] direction, and that there is 8:3 correspondence of the lattices (8ETO:3Eu_2O_3), at the interfacial regions with ETO, it should stretch ETO out-of-plane by 4.28%.

4.2.1 Fabrication of ceramic targets prepared for $(ETO)_{1-x}$-$(Eu_2O_3)_x$ (x = 0.2, 0.25, 0.33, 0.5) VAN thin films growth.

The ceramic targets used in this section was fabricated through conventional solid-state reaction. Pure powders of Eu_2O_3 (nanopowder, <150 nm particle size, 99.5% trace metal basis, Sigma-Aldrich) and TiO_2 (powder, 99.9% metal basis, Alfa Aesar) were used to fabricate $(ETO)_{1-x}$-$(Eu_2O_3)_x$ (x = 0.2, 0.25, 0.33, 0.5) ceramic targets. The powders were weighed in the required proportions and ground for 30 minutes. The powder mixtures were then pressed into pellets (3 cm diameter) under hydraulic press with a pressure of 10 tons for 30 minutes. The pressed pellets were then sintered in a furnace in air environment: heated from room temperature to 1400 ℃ with 5℃/min, kept at 1400℃ for 24 hours, followed by slow cooling (1 ℃/min) to room temperature.

XRD 2θ-ω scans were carried out on the target to check the phases, as shown in Figure 4.5. Though in this section, we start with optimizing the growth parameters for growing $(ETO)_{0.5}$-$(Eu_2O_3)_{0.5}$ VAN thin films first, here we demonstrate XRD 2θ-ω scans of all ceramic targets prepared for making $(ETO)_{1-x}$-$(Eu_2O_3)_x$ (x = 0.2, 0.25, 0.33, 0.5) VAN thin films. As shown in Figure 4.5, Eu_2O_3 phases [136] were identical in all compounds. $Eu_2Ti_2O_7$ phases [127] were identical in x = 0.2, 0.25 and 0.33 compounds, while signals of $Eu_2Ti_2O_7$ phases were rather weak in x = 0.5 target since the molar ratio (volume ratio as well) of $Eu_2Ti_2O_7$ was rather small compared to the other three. $Eu_2Ti_2O_7$ phases, instead of $EuTiO_3$ phases, appeared in the ceramic target since the powder mixtures were sintered in air atmosphere. For getting pure $EuTiO_3$ phases in ceramic targets, it required sintering in H_2+Ar atmosphere [117]. For making thin films containing $EuTiO_3$

phases using PLD technique, $Eu_2Ti_2O_7$ ceramic target was used and pure ETO thin films were obtained after optimizing the growth conditions in PLD [128].

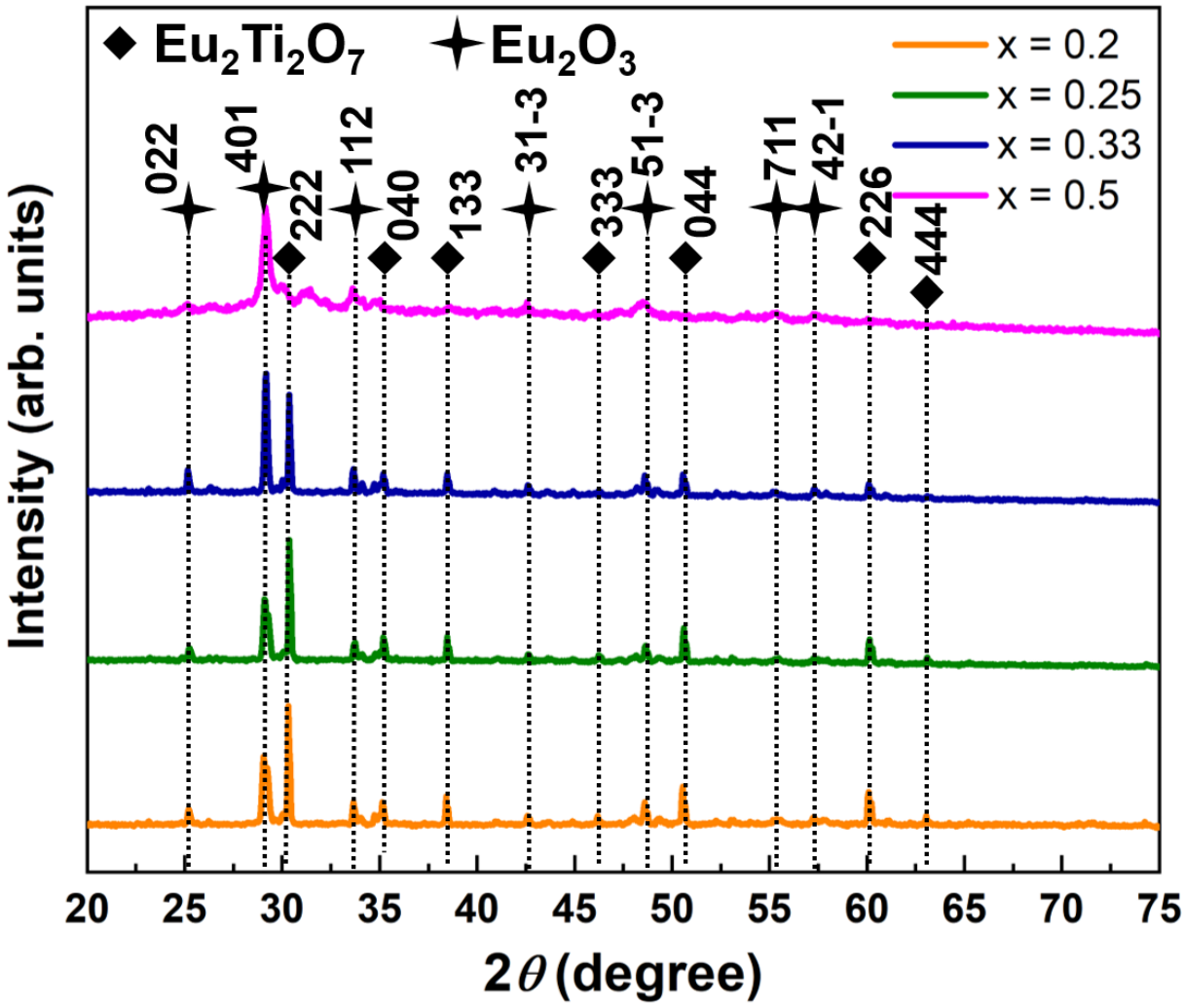

Figure 4.5 XRD 2θ-ω scans of ceramic targets prepared for (ETO)1-x-(Eu2O3)x (x = 0.2, 0.25, 0.33, 0.5) VAN thin films growth.

4.2.2 Fabrication of $(ETO)_{0.5}$-$(Eu_2O_3)_{0.5}$ VAN films in high vacuum

In this part, $(ETO)_{0.5}$-$(Eu_2O_3)_{0.5}$ thin films were grown on (0 0 1)-oriented STO substrate under high vacuum. A laser fluence of 2 J/cm^2 was used to ablate the ceramic target Parameters such as laser repetition rate, substrate temperature, and post-annealing process were performed to optimize thin films' deposition, as shown in Table 4.3.

Table 4.2 $(ETO)_{0.5}$-$(Eu_2O_3)_{0.5}$ thin films on (0 0 1)-oriented STO substrate in high vacuum.

Sample Number	Laser Repetition Rate (Hz)	Temperature (°C)	Growth Pressure (10^{-6} Torr)	Post-annealing		2θ-ω scans	
				In-situ in PLD Chamber	Furnace	ETO peaks	Eu_2O_3 peaks
7	1	700	1		96% Ar+4% H_2	Weak	No
8	1	700	0.5	Vacuum		Yes	Yes
9	1	750	1	Vacuum		No	No
10	1	650	2	Vacuum		No	No
11	1	700	1		96% Ar+4% H_2	No	Yes
12	5	700	1	Neither		Weak	Yes
13	1	700	1		O_2	No	Yes
14	1	700	1	Neither		Weak	No
15	1	700	1	Vacuum		No	No
16	10	700	2	Neither		Yes	No
17	5	700	1	Neither		Yes	Yes

After the samples were grown, XRD 2θ-ω scans were performed to identify whether there was coexistence of both $EuTiO_3$ (ETO) and Eu_2O_3 peaks (Ag peaks are from silver paste). Among these samples, there were three samples (sample 8, 12 and 17) showing both ETO and Eu_2O_3 peaks in 2θ-ω scans, as shown in Figure 4.6. All these three samples (sample 8, 12 and 17) were deposited on substrates at 700 °C. For better vacuum ($5 \cdot 10^{-7}$ Torr) during deposition with lower laser frequency (1 Hz) and post-annealed inside vacuum without O_2 or H_2+Ar atmosphere after the deposition, take sample 8 for example, clear ETO 0 0 l (l = 1, 2, 3), Eu_2O_3 2 2 2 and Eu_2O_3 0 0 4 peaks can be obtained in XRD 2θ-ω scans. When it came to sample 12 and 17, PLD deposition were performed when the vacuum was near 1×10^{-6} Torr and 5Hz laser frequency without post-annealing process, the intensity of $EuTiO_3$ 0 0 l (l = 1, 2) peaks were lower compared to that of sample 8, what is more, ETO 0 0 3 peaks could not be clearly presented in XRD 2θ-ω scans.

However, when compared sample 12 with sample 17, same thin film growth process was performed but showing observable differences in XRD 2θ-ω scans. The atmosphere (O_2 or H_2+Ar) annealing introduced after deposition to improve thin films (valence states of Eu can be switched accordingly) quality showed no significant result. Further optimized experiment needed to be performed to fully mastering the exact growth condition for controllable growth of $(ETO)_{0.5}$-$(Eu_2O_3)_{0.5}$ thin films.

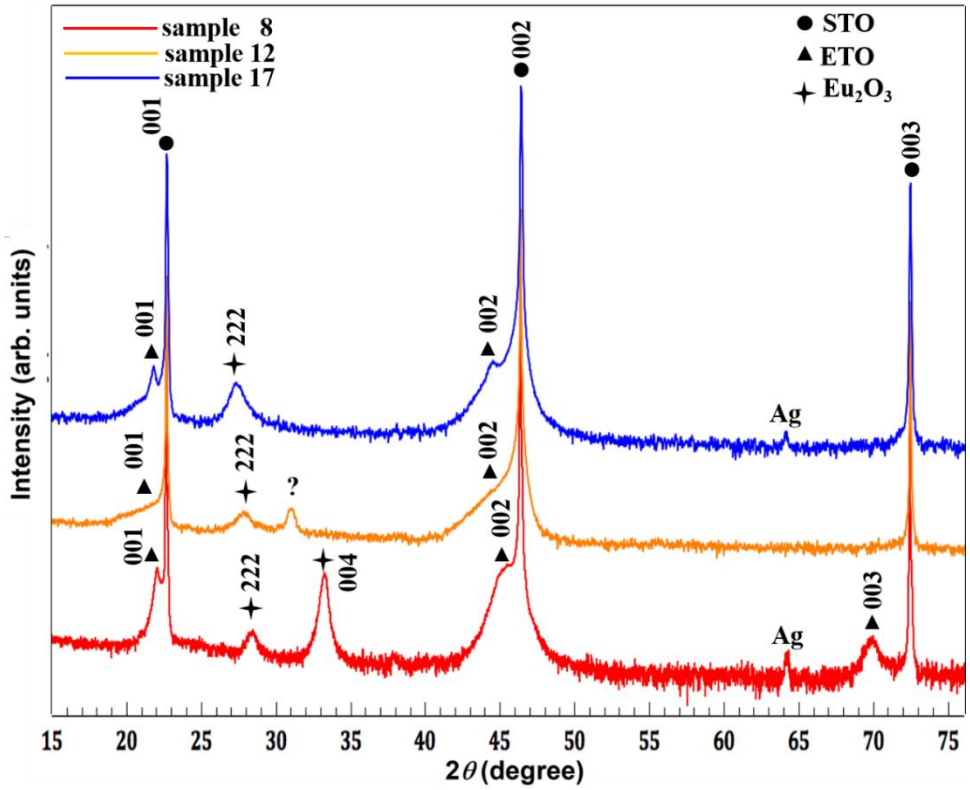

Figure 4.6 XRD 2θ-ω scans of $(ETO)_{0.5}$-$(Eu_2O_3)_{0.5}$ thin films grown on (0 0 1)-oriented STO substrate under high vacuum.

4.2.3 Fabrication of $(ETO)_{0.5}$-$(Eu_2O_3)_{0.5}$ VAN films in reducing atmosphere

Another attempt to make $(ETO)_{0.5}$-$(Eu_2O_3)_{0.5}$ thin films on (0 0 1)-oriented STO was performed when deposition undertaken at a reducing atmosphere of 96 vol % Ar + 4 vol % H_2. A laser fluence of 2 J/cm^2 with repetition rate of 3 Hz was used to ablate the ceramic target, substrate temperature was set to be 700 ^oC, 96 vol % Ar + 4 vol % H_2 gas was introduced after the substrate reached targeted temperature and maintained at 10^{-1} mbar ($7.5 \cdot 10^{-2}$ Torr), 10^{-2} mbar ($7.5 \cdot 10^{-3}$ Torr) and 10^{-}

^{3} mbar ($7.5 \cdot 10^{-4}$ Torr), as shown in Table 4.3. Once the deposition was finished, samples were cooled down without post-annealing to room temperature while keeping the pressure of reducing gas stayed the same.

Table 4.3 $(ETO)_{0.5}$-$(Eu_2O_3)_{0.5}$ thin films on (0 0 1)-oriented STO substrate under varying 96 vol % Ar + 4 vol % H_2 pressure.

Sample Number	**Laser Repetition Rate (Hz)**	**Temperature (°C)**	**96% Ar + 4% H_2 pressure during deposition (mbar)**	**2θ-ω scans**	
				ETO peaks shown	Eu_2O_3 peaks shown
18	3	700	$1 \cdot 10^{-1}$	No	Yes
19			$1 \cdot 10^{-2}$	Yes	Yes
20			$1 \cdot 10^{-3}$	Yes	No

After the samples were grown, XRD 2θ-ω scans were performed to identify whether there was coexistence of both ETO and Eu_2O_3 peaks, as shown in Figure 4.7. In sample 19, which was deposited under 10^{-2} mbar ($7.5 \cdot 10^{-3}$ Torr) 96 vol % Ar + 4 vol % H_2, ETO 0 0 *l* (*l* = 1, 2) and Eu_2O_3 2 2 2 peaks could be clearly identified. For sample grown under 10^{-1} mbar ($7.5 \cdot 10^{-2}$ Torr), $EuTiO_3$ 0 0 *l* peaks disappeared in XRD 2θ-ω scans and for sample grown under 10^{-3} mbar ($7.5 \cdot 10^{-4}$ Torr), Eu_2O_3 2 2 2 peaks disappeared.

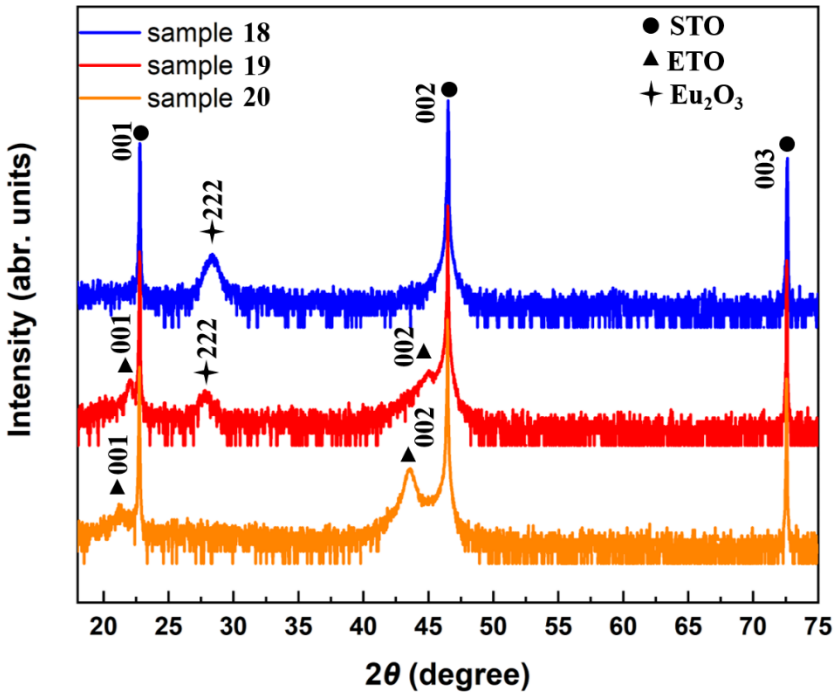

Figure 4.7 XRD 2θ-ω scans of $(ETO)_{0.5}$-$(Eu_2O_3)_{0.5}$ thin films grown on (0 0 1)-oriented STO substrate under varying 96 vol % Ar + 4 vol % H_2 pressure.

Based on the optimized reducing atmosphere (96 vol % Ar + 4 vol % H_2) confirmed to be 10^{-2} mbar ($7.5 \cdot 10^{-3}$ Torr) (sample 19), under which both ETO 0 0 l (l = 1, 2) and Eu_2O_3 2 2 2 peaks were shown in XRD 2θ-ω scans. Another $(ETO)_{0.5}$-$(Eu_2O_3)_{0.5}$ thin films on (0 0 1)-oriented STO were made using the same growth condition as sample 19 with slightly varying the substrate temperature during deposition, as shown in Table 4.4.

Table 4.4 $(ETO)_{0.5}$-$(Eu_2O_3)_{0.5}$ thin films on (0 0 1)-oriented STO substrate under 10^{-2} mbar 96 vol % Ar + 4 vol % H_2 pressure with varying substrate temperature.

Sample Number	**Laser Repetition Rate (Hz)**	**Temperature (°C)**	**96% Ar + 4% H_2 pressure during deposition (mbar)**	**2θ-ω scans**	
				ETO peaks shown	Eu_2O_3 peaks shown
21	3	650	$1 \cdot 10^{-2}$	No	No
22		710		Yes	Yes

23	720	Yes	Yes
24	730	Yes	Yes
25	740	Yes	Yes
26	750	Yes	No

XRD 2θ-ω scans were carried out on these sample as shown in Figure 4.8. A substrate temperature window ranging from 700 ^{o}C to 740 ^{o}C (under the 96 vol % Ar + 4 vol % H_2 pressure of $1 \cdot 10^{-2}$ mbar during deposition) could be confirmed in order to obtain both ETO and Eu_2O_3 phase observable from the 2θ-ω scans (as shown in Figure 4.7 and Figure 4.9). Comparing the 2θ-ω scans of samples deposited under substrate temperatures of 700 ^{o}C to 730 ^{o}C (sample 19, 22, 23, 24), slightly varying the substrate temperatures (10-20 ^{o}C) would affect the OOP orientation of Eu_2O_3 phase. Under the substrate temperature of 700 ℃, only ETO 0 0 l (l = 1, 2) and Eu_2O_3 2 2 2 peaks was shown. Under the substrate temperature of 710 ^{o}C and 720 ^{o}C, only ETO 0 0 l (l = 1, 2) and Eu_2O_3 0 0 4 peaks was shown. When the substrate temperature reached 730 ^{o}C, ETO 0 0 l (l = 1, 2, 3), Eu_2O_3 2 2 2 and Eu_2O_3 0 0 4 peaks coexisted. The crystallinity of both ETO and Eu_2O_3 peaks started to decay at the substrate temperature of 740 ^{o}C and disappeared at the substrate temperature of 750 ℃.

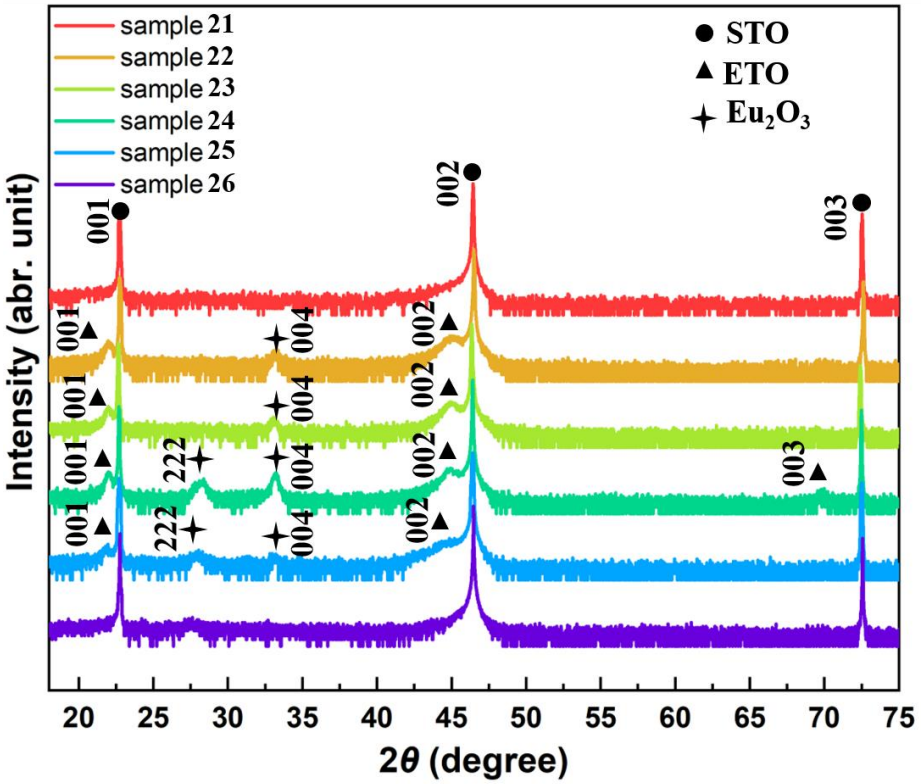

Figure 4.8 XRD 2θ-ω scans of $(ETO)_{0.5}$-$(Eu_2O_3)_{0.5}$ thin films grown on (0 0 1)-oriented STO substrate under 10^{-2} mbar 96 vol % Ar + 4 vol % H_2 pressure with varying substrate temperature.

4.3 Fabrication of $(ETO)_{1-x}$-$(Eu_2O_3)_x$ (x=0.2, 0.25, 0.33, 0.5) thin films

Based on the experience of making $(ETO)_{0.5}$-$(Eu_2O_3)_{0.5}$ thin films under various growth conditions, it would be crucial to control the growth parameters of growth pressure, substrate temperature and laser repetition rate at the same time to obtained both ETO and Eu_2O_3 phases with designed orientation. Also, in order to explore careful and systematic control of strong correlated couplings in ETO, different strain states induced by the second phase were desirable. Systematic strain tuning is was enabled simply by changing the ratios of the phases in VAN system. For instance, through varying the percentage of Sm_2O_3 in $Ba_{0.6}Sr_{0.4}TiO_3$ VAN films [56], the strain state was systematically tuned and consequently so were the ferroelectric properties. Also, by incorporating different RE_2O_3 (RE = Sm, Eu, Gd, Dy and Er) with increasing lattice parameters in $SrZrO_3$ VAN films [137], the vertical tensile strain was systematically increased in $SrZrO_3$, resulting in the enhancement of ion conductivity. In this work, the method of changing the ratios of Eu_2O_3 was utilized.

4.3.1 Fabrication of $(ETO)_{1-x}$-$(Eu_2O_3)_x$ (x=0.2, 0.25, 0.33, 0.5) thin films on STO (0 0 1)

As shown in Table 4.5, the $(ETO)_{1-x}$-$(Eu_2O_3)_x$ thin films were fabricated with a laser fluence of 2 J/cm and a repetition rate of 3Hz. During the deposition, the temperature of substrate was kept at 710 ^{0}C and the background vacuum was 1-2·10^{-6} Torr without introducing O_2 to prevent unwanted phases appear. The ceramic composite target used were introduced in Section 4.2.1. After the deposition finished, samples were cooled down to room temperature without further post-annealing.

Table 4.5 $(ETO)_{1-x}$-$(Eu_2O_3)_x$ (x=0.2, 0.25, 0.33, 0.5) thin films grown on (0 0 1)-oriented STO substrates.

$(ETO)_{1-x}$-$(Eu_2O_3)_x$	**Laser Repetition Rate (Hz)**	**Temperature (^{o}C)**	**Growth Pressure (Torr)**	**2θ-ω scans**		
				0 0 l ETO peaks	2 2 2 Eu_2O_3 peaks	0 0 4 Eu_2O_3 peaks
x=0.2	3	710	1-2·10^{-6}	Yes	None	Yes
x=0.25						
x=0.33						
x=0.5						

XRD 2θ-ω scans were carried out on these sample as shown in Figure 4.9. The coexistence of ETO 0 0 l (l = 1, 2, 3) and Eu_2O_3 0 0 4 peaks indicated the epitaxial growth of ETO and Eu_2O_3 phases in the VAN thin films under the optimized growth condition (Table 4.5). No Eu_2O_3 2 2 2 peak was observed from the 2θ-ω scans for all these films. When compared Figure 4.9 with Figure 4.5 (XRD 2θ-ω scans for ceramic targets), no $Eu_2Ti_2O_7$ phases were identical after deposition. It is same with experimental process carried out in depositing pure ETO thin films using $Eu_2Ti_2O_7$ ceramic targets as reported in literature [128]. And once more confirms the point (mentioned in Section 3.1.2) that when using PLD deposition technique, preserving stoichiometries only requires the cation stoichiometry to be identical to that of targeted film. Further strain states analysis of ETO under different ratio of Eu_2O_3 would be carried out in next chapter.

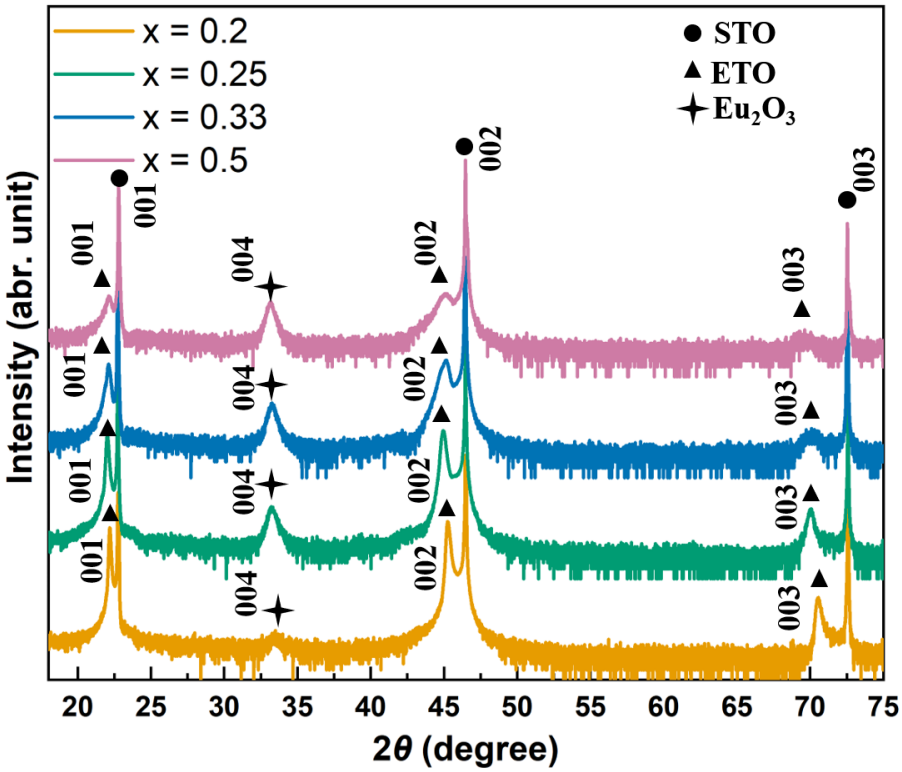

Figure 4.9 XRD 2θ-ω scans of $(ETO)_{1-x}$-$(Eu_2O_3)_x$ (x=0.2, 0.25, 0.33, 0.5) thin films grown on (0 0 1)-oriented STO substrates.

4.3.2 Fabrication of $(ETO)_{1-x}$-$(Eu_2O_3)_x$ (x=0.2) thin films on LSAT and $DyScO_3$ substrates

To explore the possibility of growing ETO-Eu_2O_3 nanocomposite film on substrates other than (0 0 1)-oriented STO, we chose $(ETO)_{0.8}$-$(Eu_2O_3)_{0.2}$ composite and tried to deposit on (0 0 1)-oriented LSAT and (1 1 0)-oriented $DyScO_3$ substrates. Since pure ETO thin films had been reported to deposit on these two substrates by molecular-beam epitaxy system [16,80], it was worth trying to grow our ETO-Eu_2O_3 nanocomposite on these two substrates.

Two $(ETO)_{0.8}$-$(Eu_2O_3)_{0.2}$ thin films were deposit on (0 0 1)-oriented LSAT and (1 1 0)-oriented $DyScO_3$ substrates respectively using the optimized growth parameters of $(ETO)_{1-x}$-$(Eu_2O_3)_x$ (x=0.2, 0.25, 0.33, 0.5) on STO, as shown in Table 4.6.

Table 4.6 $(ETO)_{0.8}$-$(Eu_2O_3)_{0.2}$ thin films grown on LSAT and $DyScO_3$.

$(ETO)_{1-x}$-$(Eu_2O_3)_x$	Substrate	Substrate Lattice Parameter	Laser Repetition Rate (Hz)	Temper-ature (°C)	Growth Pressure (Torr)	2θ-ω scans	
						0 0 l ETO peak	0 0 4 Eu_2O_3 peak
x=0.2	(0 0 1)-LSAT	*a*=3.868 Å (cubic)	3	710	$1\text{-}2\cdot10^{-6}$	Yes	Yes
	(1 1 0)-$DyScO_3$	*a*=3.94 Å (pseudocubic)				Yes	No

After the samples were grown, XRD 2θ-ω scans were carried out on as shown in Figure 4.10. Under the growth condition of Table 4.6, $(ETO)_{0.8}$-$(Eu_2O_3)_{0.2}$ thin films could be successfully deposited on (0 0 1)-oriented LSAT, showing clear peaks of ETO 0 0 *l* (*l* = 1, 2, 3) and Eu_2O_3 0 0 4. However, Eu_2O_3 0 0 4 peak could not be seen when the substrate was changed to (1 1 0)-oriented $DyScO_3$ while other growth parameter maintained the same. Comparing the results of $(ETO)_{0.8}$-$(Eu_2O_3)_{0.2}$ thin films grown on different substrates (STO, LSAT and $DyScO_3$), it was obvious that making the $(ETO)_{1-x}$-$(Eu_2O_3)_x$ nanostructured thin film required careful selection of substrates and growth window to form the nanostructured with preferred orientation and coexistence of both phases.

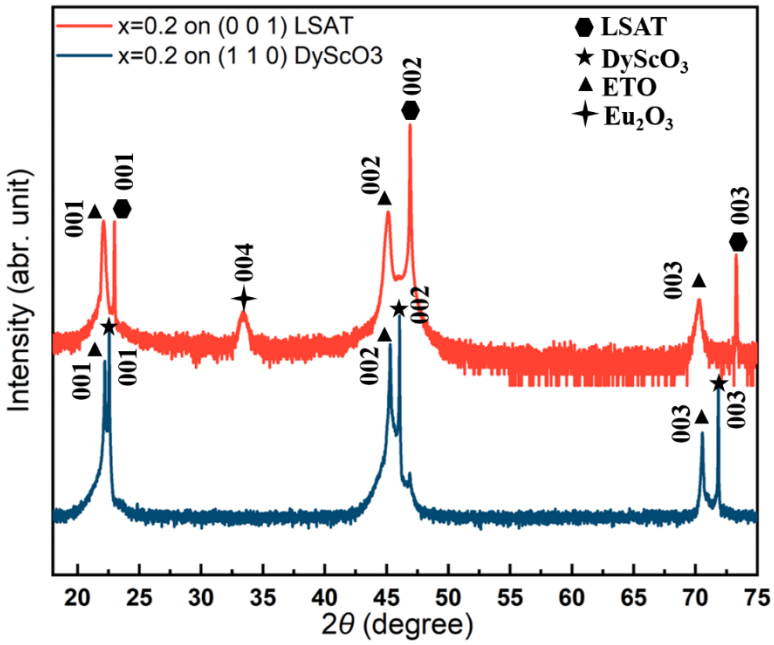

Figure 4.10 XRD 2θ-ω scans of $(ETO)_{0.8}$-$(Eu_2O_3)_{0.2}$ thin films grown on LSAT and $DyScO_3$.

4.4 Summary

In summary, systematic studies for optimizing the growth condition for ETO-based VAN thin films were carried out in this chapter. we carried out investigations for finding a suitable binary oxide second phase to incoporate with ETO. It was challenging since the growth condition suitable for growing ETO would not always be compatible with that of the binary oxide. After various exploration, $(ETO)_{0.5}$-$(Eu_2O_3)_{0.5}$ was successfully fabricated on (0 0 1)-oriented STO under careful control of growth pressure, substrate temperature and laser repetition rate. Finally, the optimized growth condition (laser repletion rate of 3 Hz, substrate temperature of 710 ^oC and growth pressure of $1\text{-}2\cdot10^{-6}$ Torr) was confirmed to make the $(ETO)_{1-x}$-$(Eu_2O_3)_x$ (x = 0.2, 0.25, 0.33, 0.5) epitaxial thin film on STO substrate with preferred OOP orientation.

Chapter 5. 3D strain induced magnetic phase transition in ETO using VAN structure and giant cryogenic magnetic entropy changes in $(ETO)_{0.8}$-$(Eu_2O_3)_{0.2}$ VAN film – Results and discussions

As introduced in Section 2.2 and 2.3, exploring the magnetic interactions and underlying mechanism of emergent FM in strained ETO films is critical to fully understand the mechanism of electrical field-controlled magnetism in ETO. Previous work has reported that the magnetic ground state of ETO could be switched by biaxial tensile strain [16,82], volume expansion [83], and electric fields [80]. For a 1.1% biaxial tensile strain on (1 1 0)-oriented $DyScO_3$ substrate [16], a spin-phonon-driven destabilization of the lattice induces a FE-FM phase in ETO with a low-lying state competing with a PE-AF phase [15]. Also, large lattice volume expansions of 1.56% ($LaAlO_3$), 2.41% ($SrTiO_3$) and 3.92% ($DyScO_3$) caused by the lattice mismatch between ETO and the substrates [83], ETO was again strained to become FM from AF. The result was explained by the exchange coupling constants variation with the changes of lattice volume [84,85,138]. In addition, under "moderate" compressive strain, an applied electric filed was found to eliminate long-range AF order in ETO films grown on (001)-oriented LSAT substrates, inducing a magnetic state with nanometer-sized FM clusters. This was explained by the modification of local exchange coupling via the electric field [80]. DFT calculations have been carried out to explain and understand these phenomena [15,80,84,85,138].

All the above works were focused on biaxial strained ETO films with a thickness < 25nm. Different scenarios were used for explaining the FM phase obtained, but there is no clear consensus of its origin. So far, three major magnetic interactions are reckoned to be crucial for determining the magnetic ground states of ETO as mentioned in Section 2.3, the latest proposal was that the 3rd NN interactions play an unneglectable role in determining magnetic ground state and the strength of this superexchange interaction relies upon the bond angle and the bond length of Eu-Ti-Eu along the {111} direction [80].

Referring to the Goodenough-Kanamori-Anderson rules [139–142], we know that the superexchange interaction *J* depends strongly on bond angle rather than on bond length. In this case, it can be concluded that the tiny modification of the Eu-Ti-Eu bond angle along {111}

direction would significantly affect the Eu-Ti-Eu superexchange and then change the magnetic ground state in ETO. However, to the best of our knowledge, experimental investigations of the Eu-Ti-Eu bond angle and its influence on the magnetic properties of ETO have not been reported. In standard epitaxial ETO films, in-plane (IP) biaxial tension (compression) along [001]/ [010] leads to out-of-plane (OOP) compression (tension) along [100] via the Possion effect, which means that the [111] bond length cannot be expanded (compressed) to any great extent, and hence the Eu-Ti-Eu superexchange coupling cannot be tuned significantly.

To systematically tune the strain along {111} and to understand the critical role of the Eu^{2+}-Ti^{4+}-Eu^{2+} superexchange coupling in controlling the magnetic ground states, the VAN approach is ideal as the vertical out-of-plane strain is tuned *independently* of the in-plane strain. The strain is not diminished with the film thickness (up to *u*m) [47,143,144], and so any spurious effects arising from substrate-induced dead layers in very thin (<10 nm) coherently strained films is eliminated. Furthermore, systematic strain tuning is enabled simply by changing the ratios of the phases in VAN system.

In this chapter, we demonstrate the control of the molar ratio of Eu_2O_3 (EO) in $EuTiO_3$ (ETO) VAN films, from 20% to 50% (20%, 25%, 33% and 50%) will lead to the systematically change of vertical strain and hence local structure and magnetic properties of ETO. STEM and atomic simulation are carried out to study the Eu-Ti-Eu bond angle change along [111] direction. Density functional theory calculations are performed to confirm the magnetism in ETO being modified by vertical strain.

As introduced in Section 2.4, magnetocaloric effect has been intensively studied in ETO-based bulk materials, such as $EuTiO_3$ [20,21], $Eu_{1-x}Ba_xTiO_3$ [22], $Eu_{1-x}La_xTiO_3$ [23], $Eu_{1-x}Sr_xTiO_3$ [24], $EuTi_{1-x}Cr_xO_3$ [25], $EuTi_{1-x}Nb_xO_3$ [26], $EuTi_{1-x}Fe_xO_3$ [27], $EuTi_{0.9}V_{0.1}O_3$ [28], for they are very promising magnetic refrigeration materials working under cryogenic temperature showing large adiabatic temperature change and magnetic entropy change under low magnetic field.

To best of our knowledge, the magnetocaloric effect on the ETO-based thin films has not been reported. Exploring the magnetocaloric materials at the nanoscale are fascinating since it can unlock regions of parameter space that are inaccessible to modern bulk synthesis techniques, such as exploiting interface, strain effects or tuning properties by geometric confinement. Comparing

to bulk materials, magnetocaloric materials explored in thin films exhibits reduced maximum entropy change and enhanced temperature breadth due to finite size effects and defects [145].

At the end of this chapter, magnetic entropy changes characterizations on $(EuTiO_3)_{1-x}$-$(Eu_2O_3)_x$ (x= 0.2, 0.5) thin films were carried out. Giant magnetic entropy change ($-\Delta S_{max}$ = 31.4 J/kg·K at ΔH = 2T) was observed in $(ETO)_{0.8}$-$(Eu_2O_3)_{0.2}$ VAN thin film, which is higher than the literature reported single crystal bulk ETO [20] ($-\Delta S_{max}$ = 23 J/kg·K at ΔH = 2T) or polycrystal bulk ETO [21] ($-\Delta S_{max}$ = 22.3 J/kg·K at ΔH = 2T).

5.1 Fabrication of $(ETO)_{1-x}$-$(Eu_2O_3)_x$ (x=0, 0.2, 0.25, 0.33, 0.5, 1) thin films

As shown in Table 5.1, thin films of $(EuTiO_3)_{1-x}$-$(Eu_2O_3)_x$ (x=0, 0.2, 0.25, 0.33, 0.5, 1) were grown on (001)-oriented STO using the optimized parameter confirmed in Section 4.3, the thickness of all the thin films were controlled to be around 220 nm. STO was selected as substrate for the system since it is a non- magnetic material with the same structure and lattice parameter as bulk ETO (a = 3.905 Å for bulk STO [146]; a = 3.905 Å for bulk ETO [14]), which is ideal for the epitaxial growth of high quality ETO thin films. Non-magnetic Eu_2O_3 is ideal secondary phase in this study not only because the merits mentioned in Section 4.2 but also it is confirmed to be compatible with the growth condition of pure ETO. In this $(EuTiO_3)_{1-x}$-$(Eu_2O_3)_x$ (x=0.2, 0.25, 0.33, 0.5) on STO system, as shown in Figure 5.1, with increasing fractions of the second phase Eu_2O_3, the distance between nanopillars will decrease and so more of the ETO will be vertically strained (i.e. less in-plane relaxation of the ETO lattice). Hence larger fractions of EO added to ETO are expected to produce larger out-of-plane strain in the ETO. At the same time, the in-plane strain is not modified as the ETO are all grown coherently on STO.

Table 5.1 Growth parameters of $(ETO)_{1-x}$-$(Eu_2O_3)_x$ (x=0, 0.2, 0.25, 0.33, 0.5) thin films grown on (0 0 1)-oriented STO substrates.

$(ETO)_{1-x}$-$(Eu_2O_3)_x$	Laser Repetition Rate (Hz)	Temperature (°C)	Growth Pressure (Torr)	Substrate	Thin Film Thickness (nm)
Film 1, x = 0	3	710	$1\text{-}2\cdot10^{-6}$	(0 0 1)-oriented STO	234
Film 2, x = 0.2					201
Film 3, x = 0.25					217
Film 4, x = 0.33					227
Film 5, x = 0.5					231
Film 6, x = 1					223

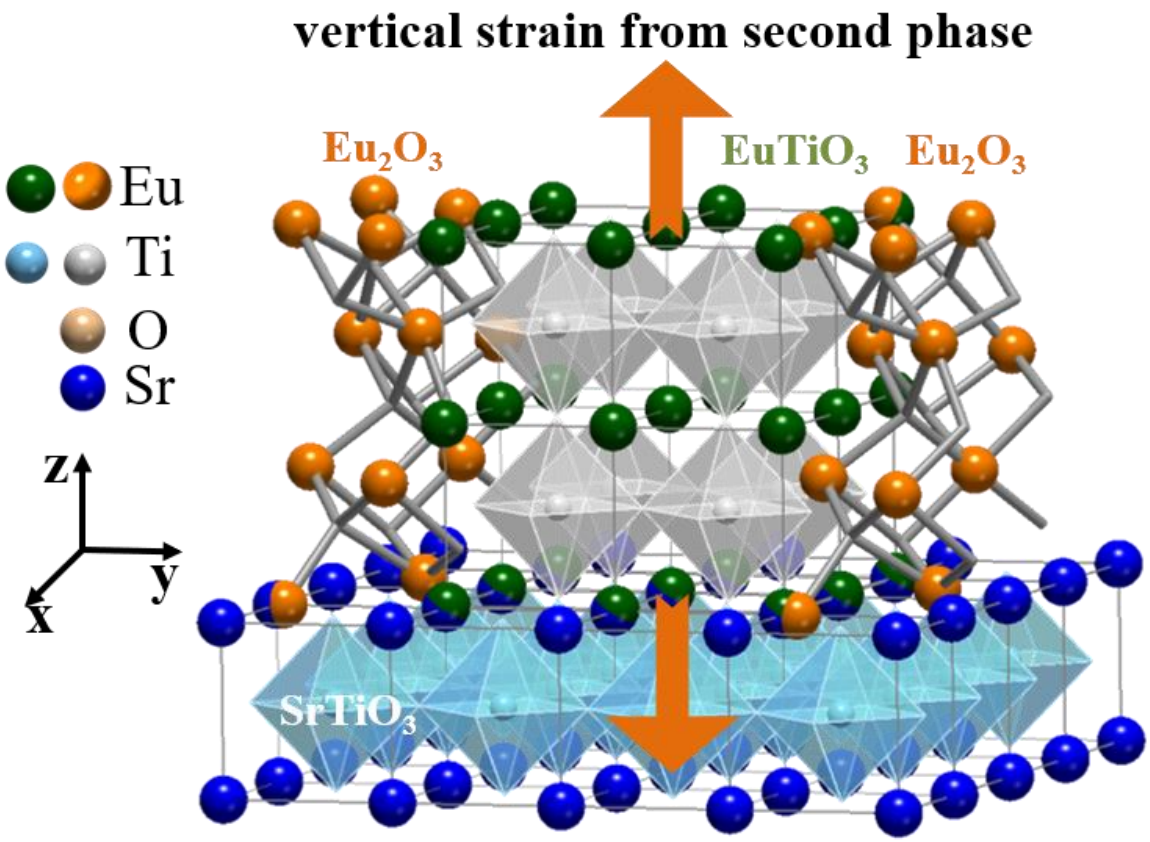

Figure 5.1 Schematic of self-assembled $EuTiO_3$-Eu2O3 nanocomposite thin films. Eu_2O_3 serves as a second phase in nanopillar form to provide out-of-plane tensile strain in $EuTiO_3$.

5.2 Strain states analysis of ETO in $(ETO)_{1-x}$-$(Eu_2O_3)_x$ (x=0, 0.2, 0.25, 0.33, 0.5) thin films using XRD

To investigate the strain states of ETO in $(EuTiO_3)_{1-x}$-$(Eu_2O_3)_x$ (x = 0.2, 0.25, 0.33, 0.5) thin films, XRD 2θ-ω scans were carried out on these samples to determine the OOP lattice parameters of ETO while reciprocal space map (RSM) were carried out near the STO 1 0 3 peaks to confirm the OOP lattice parameters and determine the IP lattice parameters. In order to give a more straightforward comparison, XRD 2θ-ω scans of pure $EuTiO_3$ and Eu_2O_3 thin films were added and Figure 4.9 was redraw as Figure 5.2, the XRD 2θ-ω scans of plain ETO (x=0), ETO-Eu_2O_3 VAN nanocomposite films (x=0.2, 0.25, 0.33, 0.5), and plain Eu_2O_3 (x=1) show only *0 0 l* peaks from ETO, Eu_2O_3 and STO substrates, indicating the epitaxial growth of ETO and Eu_2O_3 phases in the VAN thin films. Apart from the expected ETO, Eu_2O_3 and STO phases, no impurity phases are detected.

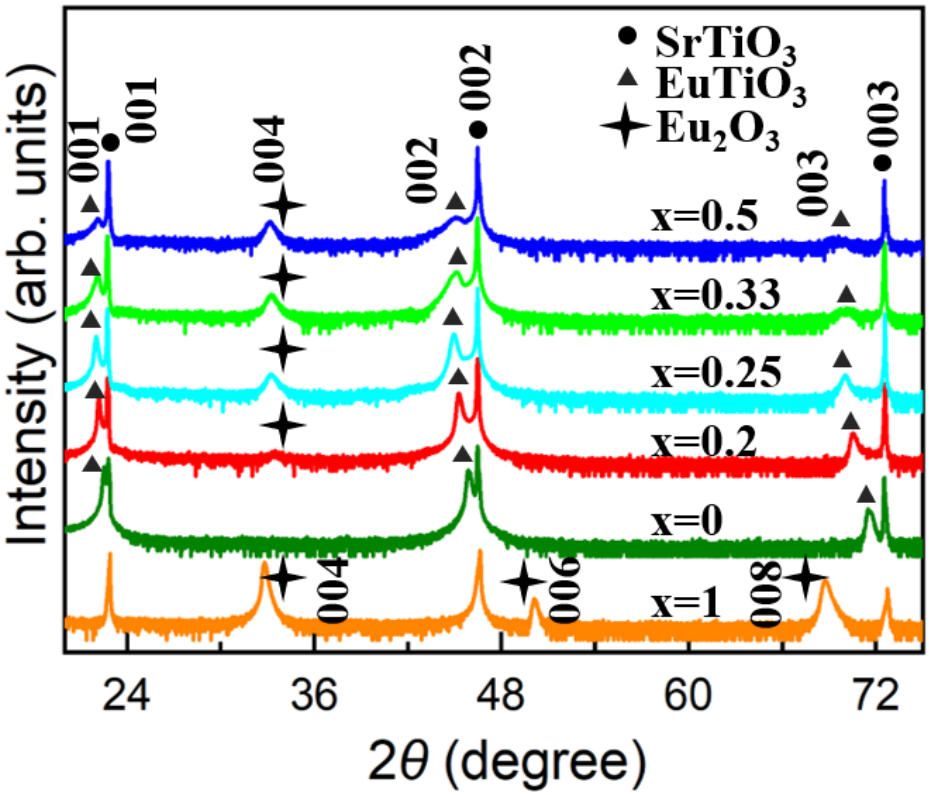

Figure 5.2 XRD 2θ-ω scans of plain ETO (x=0), ETO-Eu_2O_3 VAN nanocomposite films (x=0.2, 0.25, 0.33, 0.5), and plain Eu_2O_3 (x=1).

As shown in Figure 5.3, the relative peak heights of the ETO and Eu_2O_3 phases vary in accordance the phase fraction at the selected range where Eu_2O_3, ETO and STO are included. A rise of the Eu_2O_3 peaks started to show up and follows by a decrease of ETO peaks as the fraction of Eu_2O_3 changed from x = 0 to x = 0.5. The position of the *0 0 l* peaks for ETO show a general trend of decreasing 2θ (increasing *d* spacing, and hence larger '*c*') with larger EO fraction, indicating that the different levels of vertical strain states were induced as varying the fraction of EO.

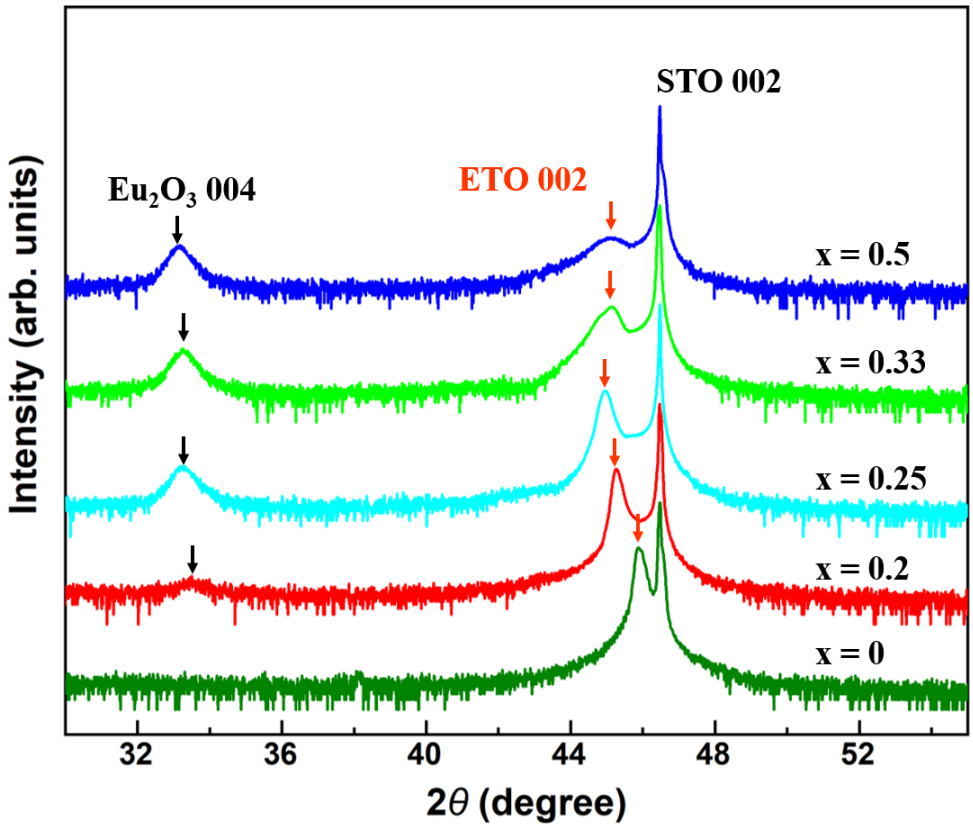

Figure 5.3 Selected range XRD 2θ-ω patterns of plain ETO (x=0) and ETO-Eu_2O_3 VAN nanocomposite films (x=0.2, 0.25, 0.33, 0.5).

As shown in Figure 5.4, RSM of plain ETO (x= 0) and ETO-Eu_2O_3 VAN films (x= 0.2, 0.25, 0.33, 0.5) near the STO 1 0 3 peak were measured. For both the plain ETO and the VAN ETO-EO films, the ETO 1 0 3 peaks have the same Q_{in} values as the STO 1 0 3 peaks, indicating that the IP lattice parameters of ETO are the same as that for the STO substrate (*a*STO = *a*ETO = *b*STO = *b*ETO = 3.905 Å). The OOP lattice parameter for ETO, is indicated by the red dash lines in the RSM. With increasing EO fraction, the OOP lattice parameter of ETO is increased from *c*ETO =

3.950 Å (film 1, x= 0) to *c*ETO = 4.028 Å (film 5, x= 0.5). ETO peak in x = 0.5 showed like a line shape was caused by relative low intensity of (1 0 3) ETO, which was comparable to background signal noise from XRD system.

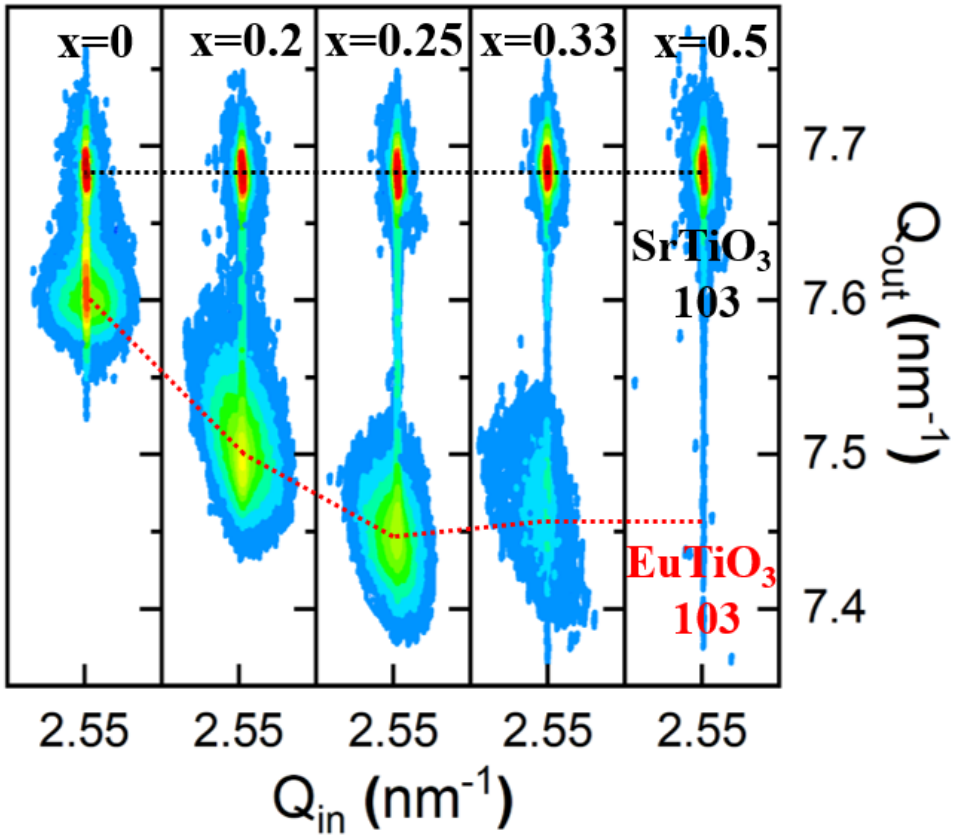

Figure 5.4 Reciprocal space maps of plain ETO and nanocomposite films around STO 1 0 3 and ETO 1 0 3 peaks.

The IP lattice parameters, OOP lattice parameters, tetragonal distortions and vertical strains of the ETO in these samples were summarized as shown in Table 5.2. The error bars introduced were caused by peak broadening and the step size of individual 2θ-ω scans. The OOP lattice constant is saturated when the EO fraction reaches x= 0.25. If we compare the lateral width of the ETO between the embedded EO nanofeatures for the x= 0.2 and 0.5 in the TEM images in Figures 5.5 (a) and 5.5 (d, e) in Section 5.3, the values are up to ~ 50 nm, and ~5 -30 nm, respectively. These values are estimated and averaged from multiple images. The latter spacing is certainly small enough that the ETO *c*-parameter cannot laterally increase between the nanopillars. This explains

the flattening of the *c*-parameter rise with increasing x, which will take place when the spacing of the ETO between pillars is below around 20 nm [56].

Table 5.2 The IP lattice parameters, OOP lattice parameters, tetragonal distortions and vertical strains of the ETO in plain ETO (x=0) and ETO-Eu_2O_3 VAN nanocomposite films (x=0.2, 0.25, 0.33, 0.5).

$(ETO)_{1-x}$-$(Eu_2O_3)_x$	OOP Lattice Parameter *c* of ETO (Å)	IP Lattice Parameter *a* of ETO (Å)	Tetragonal Distortion *c*/*a*	Vertical Strain (%)
Film 1, x = 0	3.950±0.005	3.905±0.005	1.012±0.005	1.15
Film 2, x = 0.2	4.002±0.005		1.025±0.005	2.48
Film 3, x = 0.25	4.029±0.005		1.032±0.005	3.18
Film 4, x = 0.33	4.019±0.005		1.029±0.005	2.92
Film 5, x = 0.5	4.028±0.005		1.031±0.005	3.15

5.3 TEM and STEM characterizations of $(ETO)_{1-x}$-$(Eu_2O_3)_x$ (x=0.2, 0.5) VAN thin films

TEM and STEM characterizations were carried out on $(ETO)_{1-x}$-$(Eu_2O_3)_x$ (x= 0.2 and 0.5) VAN nanocomposite films to investigate their crystallographic structure at atomic level and phase morphologies.

Comparing the (S)TEM images for the x=0.2 and x=0.5 samples (Figures 5.5 a-c, *cf.* Figures 5.5 d-f), we first observe that the ETO appears as a lighter contrast phase (as expected for the lower atomic weight). Next, we observe that columns of EO embedded in the ETO are not fully continuous in the x=0.2 sample (Figures 5.5 a-e) but become continuous for the x=0.5 sample (Figures 5.5 d-f). We can therefor label the composite types as 0-3 (Figure 5.5 c) [147] and 1-3 (Figure 5.5 f) [48], for x=0.2 and 0.5, respectively. We shade the ETO phase green and EO phase yellow in Figs. 2c, d and g to show the 2 phases more clearly. We also observe the ETO nucleates and grows first on the STO substrate (Figures 5.5 a and d) as expected because of lower interfacial energy of the two crystallographically identical structures. Also, as observed from the HRTEM images

(Figures 5.5 b and e), both EO and ETO phases are highly crystalline for x = 0.2 and 0.5 and the interfaces between the phases are very clean.

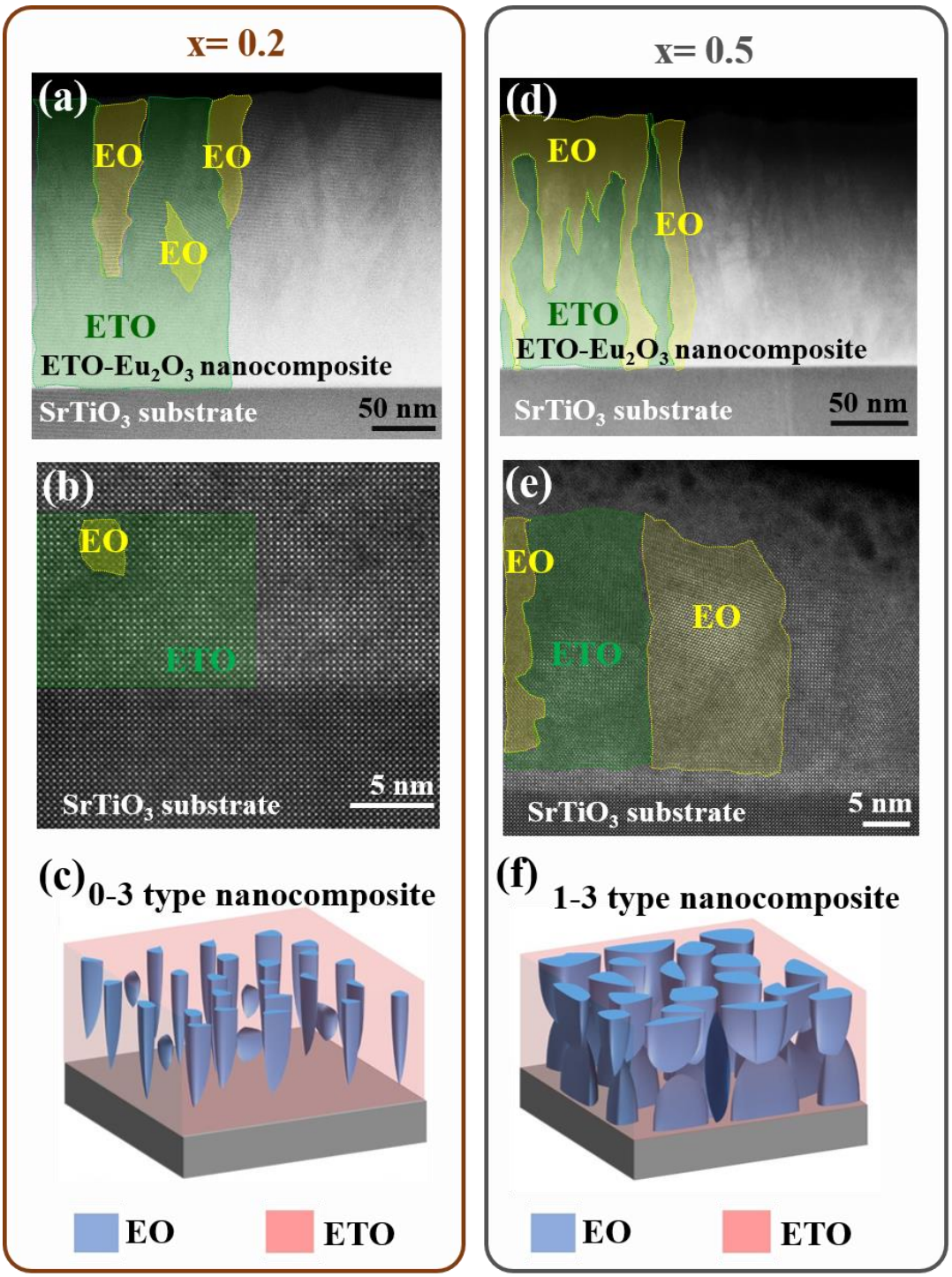

Figure 5.5 (a, b, c) TEM and STEM characterization and schenmatic type of film 2 (x = 0.2); (d, e, f) TEM and STEM characterization and schenmatic type of film 5 (x = 0.5).

To exclude the possible existence of Eu-rich phases, $Eu_2Ti_2O_7$, Eu_2TiO_5, Eu_2TiO_4, $Eu_3Ti_2O_7$ [76,148] which could possibly form, we investigated selected area electron diffraction (SAED) patterns x = 0.2 sample. As shown in Figure 5.6, only EO diffraction patters are detected, there is no evidence of the above ternary phase, and hence the magnetic properties measured later originated from ETO only (EO is nonmagnetic).

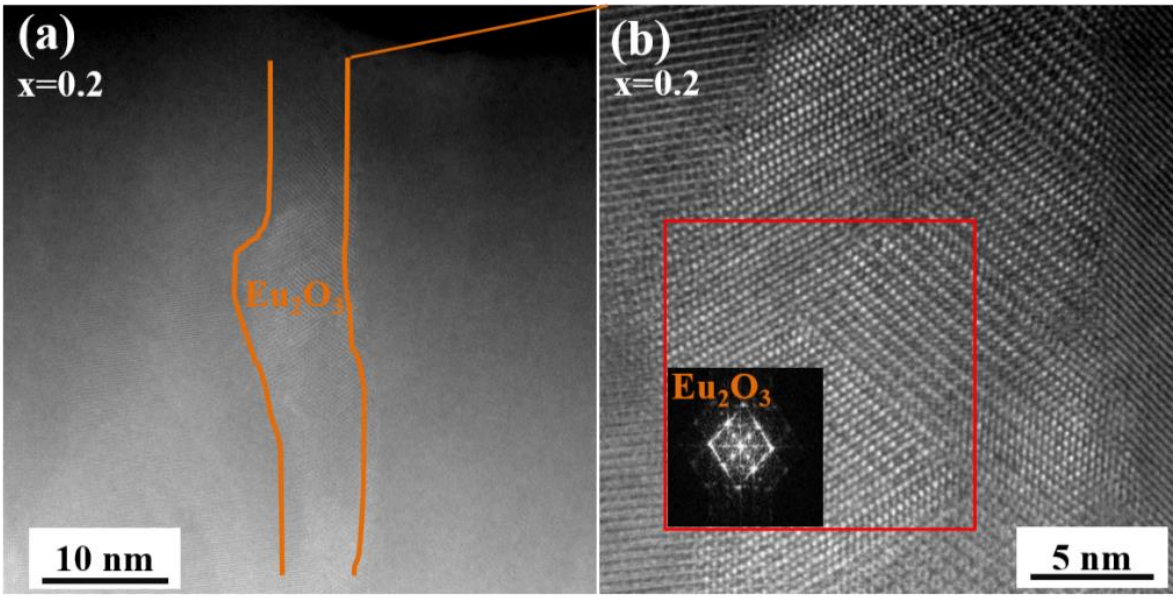

Figure 5.6 (a, b) Zoomed in region of x = 0.2 (film 2) and related SAED.

5.4 Magnetic properties characterizations of $(ETO)_{1-x}$-$(Eu_2O_3)_x$ (x=0, 0.2, 0.25, 0.33, 0.5) thin films using SQUID

To investigate the magnetic properties of the ETO, temperature-dependent magnetization and magnetic field-dependent magnetization were carried out using SQUID. Since there is no magnetization contribution from Eu^{3+}, the measured magnetization is ascribed to Eu^{2+} from the ETO phase [149,150]. M-T curves obtained by field-cooling under 100 Oe are shown in Figure 5.7 (a), FM-like behavior is observed for all VAN films (x=0.2, 0.25, 0.33, and 0.5). This result is sharply different to plain epitaxial ETO films in the literature which overwhelmingly show AF behavior. There is only one exception where the OOP lattice parameter is reduced, and FM behavior has been shown [16]. This point will be discussed later in this section. By taking the 1st derivate of *M-T* curves, transition temperature (T_c) values of around 3 K were obtained (listed in Table 5.3). T_c is

independent of vertical strain. Magnetic hysteresis loops (magnetization vs. magnetic field, *M-H*) were measured along the a-b plane of ETO at 2 K as shown in Figure 5.7 (b). Here it should be noted that only ETO contributes to the magnetization since EO and STO are non-magnetic. The values of magnetic moment (*M*) obtained at 2K and 500 Oe field, as well as the coercivity fields (H_c) are summarized in Table 5.3.

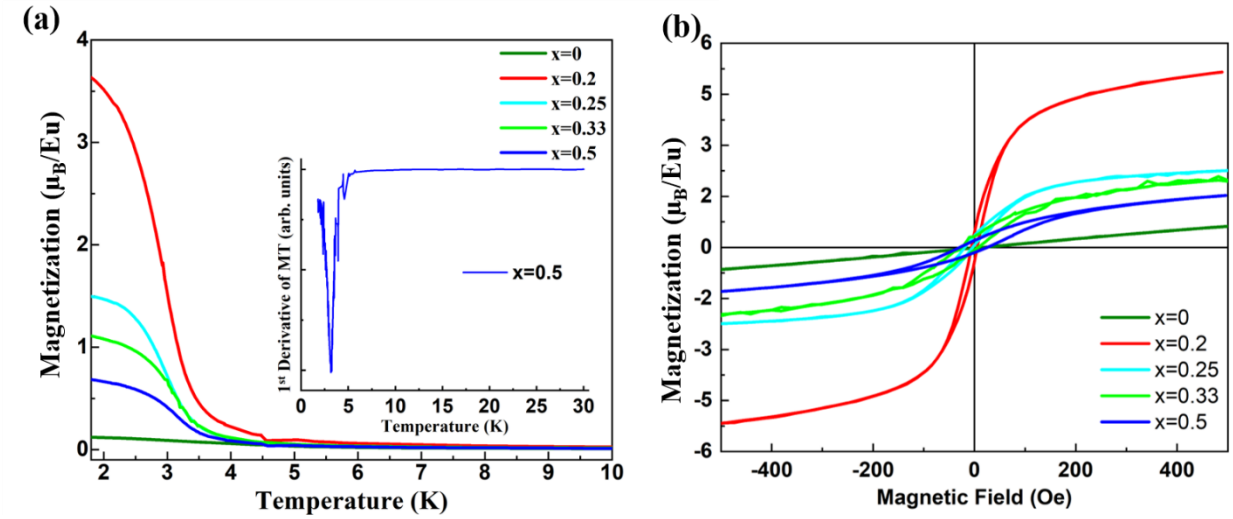

Figure 5.7 (a) Temperature-dependent magnetization measured from 1.8 K to 30 K of plain film (x = 0) and nanocomposite films (x = 0.2, 0.25, 0.33, 0.5) (field-cool under 100 Oe). The inset shows 1st derivation M-T of x = 0.5. (b) Magnetic hysteresis loops of plain film and nanocomposite films measured at 2 K.

Table 5.3 The magnetic properties of the ETO in plain ETO (x=0) and ETO-Eu_2O_3 VAN nanocomposite films (x=0.2, 0.25, 0.33, 0.5).

$(ETO)_{1-x}$-$(Eu_2O_3)_x$	***T_c* (K)**	***M*** **2K 500 Oe (μ_B/Eu)**	***H_c*(Oe)**
Film 1, x = 0	PM	0.62	0
Film 2, x = 0.2	3.00	5.15	5.74
Film 3, x = 0.25	2.98	2.26	7.09
Film 4, x = 0.33	3.00	1.96	16.77
Film 5, x = 0.5	3.12	1.46	26.23

Comparing the Table 5.2 and 5.3, we can see that *M* decreases from 5.15 μ_B/Eu on going from *c/a* = 1.025 (x = 0.2) to 1.031 (x = 0.5), while H_c increases continuously, with increasing *c/a*, from

5.74 Oe to 26.23 Oe. We compare our results to previous experimental works [14,16,83,128] and theoretical calculation [15,16], in a diagram showing OOP lattice parameter *versus* IP parameter for ETO films with magnetic properties indicated. We also show lines of constant *c/a*. Theoretically [15,16], due to spin-lattice coupling effect in single phase ETO, the boundaries of ferromagnetism for ETO lie at above the value of *c/a* = 1.02 (vertical strain case) or below the value of 0.99 (horizonal strain case) as shown in Figure 5.8. Our x = 0.2 VAN film has *c/a* (1.025±0.005). This is very close to the theoretical boundary, so both AF and FM interactions likely exist in the film. This explains why H_c is rather small (5.74 Oe), since in un-strained or bulk ETO [16,128] (purely AF), H_c would be 0 Oe. For the x=0.5 VAN film, the *c/a* is 1.031, far higher than the boundary value (1.02), so FM interactions dominate. This explains the high H_c value of 26.23 Oe (measured at 2K), since in strained ETO [16] (ETO on $DyScO_3$), H_c is around 50 Oe (measured at 1.8K). In addition, the very high *c/a* values were achieved using VAN structures to induce this level of tetragonality into plain films without external pressure. Hence, we confirm clearly the theoretical predictions of the FM zone being at high *c/a*.

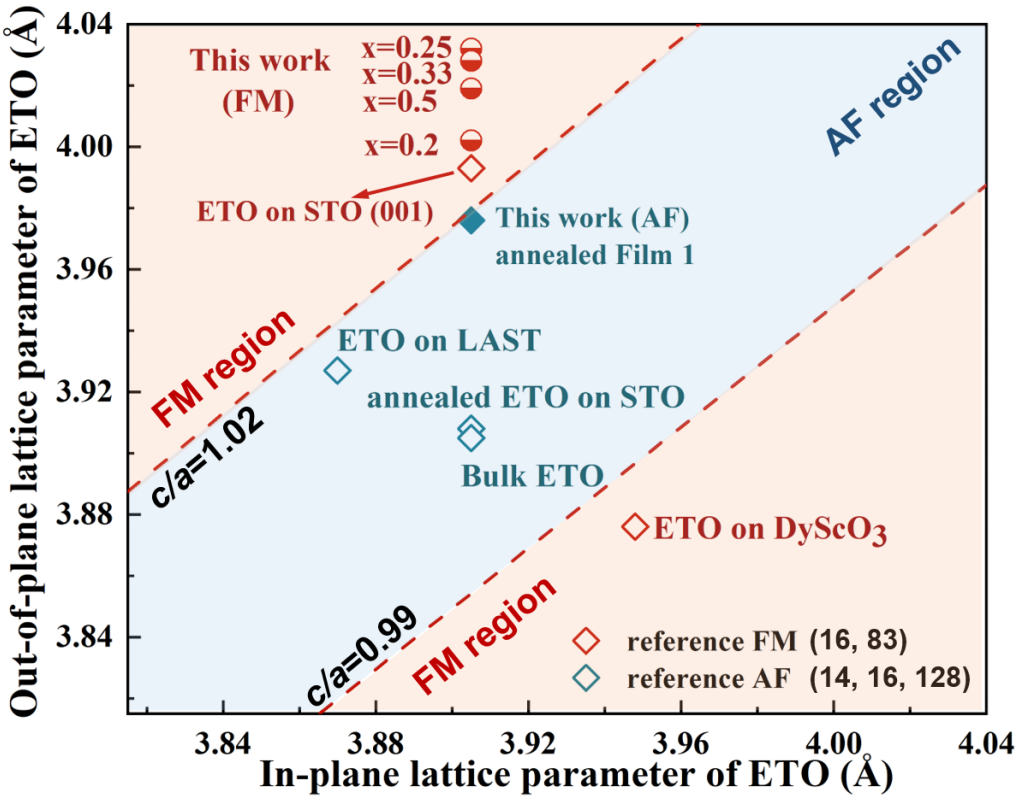

Figure 5.8 Phase diagram for both strained- and unstrained-ETO showing the relationship between tetragonal distortion and magnetic properties.

5.5 Atomic column study of $(ETO)_{1-x}$-$(Eu_2O_3)_x$ (x= 0.2, 0.5) VAN films using Atomap

As introduced before, the magnetic ground states of ETO are strongly determined by the Eu-Ti-Eu superexchange interactions along the {1 1 1} directions [80]. To understand the magnetic behavior evolutions of ETO in the VAN films with increasing *c*/*a* (increasing EO) fraction, atomic column simulations of Eu and Ti ion positions along [0 0 1]/[0 1 0] direction in STEM images for the x = 0.2 and x = 0.5 were performed using Atomap software [122].

The ETO phase region (shaded green) analyzed were the area adjacent to the EO regions as shown in Figures 5.9 (a) and (b) for x=0.2 and 0.5, respectively. The position of Eu and Ti columns are shown as red and blue dots in the inset figures in Figures 5.9 (a) and (b), respectively. The method of how to identify atomic columns in the images are introduced in Section 3.2.

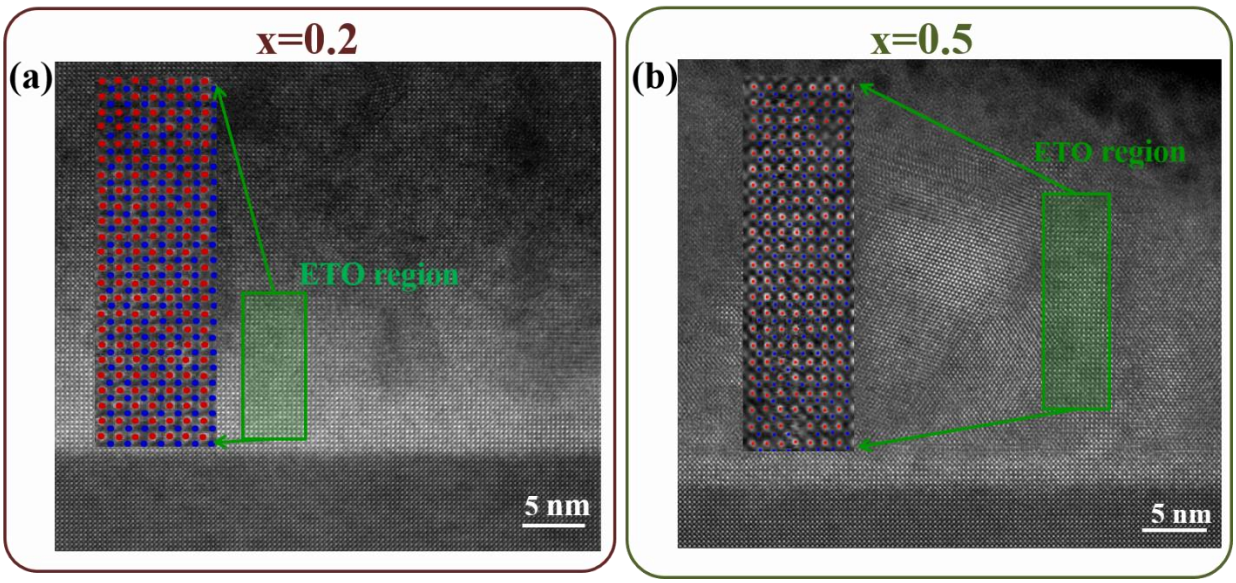

Figure 5.9 (a, b) Atomic column sumulations on ETO region adjacent to EO regions for x = 0.2 and 0.5 VAN films, repectively.

After knowing the column positions of both Eu and Ti, Ti position shift along [0 0 1] direction can be defined as:

$$Ti\ shift = \frac{L2}{L1 + L2} = \frac{Area2}{Area1 + Area2} = \frac{|V4 \times V5|}{|V1 \times V2| + |V4 \times V5|}$$

where $L2$ and $L1$ are the distances from Ti position to upper Eu planes and lower Eu planes, respectively; $Area2$ and $Area1$ are the triangle areas of Ti with two upper nearest Eu and two lower nearest Eu, respectively; Vx (x = 1, 2, 4, 5) are the vectors from Ti to its nearest Eu, as shown in Figure 5.10.

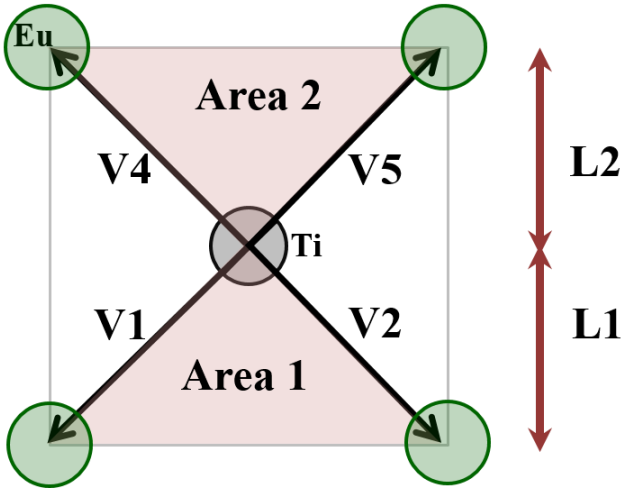

Figure 5.10 Schematic of Ti position shift along [0 0 1] direction.

The statistic Ti shift along [001] was determined and is shown in Figure 5.11 (a) and (b), respectively. The red dots indicate the percentage of distance from Ti to the upper Eu planes (along the [001] direction) compared to two adjacent Eu planes, which are larger than 0.5 while blue ones are for percentage distances less than 0.5. The mean value (statistically) of Ti shift in x=0.2 VAN film is 0.498 (with standard deviation of 0.018) while the mean value of Ti shift for the x=0.5 VAN film is 0.488 (with standard deviation of 0.021).

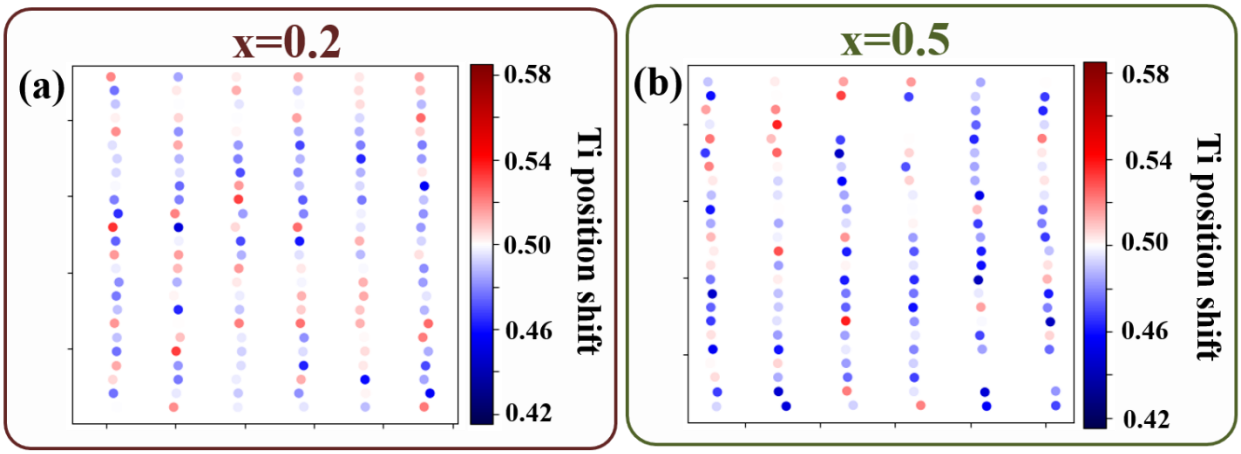

Figure 5.11 (a, b) The statistic Ti shift along [001] for x=0.2 and 0.5 VAN films, respectively.

Assuming the shift only occurs along z axis (only vertical strain introduced in our samples), combined with lattice parameters obtained from XRD analysis, Ti position around tetragonal center can be determined.

As shown in Figure 5.12, for x=0.2 (film 2), lattice parameters are a_{ETO}=b_{ETO}=3.905 Å, c_{ETO}=4.002 Å. So, the position of Ti should be (1.9525, 1.9525, 2.009), and Eu ions are: Eu_8 (3.905, 0, 4.002) and Eu_2 (0, 3.905, 0), so the Eu-Ti-Eu angle along [111] direction <Eu_8-Ti-Eu_2> is 179.78°. For x=0.5 (film 5), lattice parameters are a_{ETO}=b_{ETO}=3.905 Å, c_{ETO}=4.028 Å. So, the position of Ti should be (1.9525, 1.9525, 2.062), and Eu ions are: Eu_8 (3.905, 0, 4.028) and Eu_2 (0, 3.905, 0), so the Eu-Ti-Eu angle along [111] direction <Eu_8-Ti-Eu_2> is 178.7°.

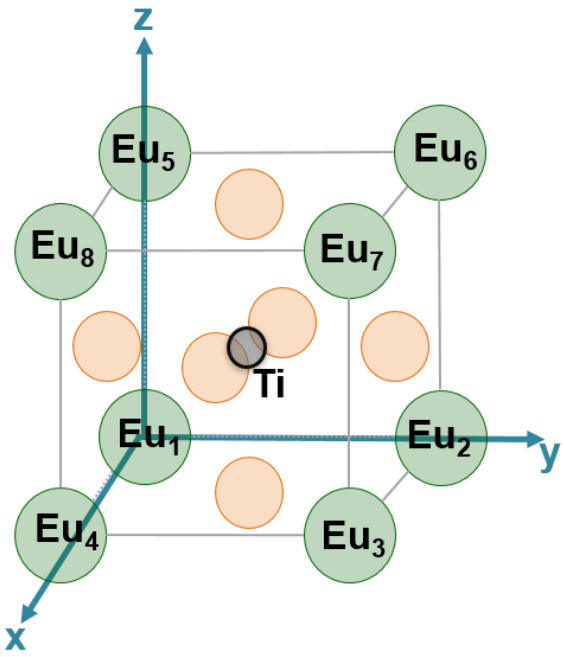

Figure 5.12 Schematic of ETO unit cell.

Taking the standard deviation from statistical analysis and error induced by pixels in STEM images, the Eu-Ti-Eu bond angle along [111] is calculated to be 179.78° ± 0.80° in x=0.2 (Figure 5.13 a) and 178.70° ± 0.83° in x=0.5 (Figure 5.13 b). In both films, the Eu-Ti-Eu bond angle is slightly less than 180°, but it is more than 1° lower in the x=0.5 film. A lower bond angle corresponds to a weaker AF interaction because of the Goodenough-Kanamori-Anderson rules [139–142] mentioned at the beginning of this chapter. This explains the observed larger H_c value (Figure

5.7 b) in the x=0.5 film. This is the first experimental determination of Eu-Ti-Eu bond angle in ETO and its strong influence on the resulting magnetic properties is very clear.

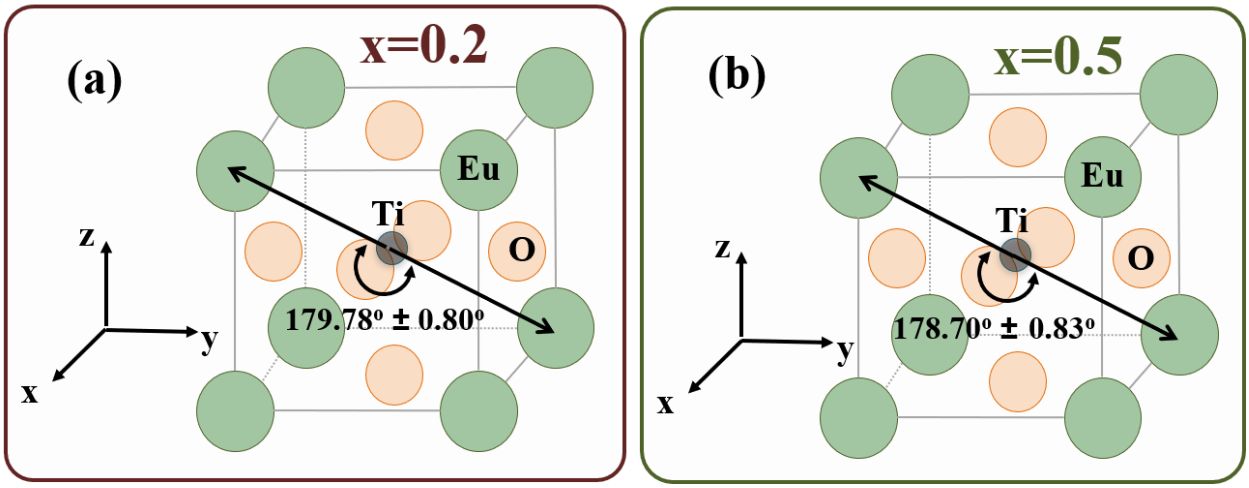

Figure 5.13 (a, b) Schematic bond angle determined from atomic position for x = 0.2 and x = 0.5 VAN films, respectively.

5.6 DFT calculations on phase transition *versus* vertical strain

Our first-principles calculations were performed in the framework of density-functional theory as implemented in the Vienna ab initio simulation package (VASP) with a plane-wave cutoff of 650 eV [151,152]. The strong electron correlation effects on the f shells of Eu atoms was considered by using GGA+U scheme in Dudarev's approach with an on-site Coulomb parameter U = 5.7 eV and Hund's exchange J = 1.0 eV. The I4/mcm structure was chosen as ground state followed the previous study [153]. The 6×6×6 Monkhorst and Pack grid of k-point mesh was used for calculation. To confirm the obtained experimental results, partial density of states (PDOS) calculations were carried out under vertical strain states (1.92%, 2.4% and 3.2%), and the data is shown in Figure 5.14. The largest hybridization between the Eu, Ti and O orbitals is observed in the system when the vertical strain is ~2%. When the vertical strain is increased further, the hybridization between Eu, Ti and O orbitals weakens.

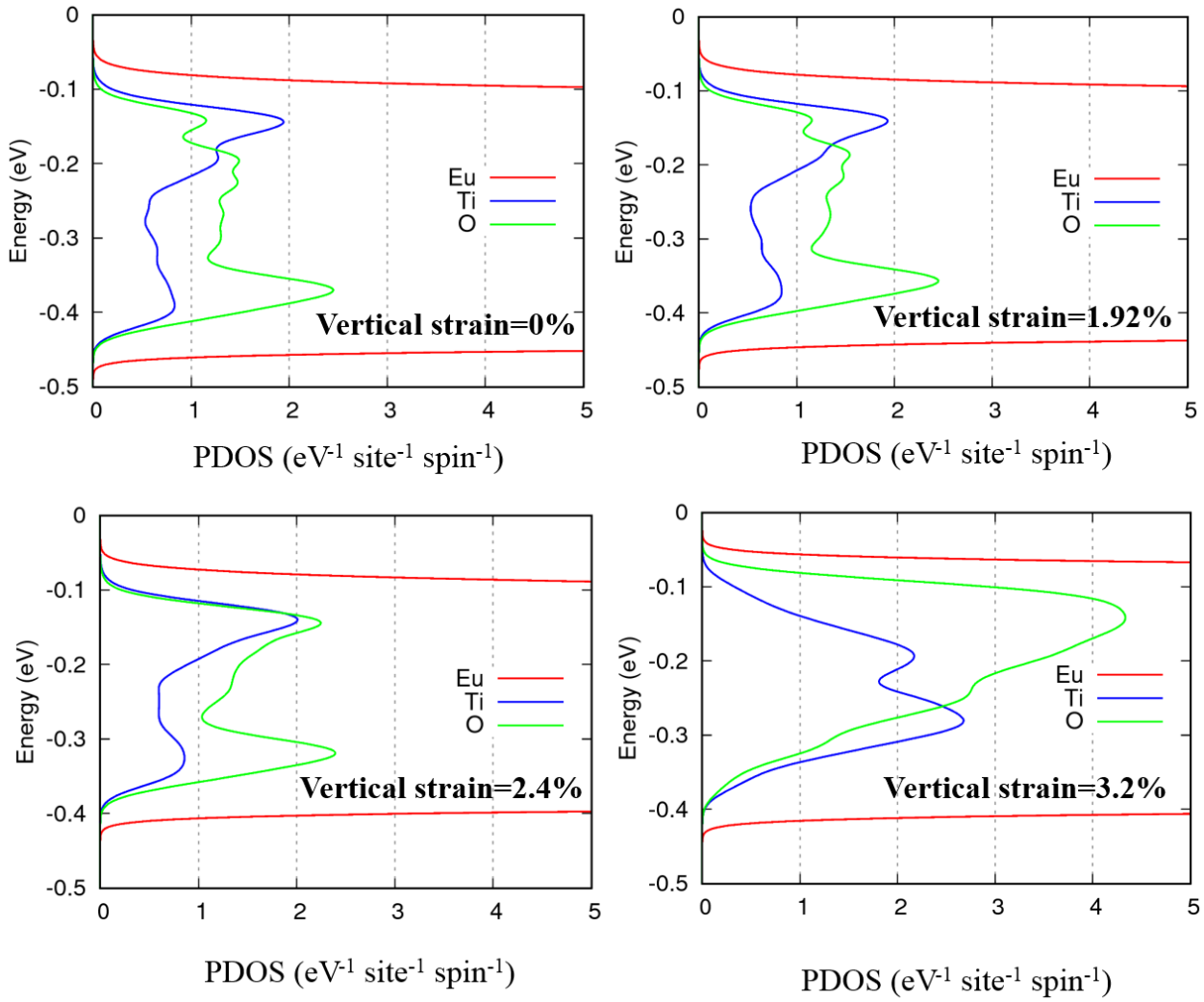

Figure 5.14 Site projected partial density of states (PDOS) under vertical strain states of 0%, 1.92%, 2.4% and 3.2%.

Figure 5.15 shows the total energies of the G-type AF magnetic configuration relative to FM configurations as a function of vertical strain. It is observed that the magnetic configuration is changed from G-type AF to FM with increasing strain, with the critical vertical strain point being around 2.5%.

For the x = 0.2 VAN film, the vertical strain is 2.48% (tetragonal distortion of c/a=1.025 (as shown in Table 5.2 and Figure 5.8). Hence, the x = 0.2 VAN film lies at the transition point and so both AF and FM interactions are expected to coexist in the film. Indeed, the magnetic properties shown in Figure 5.7 (a) and (b) confirm this, namely H_c is rather small (5.74 Oe) and M (5.15

μ_B/Eu) peaks at x=0.2, since in un-strained or bulk ETO [16,128] (purely AF), H_c is 0 Oe and M is 7 μ_B/Eu [128] (measured at 2K, 50000 Oe).

When the vertical strain is over 2.5%, as shown in Figure 5.15, FM interactions are stabilized in the ETO. This is consistent with the magnetic properties observed in the x=0.5 VAN film, namely the high H_c value of 26.23 Oe (measured at 2K) and M is rather small (1.46 μ_B/Eu), since in strained ETO [16] (ETO on $DyScO_3$), H_c is 50 Oe (measured at 1.8K) and M is ~3μ_B/Eu (measured at 1.8K, 400 Oe).

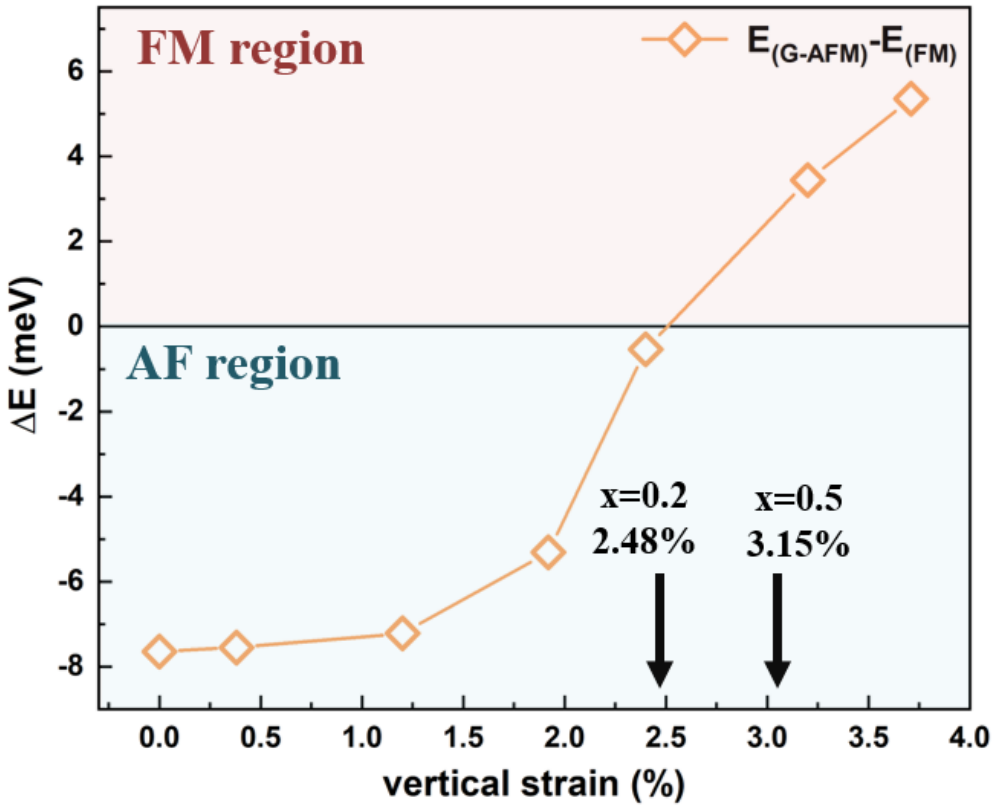

Figure 5.15 Total energies of G-type AF magnetic configuration relative to FM magnetic configuration as a function of vertical strain in ETO.

5.7 Proposed mechanism

An underlying mechanism to explain the observed experimental data is proposed in Figure 5.16 (a) and (b). As mentioned in Section 2.3, there are three major interactions coexisting in ETO [80]: (1) antiferromagnetic interactions between first-nearest-neighboring Eu^{2+} ions; (2) ferromagnetic

interactions derived from the indirect exchange coupling between second-nearest-neighboring Eu^{2+}; (3) antiferromagnetic interactions originated from superexchange interactions between third-nearest-neighboring Eu^{2+} ions via the Ti 3*d* band along {111} direction.

In its bulk form [75,85] (or post-annealed ETO thin film [128]), ETO has a cubic structure and the AF interaction is dominant, as shown in Figure 5.16 (a). In the VAN films, with increasing vertical strain, the Eu-Ti-Eu bond angle along {111} direction increasingly deviates from 180°. As a result, AF interactions in both 1st and 3rd NN Eu^{2+} ions (via Ti 3*d* band) and the FM interaction in 2nd NN Eu^{2+} ions become weaker, as shown in Figure 5.16 (b). However, the AF interactions becomes weaker at a greater rate than do the FM interactions. This is because the distance of Eu-Ti-Eu length (larger OOP lattice parameter) and deviation of Eu-Ti-Eu bond angle along [111] direction is increased simultaneously. Consequently, the FM interaction is dominant in the well-strained ETO (film 5, x = 0.5).

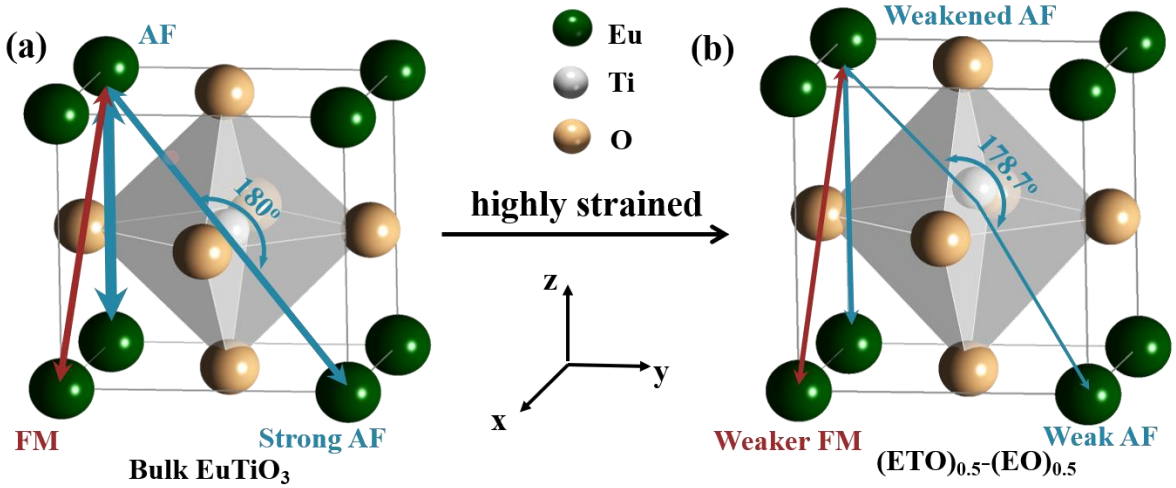

Figure 5.16 (a, b) Proposed mechanism explaining the change of Eu-Ti-Eu bond angle along [111] direction caused by vertical strain. Arrow thickness refer to the "strength" of magnetic interaction.

5.8 Giant cryogenic magnetic entropy change in $(ETO)_{0.8}$-$(Eu_2O_3)_{0.2}$ VAN thin films

As shown in Figure 5.17, the field dependence of magnetization for $(EuTiO_3)_{1-x}$-$(Eu_2O_3)_x$ (x = 0.2, 0.5) thin films at different temperatures from 2 to 54 K were measured. The magnetic contributions from STO substrate were subtracted at this point (Detailed data about the STO substrate will be introduced later). For x = 0.2 sample, in an applied field up to 7 T during both increasing and decreasing field at the temperature of 2 K show no magnetic hysteresis (not shown here), implying that the compound is a soft ferromagnet. The magnetic moment (at temperature of 2 K and magnetic field of 5 T) calculated to be 8.47 μ_B/Eu for x = 0.2 and 3.88 μ_B/Eu for x = 0.5. Theoretically, for completed alignment of all Eu^{2+} spins, the saturated magnetization M_s is expected to be 7 (± 1) μ_B/Eu [75]. It is easy to understand that for x = 0.5 sample (FM dominant), the average magnetization is 3.88 μ_B/Eu. This value is consistent with the reported average magnetization of ~3 μ_B/Eu in FM strained-ETO [82], indicating that there could also exist local inhomogeneity as reported previously in FM strained-ETO. The unexpected high value of magnetic moment (changes) in x = 0.2 film lead us to expect a large magnetic entropy change in this sample.

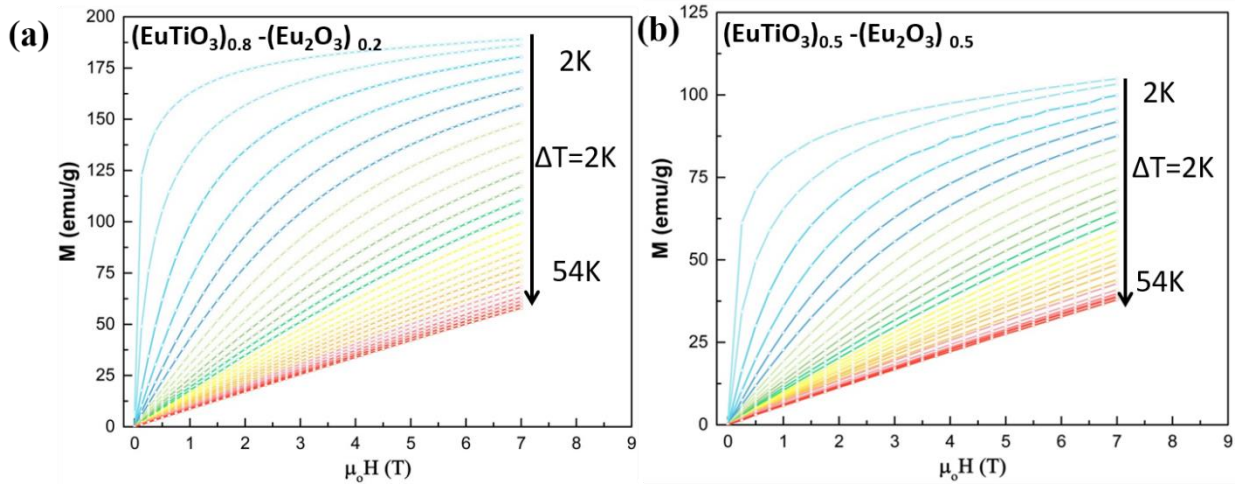

Figure 5.17 (a, b) Field dependence of magnetization for $(EuTiO_3)_{1-x}$-$(Eu_2O_3)_x$ (x = 0.5, 0.2) thin films at different temperatures from 2 to 54 K.

To exclude the magnetic contribution from the substrate STO and second phase EO, pure Eu_2O_3 was deposited on (0 0 1)-oriented STO (5·5·0.5 mm^3) using the same growth parameters as

$(EuTiO_3)_{1-x}$-$(Eu_2O_3)_x$ VAN thin films as shown in Table 5.1. The film thickness was measured to be 226 nm. XRD 2θ-ω scan of pure Eu_2O_3 as shown in Figure 5.18 (a) indicates only pure Eu_2O_3 phase in this sample. OOP lattice parameter and IP lattice parameter of Eu_2O_3 were confirmed to be c_{EO} = 10.77 Å, a_{EO} = b_{EO} = 11.46 Å by RSM carried out near STO 1 0 3 peak, as shown in Figure 5.18 (b) and (c).

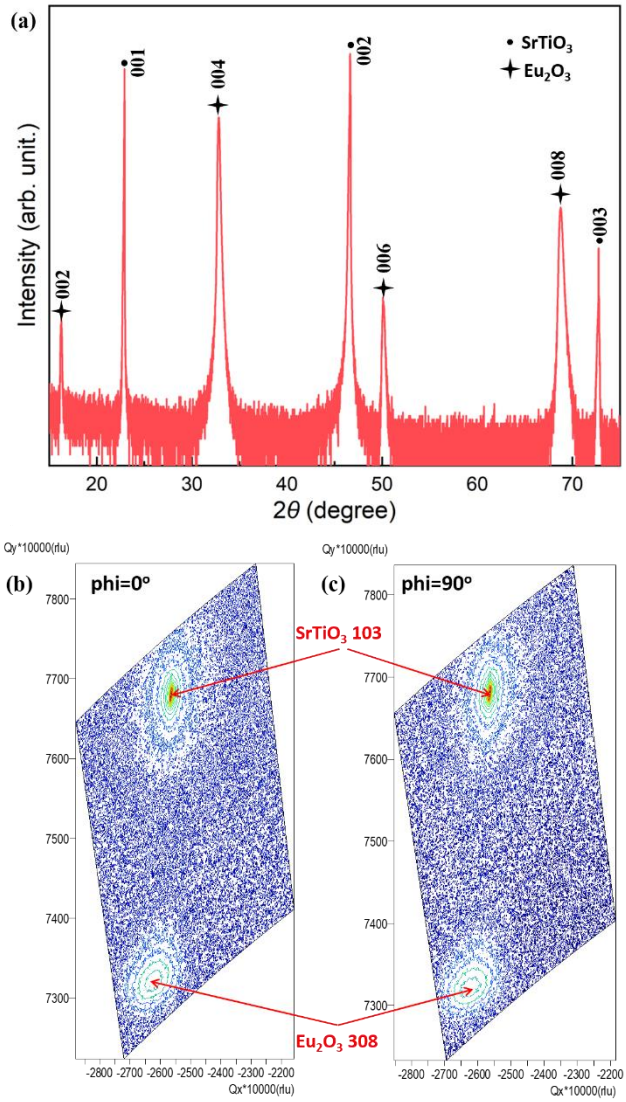

Figure 5.18 (a) XRD 2θ-ω scan of pure Eu_2O_3 on (0 0 1)-oriented STO; (b, c) Reciprocal space maps of Eu_2O_3 thin film around STO 1 0 3 peaks.

The field dependence of magnetization for Eu_2O_3 thin film and STO substrate at different temperatures from 2 to 54 K were measured, as shown in Figure 5.19. The commercial 5·5·0.5 mm^3 STO substrate (from CrysTec®) was load into the measurement system with non-magnetic

tools, the PM signal shown in Figure 5.19 (b) could be contamination when the substrate was produced. There was similar report about commercial STO showing unexpected magnetic signals [154]. As shown in Figure 5.19, the shape of curves for Eu_2O_3 and STO showing no significant magnetic phase transition.

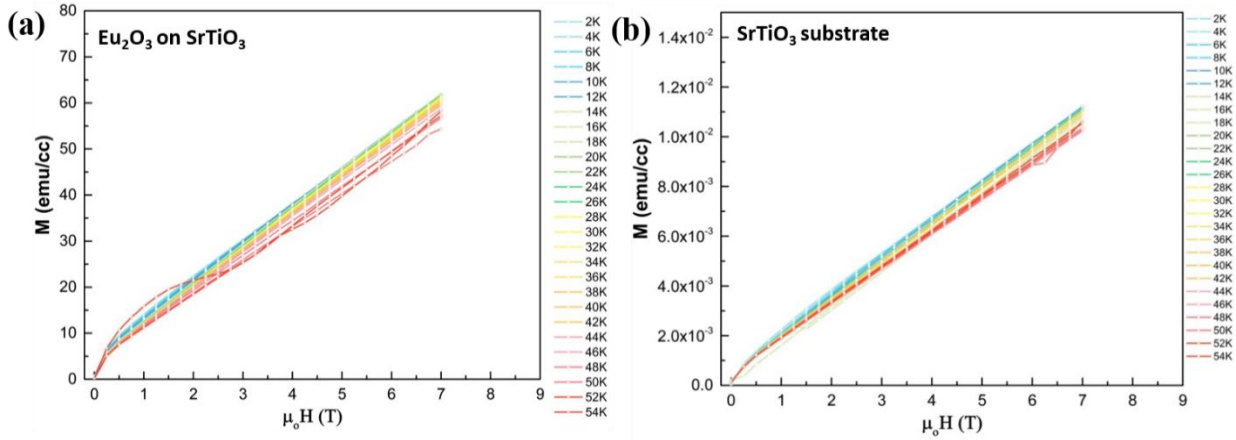

Figure 5.19 (a, b) Field dependence of magnetization for Eu_2O_3 on STO thin film, bare STO substrate at different temperatures from 2 to 54 K.

From the measured magnetization isotherms at different temperature as shown in Figure 5.17, the isothermal entropy change is calculated by the numerical approach of Maxwell relation mentioned in Section 2.4, Equation 3. In the equation, entropy change (ΔS) comprises structural, electronic and magnetic properties. Since in our $(EuTiO_3)_{1-x}$-$(Eu_2O_3)_x$ samples, both ETO and EO are insulators and show no structure transition under the measured temperature range [155–158], the entropy change (ΔS) represents the magnetic entropy change alone in our samples.

We plot the temperature dependence of $-\Delta S$ under different applied external magnetic fields (from 0.25 to 7 T with 0.25 T interval) for x = 0.2 and x = 0.5 as shown in Figure 5.20. For a given field change, $-\Delta S$ decreases on the both sides of T_c (Table 5.3). ΔS is negative over the whole range of temperature, the peak value of $-\Delta S$ increases monotonically with increasing external magnetic field. For x = 0.5, the maximum magnetic entropy change $-\Delta S_m$ is 9.4, 15.2, 25.1 and 28.7 J/kg·K for magnetic field change ΔH of 1, 2, 5, 7 T. For x = 0.2, the maximum magnetic entropy change $-\Delta S_{max}$ is 19.8, 31.4, 49.4 and 56.5 J/kg·K for magnetic field change ΔH of 1, 2, 5, 7 T. Compare to the $-\Delta S_{max}$ of x = 0.2, the relatively smaller value of $-\Delta S_{max}$ in x = 0.5 is due to the smaller size

of effective ETO. The lateral width of the ETO between the embedded EO nanofeatures for the x= 0.2 and 0.5 in the TEM images in Figures 5.5 (a) and 5.5 (d, e) in Section 5.3, the values are up to ~ 50 nm, and ~5 -10 nm, respectively. Similar effects have been reported in $Eu_{0.9}Sr_{0.1}TiO_3$ [24] and manganites [159]. In Table 5.20, we compare the maximum magnetic entropy change ($-\Delta S_{max}$) calculated in x = 0.5 and x = 0.2 VAN thin films with those of ETO-based bulk materials. The magnetic entropy change in x = 0.2 is higher than literature reported single crystal bulk ETO [20] or polycrystal bulk ETO [21]. The enhanced magnetocaloric effect was also observed in ETO nanowires [160].

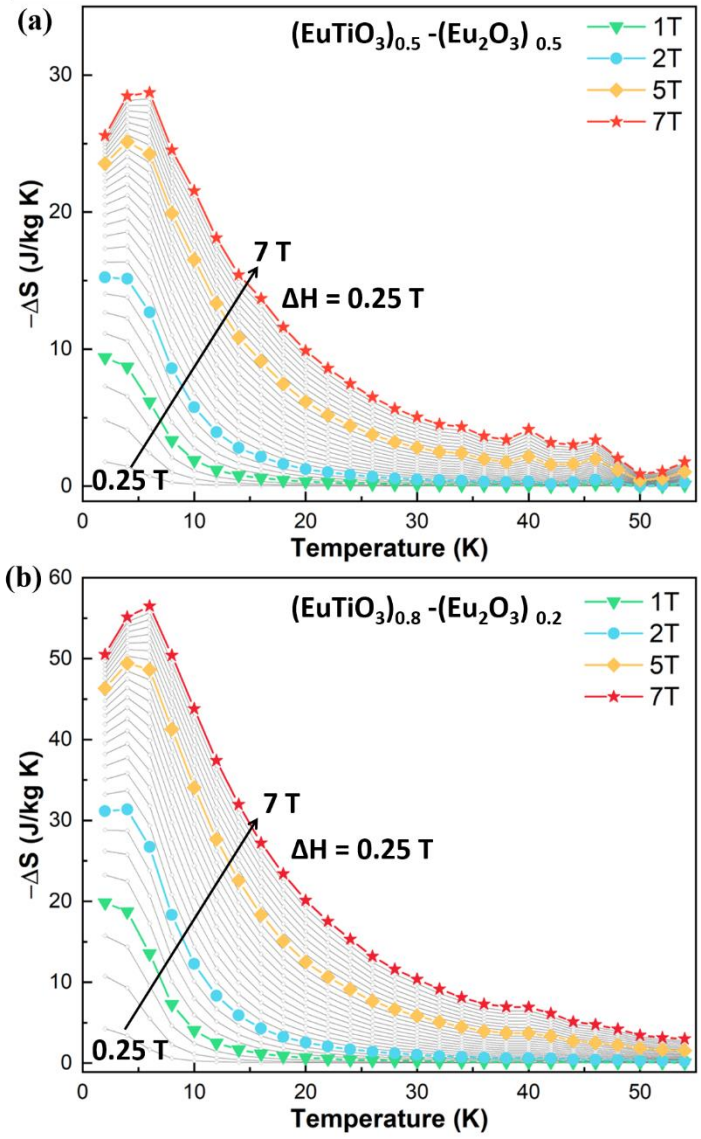

Figure 5.20 (a, b) Temperature dependence of the magnetic entropy change ($-\Delta S$) under different applied external magnetic fields for x = 0.5 and 0.2, respectively.

Table 5.4 Maximum values of magnetic entropy change ($-\Delta S_m$) and magnetic transition temperature for ETO-based compounds (SC: single crystalline, PL: polycrystalline).

Compound	T_N/T_c **(K)**	$-\Delta S_m$ **(J/kg·K)**		**Reference**
		ΔH = 2 T	ΔH = 5 T	
$(ETO)_{0.8}$-$(Eu_2O_3)_{0.2}$ thin film	3.00	31.4	49.4	this work
$(ETO)_{0.5}$-$(Eu_2O_3)_{0.5}$ thin film	3.12	15.2	25.1	
$EuTiO_3$ (PL)	5.7	22.3	40.4	[20]
$EuTiO_3$ (PL)	5.4	20	40.4	[21]
$EuTiO_3$ (SC)	5.6	22.3	44.4	
$Eu_{0.8}Ba_{0.2}TiO_3$ (PL)	2.8	20	35	[22]
$Eu_{0.99}La_{0.01}TiO_3$ (PL)	5.2	23	41.5	[23]
$Eu_{0.8}La_{0.2}TiO_3$ (PL)	7.5	18	31.4	
$Eu_{0.96}Sr_{0.04}TiO_3$ (PL)	-	20.8	38.4	[24]
$Eu_{0.98}Sr_{0.02}TiO_3$ (PL)	-	20.7	38.2	
$Eu_{0.9}Sr_{0.1}TiO_3$ (PL)	5.7	21	37.8	
$EuTi_{0.9}Cr_{0.1}O_3$ (PL)	9.7	16.8	30	[25]
$EuTi_{0.85}Nb_{0.15}O_3$ (SC)	9.5	21	36.3	[26]
$EuTi_{0.95}Fe_{0.05}O_3$ (SC)	6	18.5	31.5	[27]
$EuTi_{0.9}Fe_{0.1}O_3$ (SC)	6	18	31	
$EuTi_{0.9}V_{0.1}O_3$ (PL)	4.54	20	36	[28]

5.9 Summary

Self-assembled, epitaxial VAN films of ETO-EO grown on STO, with a range of EO fractions, were made, with the aim of tuning the magnetic ground states in ETO *via* progressive increasing of the vertical out-of-plane strain (while maintaining a constant in-plane strain). The VAN films were all found to be ferromagnetic. Increasing tetragonality was shown to cause an increase in M (measured at 2K, 500 Oe) to a maximum of 5.15 μ_B/Eu for x = 0.2 fraction, followed by a decrease. At the same time H_c increased across the series. The results can be explained by a progressive reduction in the Eu-Ti-Eu bond angle along {111} in the unit cell, as determined from measuring the atomic position in electronic microscopy image. This strongly influences the AF interactions along {111} direction. Consequently, modifies the competition between AF and FM interactions. Hence, for the largest volume fraction (x=0.5) of EO (larger tetragonality), the film shows strong ferromagnetic behavior because of weakened AF interactions. DFT calculations were undertaken, a threshold vertical strain of 2.5% at which ETO switch from AF to FM is proposed. This supports our magnetic properties of VAN films (different vertical strain). Our results provide a new way to delicately control and tune the antiferromagnetic and ferromagnetic correlations in strongly correlated oxide, and it reveals that 3D strain, induced uniquely using VAN structures, can manipulate multifunctionalities of strong spin-lattice coupling perovskite oxides at the atomic scale. Magnetic entropy changes characterizations on $(EuTiO_3)_{1-x}$-$(Eu_2O_3)_x$ (x= 0.2, 0.5) thin films were carried out. Giant magnetic entropy change ($-\Delta S_m$ = 31.4 J/kg·K at ΔH = 2T) was observed in $(ETO)_{0.8}$-$(Eu_2O_3)_{0.2}$ VAN thin film, which is higher than the literature reported single crystal bulk ETO [20] ($-\Delta S_m$ = 23 J/kg·K at ΔH = 2T) or polycrystal bulk ETO [21] ($-\Delta S_m$ = 22.3 J/kg·K at ΔH = 2T).

Chapter 6. Magnetic properties of $Eu_{1-x}Gd_xTiO_3$ (x=0.3, 0.5, 1) thin films – Results and Discussion

As mentioned in Section 2.2, to realize electric field-controlled magnetism in ETO, the modification of magnetic behavior, especially realizing the FM state in ETO, is crucial. Previous chapter has focused on using the vertical strain induced by VAN structure to tune the Eu-Ti-Eu bond angle along {111} in the unit cell, thus affecting the balance between AF and FM interations whithin ETO and cause the AF to FM magnetic ground state transition. This kind of mechanism has been widely used in realizing FM in ETO, such as introducing biaxial tensile strain [16,82], volume expansion [83], and electric fields [80].

Another mechanism is based on Ruderman-Kittel-Kasuya-Yosida (RKKY) interaction [161] between localized moments of nearest-neighbor Eu^{2+} spins mediated by the conduction electrons. Under this mechanism are the cases of chemical doping induced FM in the ETO-based compounds, such as $Eu_{1-x}A_xTiO_3$ (A=La, Gd, Dy) [161,162], $EuTi_{1-x}B_xO_3$ (B=Cr, Nb, Zr) [163–165], $EuTiO_{3-x}H_x$ [166] and $EuTiO_{3-x}$ [167]. Among these compounds, Gd-doped ETO is interesting. The most stable valence state of Ti in the $GdTiO_3$ (GTO) is 3+, which means Ti is in a spin ½ $3d^1$ electronic state, while the valence state of Ti in ETO is 4+, which means Ti is in a spin ½ $3d^0$ electronic state. Gd^{3+} and Eu^{2+} both possesses $4f^7$ configurations. Doping of Gd into Eu-site with larger substitutions of x = 0.5 and x = 0.7 has been carried out in previous literature [161], FM behavior was reported in $Eu_{1-x}Gd_xTiO_3$ (x=0.5, 0.7) samples.

In this chapter, we fabricate $Eu_{1-x}Gd_xTiO_3$ (x=0.3, 0.5, 1) thin films and study their magnetic properties, strain states and valence states differences of $Eu_{1-x}Gd_xTiO_3$ (x=0.3, 0.5) are investigated by XRD and XPS, the origin of FM in $Eu_{1-x}Gd_xTiO_3$ thin films are discussed.

6.1 Fabrication of $Eu_{1-x}Gd_xTiO_3$ (x=0.3, 0.5, 1) thin films

Before growing $Eu_{1-x}Gd_xTiO_3$ (x=0.3, 0.5) thin films, we start with optimizing the growth conditions of GTO thin films in our PLD system. Growing stoichiometric GTO thin film is particularly challenging due to the poor stability of Ti^{3+} ions in GTO. An oxygen-rich atmosphere usually introduces impurity $Gd_2Ti_2O_7$ pyrochlore phases into this compound. So far, growing the

pure GTO thin film using PLD technique in the literature report is scarce. To best of our knowledge, there is only one report showing successfully growing stoichiometric GTO thin film using the PLD technique [168].

First group of thin films were grown under ~ $4 \cdot 10^{-4}$ Torr O_2 with various substrate temperatures as shown in Table 6.1. A laser fluence of 2 J/cm^2 with a repetition rate of 3 Hz was used to ablate the ceramic target (mixture of Gd_2O_3 and TiO_2 weighted as per required proportion). Thin films were deposited on (0 0 1)-oriented LSAT substrates with an IP lattice parameter of 3.868 Å. XRD 2θ-ω scans were carried out on these samples as shown in Figure 6.1, however, there show no thin film peaks except signals from the substrates.

Table 6.1 $GdTiO_3$ thin films grown under ~ $4 \cdot 10^{-4}$ Torr O_2 with various substrate temperatures.

Sample Number	**Substrate**	**Temperature (°C)**	**Growth Pressure (Torr)**	**In-situ post-annealing**
1	(0 0 1)-oriented LSAT	650	~ $4 \cdot 10^{-4}$ in O_2	No
2		675		
3		700		
4		725		
5		750		

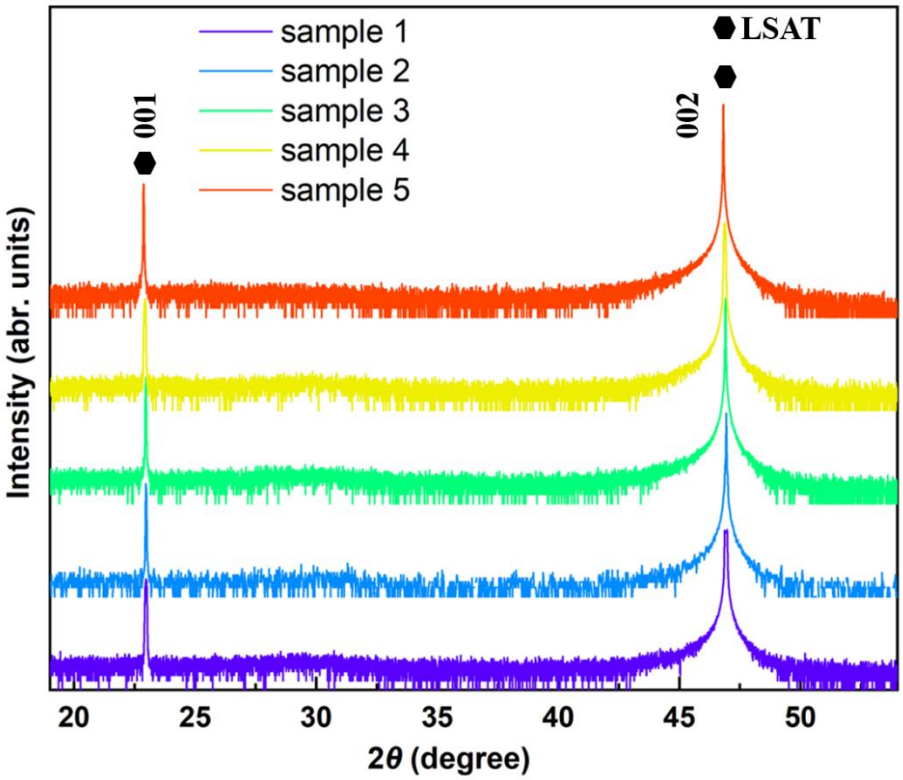

Figure 6.1 XRD 2θ-ω scans of $GdTiO_3$ thin films grown under ~ $4 \cdot 10^{-4}$ Torr O_2 with various substrate temperatures.

Next, we tried to grow the samples under vacuum ($1 \cdot 10^{-6}$ Torr) with various substrate temperatures as shown in Table 6.2. The laser fluence, laser repetition rate and substrate type were unchanged.

Table 6.2 $GdTiO_3$ thin films grown under $1 \cdot 10^{-6}$ Torr in vacuum with various substrate temperatures.

Sample Number	Substrate	Temperature (°C)	Growth Pressure (Torr)	In-situ post-annealing
6	(0 0 1)-oriented LSAT	700	$1 \cdot 10^{-6}$ in vacuum	No
7		750		
8		800		
9		850		

XRD 2θ-ω scans were carried out on these samples as shown in Figure 6.2. When the substrate temperature was set to 700 ^{o}C (sample), no crystalline thin film peak (except substrate) could be observed. Under the substrate temperature of 750 ^{o}C (sample 7), 1 1 0 and 2 2 0 GTO peaks could be clearly shown lying near the 0 0 *l* LSAT substrate. When the substrate increased to above 800 ^{o}C (sample 8 and 9), 1 1 1 GTO phase and impurity phases started to show in the OOP direction.

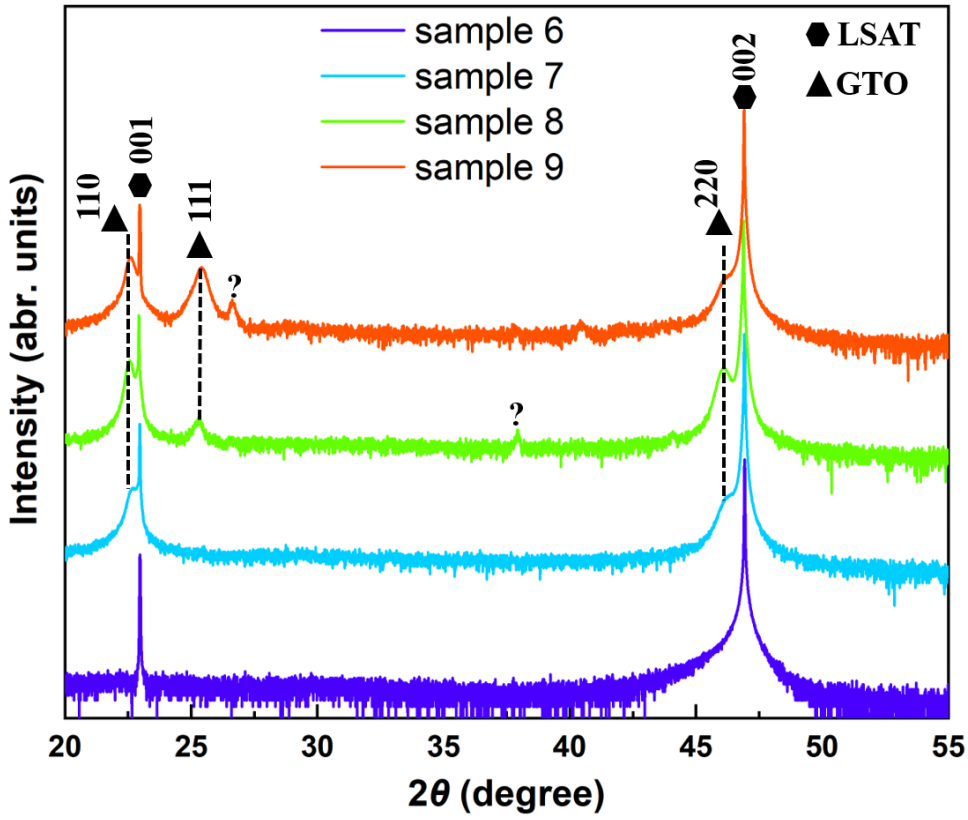

Figure 6.2 XRD 2θ-ω scans of $GdTiO_3$ thin films grown under vacuum ($1\cdot 10^{-6}$ Torr) with various substrate temperatures.

The ceramic targets for making $Eu_{1-x}Gd_xTiO_3$ (x=0.3, 0.5) thin films were fabricated through conventional solid-state reaction. Pure powders of Eu_2O_3 (nanopowder, <150 nm particle size, 99.5% trace metal basis, Sigma-Aldrich), Gd_2O_3 (powder, 99.9% trace metal basis, Sigma-Aldrich) and TiO_2 (powder, 99.9% metal basis, Alfa Aesar) were used. The powders were weighed in the required proportions and ground for 30 minutes. The powder mixtures were then pressed into pellets (3 cm diameter) under hydraulic press with a pressure of 10 tons for 30 minutes. The pressed

pellets were then sintered in air atmosphere, heated from room temperature to 1400 ℃ with 5℃/min, kept at 1400℃ for 24 hours, followed by slow cooling (1 ℃/min) to room temperature. XRD 2θ-ω scans were carried out on the targets to check the phases, as shown in Figure 6.3. In the composite targets, $Eu_2Ti_2O_7$ [131], $Gd_2Ti_2O_7$ [169] and Gd_2O_3 [170] phases are identical. Since the powder mixtures were sintered in air atmosphere, $Gd_2Ti_2O_7$ are formed instead of $GdTiO_3$ [171]. Gd_2O_3 phases were detected (more obvious in x = 0.5 target) because of relatively low temperature and shorter sintering time compared to previous report [169].

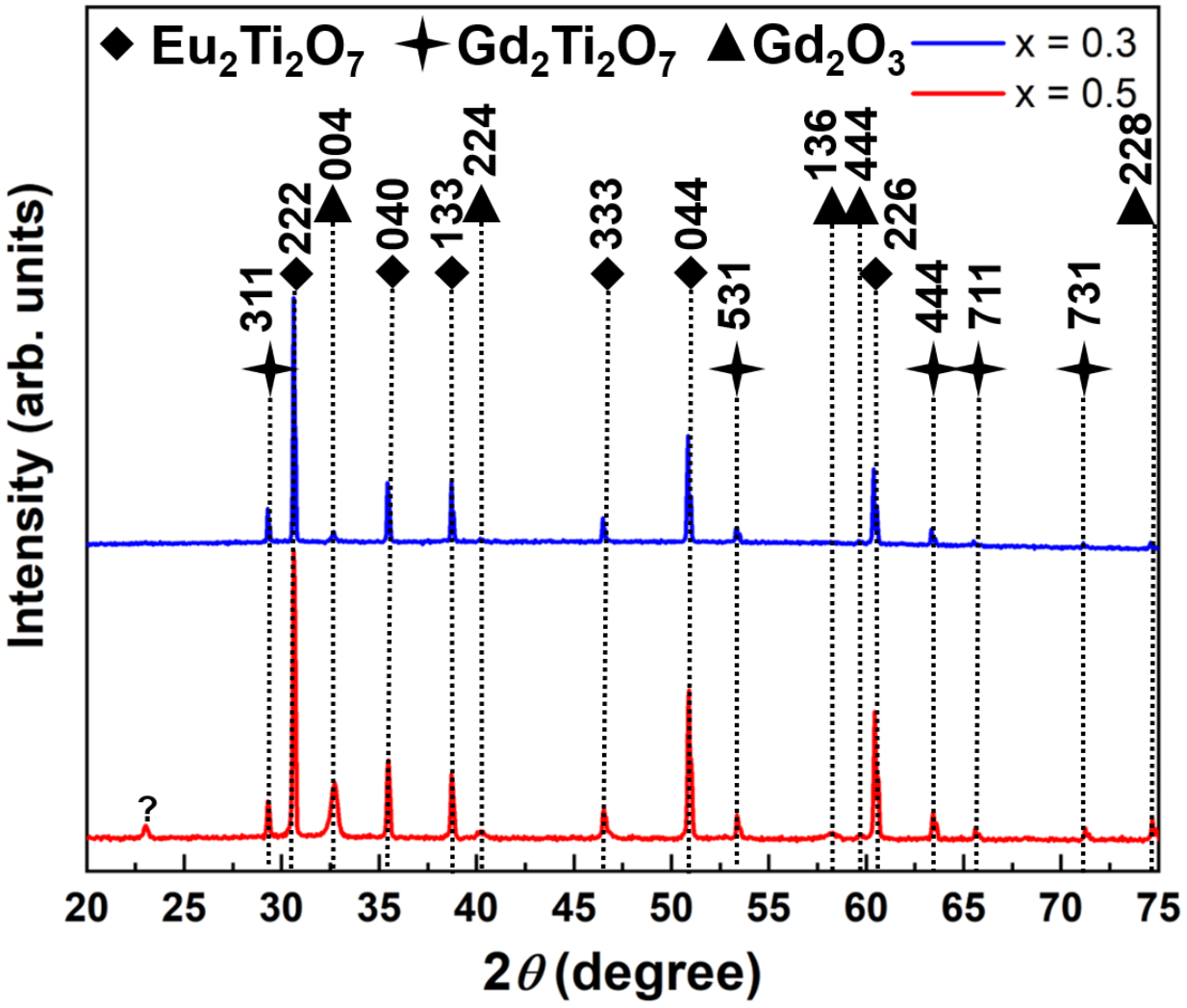

Figure 6.3 XRD 2θ-ω scans of ceramic targets prepared for $Eu_{1-x}Gd_xTiO_3$ (x=0.3, 0.5) thin films.

The ceramic targets containing $Eu_2Ti_2O_7$, $Gd_2Ti_2O_7$ and Gd_2O_3 phases were used for later PLD deposition, since it only required cation stoichiometry as mentioned before. Comparing the optimized growth conditions for GTO, it can be concluded that for growing stoichiometric GTO,

high vacuum during deposition (around 1-2 · 10^{-6} Torr) is required. The substrate temperature is around 750 ºC for GTO and around 710 ºC for ETO-based VAN thin films. Since our aim was to dope Gd into Eu-site with smaller substitutions of x = 0.3 and x = 0.5, the substrate temperature was set to that of ETO. The growth condition chosen for depositing $Eu_{1-x}Gd_xTiO_3$ (x = 0.3, 0.5) is shown in Table 6.3.

Table 6.3 Growth condition for $Eu_{1-x}Gd_xTiO_3$ (x = 0.3, 0.5) thin films.

$Eu_{1-x}Gd_xTiO_3$	**Thickness (nm)**	**Laser Repetition Rate (Hz)**	**Temperature (ºC)**	**Growth Pressure (Torr)**	**Substrate**
x=0.3	50	3	710	1-2·10^{-6}	(0 0 1)-oriented STO
x=0.5					

XRD 2θ-ω scans were carried out on $Eu_{1-x}Gd_xTiO_3$ (x = 0.3, 0.5) thin films as shown in Figure 6.3. In the whole range 2θ-ω scans (Figure 6.3 a), $Eu_{1-x}Gd_xTiO_3$ 0 0 l peaks can be observed in x = 0.3 sample. If we zoom in the range of 2θ (34º to 56º, Figure 6.3 (b)), we can see the fringes of $Eu_{1-x}Gd_xTiO_3$ 0 0 2 peak in x = 0.5 sample, while the main peak lying beneath the STO 0 0 2 peak. Since the ionic radii of Gd^{3+} is smaller than that of Eu^{2+}, the lattice parameter of $Eu_{1-x}Gd_xTiO_3$ for x = 0.5 is smaller than that of x = 0.3, thus showing increased 2θ. And the compounds are ETO-based, the peak positions are very close to that of pure ETO grown on (0 0 1)-oriented STO (as shown in Figure 4.2). No extra peaks, such as $Eu_2Ti_2O_7$, $Gd_2Ti_2O_7$ and Gd_2O_3 phases, are detected (compared Figure 6.4 with Figure 6.3). This once again confirmed that by careful controlling the growth parameter during PLD deposition process, $EuTiO_3$-based thin films can be obtained from $Eu_2Ti_2O_7$-based ceramic targets (cation stichometry were preserved).

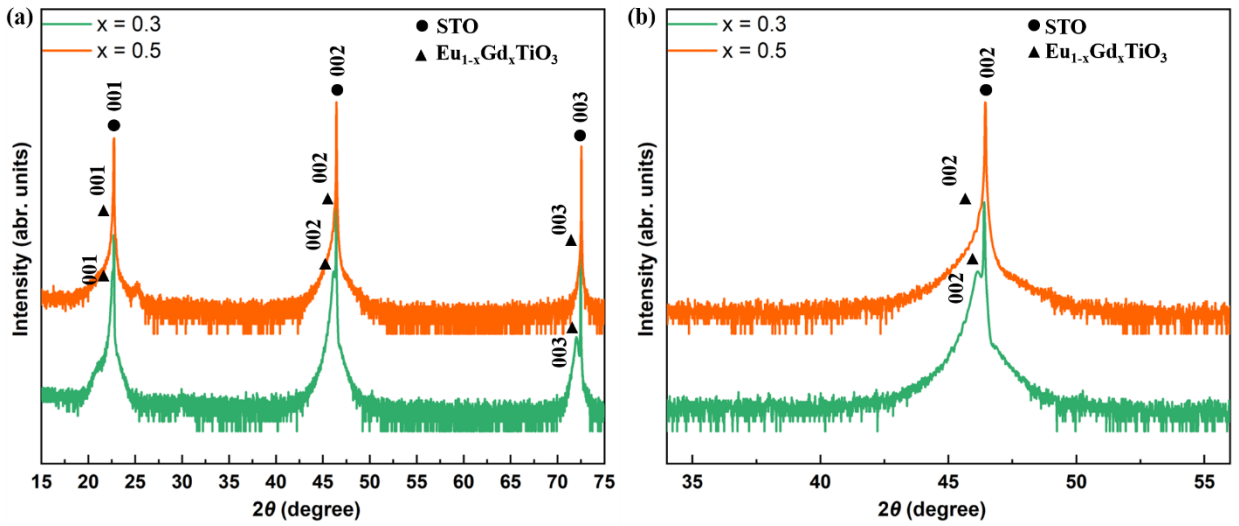

Figure 6.4 (a, b) XRD 2θ-ω scans of $Eu_{1-x}Gd_xTiO_3$ (x = 0.3, 0.5) thin films on (0 0 1)-oriented STO.

6.2 Magnetic properties characterization of $Eu_{1-x}Gd_xTiO_3$ (x = 0.3, 0.5, 1) thin films using SQUID

We first investigate the magnetic property of pure GTO grown in our PLD system, temperature-dependent magnetization was carried out on sample 7 using SQUID. Since there is magnetic contribution from both Gd^{3+} and Ti^{3+}, the magnetic moment was converted (μ_B/f.u.). M-T curves obtained by field-cooling under 100 Oe with temperature range of 5 K to 80 K are shown in Figure 6.4. FM behavior can be observed with a T_c around 30 K (for better comparison with literature report, the 1st derivate of *M*-*T* curves is not applied here), which is very close to the values reported in thick GTO films [71,168] and bulk GTO [62,64].

Temperature-dependent magnetization and magnetic field-dependent magnetization were then carried out on $Eu_{1-x}Gd_xTiO_3$ (x = 0.3, 0.5) thin films as shown in Figure 6.5. *M*-*T* curves were obtained by field-cooling under 100 Oe and magnetic hysteresis loops (magnetization vs. magnetic field, *M*-*H*) were measured along the a-b plane of thin films at 2 K. They all show clear FM behavior with the T_c determined from 1st derivation of *M*-*T* curves to be 6.7 K for x = 0.3 and 5.4 K for x = 0.5. The magnetic signals are contributed from the deposited thin films since STO substrates are non-magnetic. The values of magnetic moment (*M*) obtained at 2K and 500 Oe field are 2.8 μ_B/f.u. for x = 0.3 and 2.1 μ_B/f.u. for x = 0.5. The coercivity fields (H_c) determined from *M*-

H curves are 21 Oe for x = 0.3 and 35 Oe for x = 0.5. This result suggests that by doping small amount of Gd (x = 0.3, 0.5) into ETO, comparing to literature reported $Eu_{1-x}Gd_xTiO_3$ (x = 0.5, 0.7) [161], magnetic ground state of ETO could also be tuned from AF (ETO bulk) to FM.

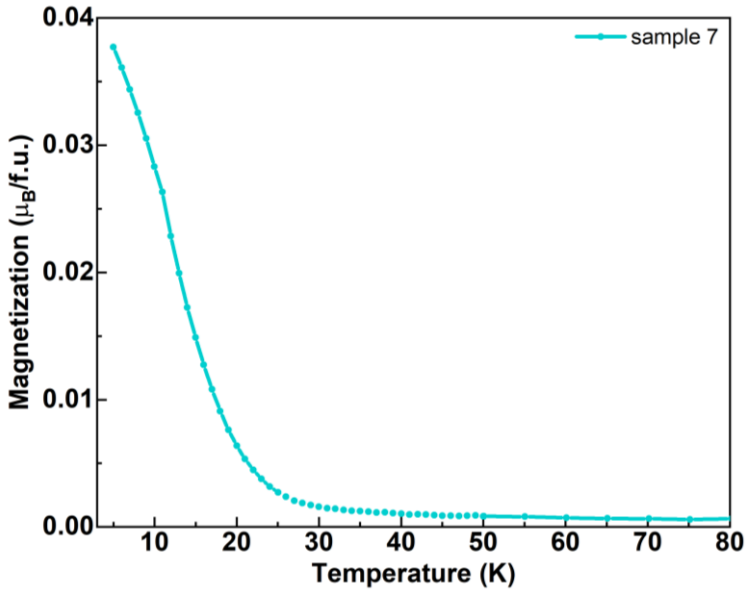

Figure 6.5 Temperature-dependent magnetization measure from 5 K to 80 K of pure GTO.

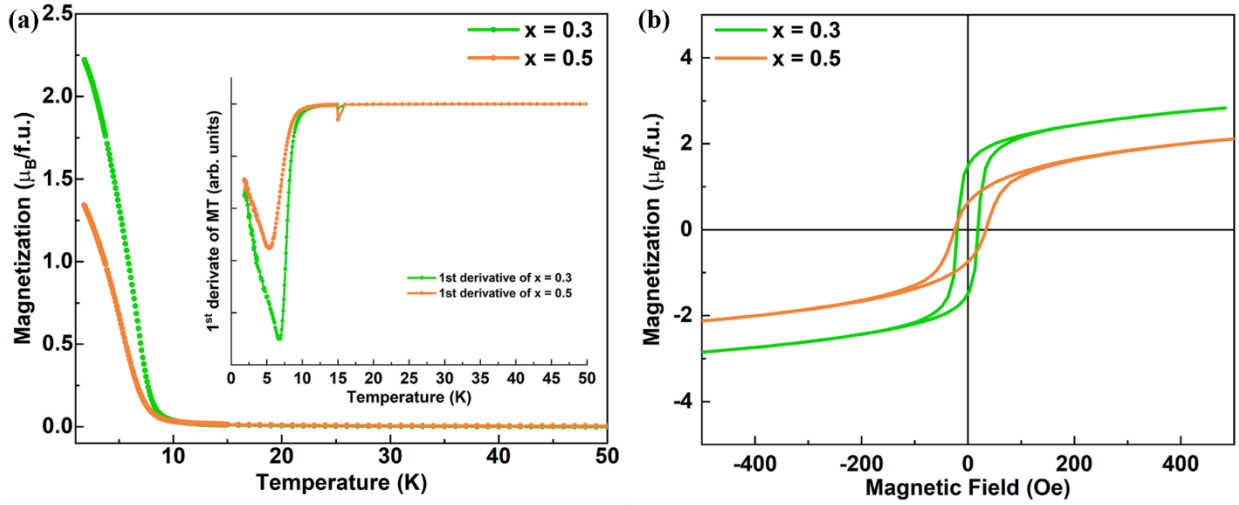

Figure 6.6 (a) Temperature-dependent magnetization measured from 1.8 K to 50 K of $Eu_{1-x}Gd_xTiO_3$ (x = 0.3, 0.5) thin films. The inset shows 1st derivation M-T of x = 0.3 and x = 0.5. (b) Magnetic hysteresis loops of $Eu_{1-x}Gd_xTiO_3$ (x = 0.3, 0.5) thin films measured at 2 K.

6.3 Strain state analysis of $Eu_{1-x}Gd_xTiO_3$ (x=0.3, 0.5) thin films using XRD

To exclude the possibility of strain-induced FM transition in $Eu_{1-x}Gd_xTiO_3$ (x = 0.3, 0.5) thin films, strain state analysis of $Eu_{1-x}Gd_xTiO_3$ (x = 0.3, 0.5) thin films was carried out. The OOP and IP lattice parameters were determined from RSM near the STO 1 0 3 peaks as shown in Figure 6.6. For both x = 0.3 and x = 0.5 films, the $Eu_{1-x}Gd_xTiO_3$ 1 0 3 peaks have the same Q_{in} values as the STO 1 0 3 peaks, indicating that the IP lattice parameters of $Eu_{1-x}Gd_xTiO_3$ are the same as that for the STO substrate ($a_{STO} = a_{EGTO} = b_{STO} = b_{EGTO}$ = 3.905 Å). The OOP lattice parameter for x = 0.3 is (calculated using the center of the red circle) 3.932 Å. For x = 0.5, the $Eu_{0.5}Gd_{0.5}TiO_3$ 1 0 3 peak share the same Q_{out} value as the STO 1 0 3 peak, this point can be confirmed from Figure 6.3 (b). Thus, the IP and OOP lattice parameters, tetragonal distortions and vertical strains for $Eu_{1-x}Gd_xTiO_3$ (x = 0.3, 0.5) thin films are summarized in Table 6.4. The error bars introduced were caused by peak broadening and the step size of individual 2θ-ω scans.

As discussed in the previous chapter (Section 5.4 and 5.6), if the FM behaviors in $Eu_{1-x}Gd_xTiO_3$ thin films are caused by strain effects, it requires the tetragonal distortions of $Eu_{1-x}Gd_xTiO_3$ satisfy the theoretical boundary of c/a = 1.02 (vertical strain case) or the vertical strain of $Eu_{1-x}Gd_xTiO_3$ satisfy the theoretical boundary of 2.5%. However, the tetragonal distortion and vertical strain in both samples are far away from these values. Thus, the FM behaviors in $Eu_{1-x}Gd_xTiO_3$ thin films are not caused by strain effects.

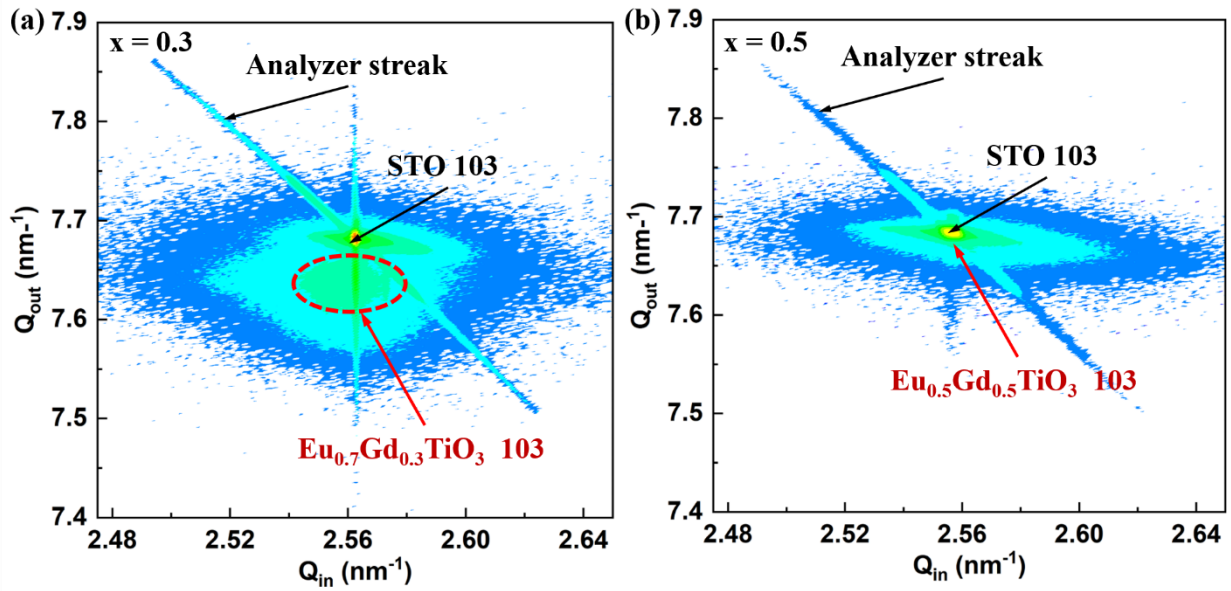

Figure 6.7 Reciprocal space maps of $Eu_{1-x}Gd_xTiO_3$ (x = 0.3, 0.5) thin films.

Table 6.4 The IP lattice parameters, OOP lattice parameters, tetragonal distortions and vertical strains of the $Eu_{1-x}Gd_xTiO_3$ in x = 0.3 and x = 0.5 films.

$Eu_{1-x}Gd_xTiO_3$	OOP Lattice Parameter *c* (Å)	IP Lattice Parameter *a* (Å)	Tetragonal Distortion *c*/*a*	Vertical Strain (%)
x = 0.3	3.932±0.015	3.905±0.015	1.007±0.015	0.68
x = 0.5	3.905±0.005	3.905±0.005	1.000±0.005	0.00

6.4 Valence state analysis of $Eu_{1-x}Gd_xTiO_3$ (x=0.3, 0.5) thin films using XPS

Because of the charge compensation, the existence of Gd^{3+} doping should induce changes in the valence states of cations. To quantify these changes, we carried out valence states analysis of $Eu_{1-x}Gd_xTiO_3$ (x = 0.3, 0.5) thin films by using XPS. We found that the valence states of Ti ions have been changed. The Ti 2*p* core-level photoemission spectrums of of $Eu_{1-x}Gd_xTiO_3$ (x = 0.3, 0.5) thin films are shown in Figure 6.7. When fitting the data, the intensity ratio (area ratio) of Ti $2p_{3/2}$ and Ti $2p_{1/2}$ peaks is constrained to 2:1 due to spin-orbit splitting. The initial peak positions are set around the reported position of Ti^{4+} $2p_{3/2}$, Ti^{4+} $2p_{1/2}$, Ti^{3+} $2p_{3/2}$ and Ti^{3+} $2p_{1/2}$. Compare with previous literature reported results, the peaks at a binding energy around 459.1 eV and 464.8 eV can be assigned as Ti^{4+}, with peaks around 458.7 eV and 464.4 eV corresponding to Ti^{3+} [149,172,173]. Comparing the peak areas, the content of Ti^{3+} was calculated to be 13.41% in the x = 0.3 thin film, while the content of Ti^{3+} in the x = 0.5 thin film was calculated to be 34.59%. The ideal content of Ti^{3+} for the x = 0.3 and x = 0.5 should be 30% and 50%, our fitting results are smaller than these values in both films. This suggests that the extra electrons introduced by Gd^{3+} doping are not all bonded to Ti^{4+} in the form of $Ti^{4+} + e^- \leftrightarrow Ti^{3+}$, in other words, 13.41% (x = 0.3) and 34.59% (x = 0.5) of extra electrons are bonded to Ti^{4+} effectively.

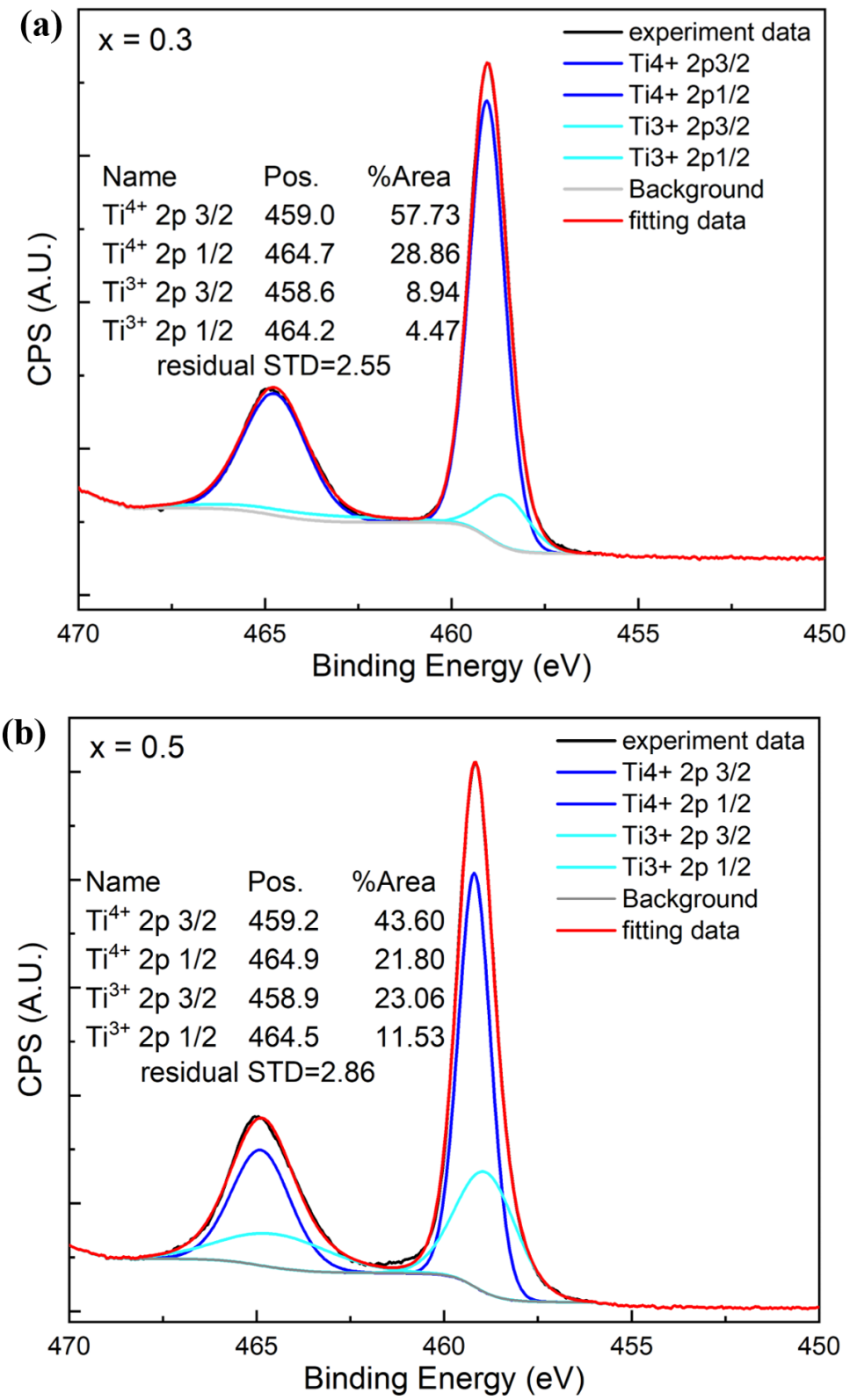

Figure 6.8 (a, b) Valence state analysis on Ti 2*p* core-level photoemission spectra of $Eu_{1-x}Gd_xTiO_3$ (x = 0.3, 0.5) thin films.

6.5 Origin of FM in $Eu_{1-x}Gd_xTiO_3$ (x = 0.3, 0.5) thin films

Gd-doping has caused the magnetic ground state of ETO to change from AF to FM. From the strain states analysis of both thin films, we can exclude the possibility of strain induced FM transition in ETO. From the XPS analysis of $Eu_{1-x}Gd_xTiO_3$ (x = 0.3, 0.5) thin films, we can see the by doping the Eu-site with Gd, extra electrons are introduced into the otherwise empty Ti 3d orbitals. 13.41% and 34.59% of extra electrons are bonded to Ti^{4+} effectively in x = 0.3 and x = 0.5 samples. The emergence of FM state in $Eu_{1-x}Gd_xTiO_3$ (x = 0.3, 0.5) thin films should be ascribed to magnetic interactions between localized Eu^{4+} 4f spins mediated by itinerant Ti 3d electrons (RKKY interaction). This kind of mechanism has also been reported in $Eu_{1-x}A_xTiO_3$ (A=La, Gd, Dy) [161,162], $EuTi_{1-x}B_xO_3$ (B=Cr, Nb, Zr) [163–165], $EuTiO_{3-x}H_x$ [166] and $EuTiO_{3-x}$ [167]. It should be pointed out here that the origin of ferromagnetic interaction in $GdTiO_3$ and $EuTiO_3$ are different [161], since the ferromagnetic interaction in $GdTiO_3$ is believed to be dominated between neighboring Ti (associated with the ordering of Ti t_{2g} orbitals) [174]. And clear magnetic behavior can be observed by comparing the temperature-dependent magnetization of $GdTiO_3$, ETO-EO VAN and Gd-doped $EuTiO_3$ (Figure 6.5, Figure 5.7 and Figure 6.6).

It should be noted that T_c drops from 6.7 K to 5.4 K as the x increases from 0.3 to 0.5, this can be explained by the RKKY oscillation [175,176]. In RKKY interactions, the sign of interaction changes oscillatory accordingly to the relation between the Fermi wave number and the distance between neighboring sites. Thus, with increasing number of electrons in Ti 3d orbitals, T_c can change oscillatory. The difference of the magnetic moment (2K, 500Oe) and coercivity field in x = 0.3 and x = 0.5 can be understood by chemical randomness induced by substitution of magnetic Eu^{2+} ions. Similar effects have been observed in $Eu_{1-x}A_xTiO_3$ (A=La, Gd) system [161].

6.6 Summary

In summary, two kinds of Gd-doped ETO thin films with different content of Gd (x = 0.3 and 0.5) and a reference sample (pure GTO thin film) were fabricated using PLD. Magnetic properties of these thin films were characterized using SQUID. We found that the Gd-doped ETO thin films has been changed from AF to FM (comparing to bulk ETO). By using XRD, we analyzed the strain states of $Eu_{1-x}Gd_xTiO_3$ (x = 0.3, 0.5) thin films and exclude the possibility of strain induced FM.

By using XPS, we demonstrated the valence states change of Ti ions. FM in $Eu_{1-x}Gd_xTiO_3$ (x = 0.3, 0.5) thin films was explained by magnetic interactions between localized Eu^{4+} 4f spins mediated by itinerant Ti 3d electrons (introduced by Gd doping). The results are important since it is the first time that valence states change of Ti ions is observed in (A=La, Gd, Dy) [161,162], $EuTi_{1-x}B_xO_3$ (B=Cr, Nb, Zr) [163–165] and $EuTiO_{3-x}H_x$ [166] systems, which can prove that the emergence of FM in $Eu_{1-x}Gd_xTiO_3$ is indeed originated from magnetic interactions between localized Eu^{4+} 4f spins mediated by itinerant Ti 3d electrons. This chapter also presents an alternative methodology to tune the magnetic ground states (from AF to FM) of ETO besides the strain induced FM method.

Chapter 7. Conclusions and Future Work

7.1 Conclusions

Systematic studies for optimizing the growth condition for ETO-based VAN thin films were carried out. Inverstigations for finding a suitable binary oxide second phase to incoporate with ETO were carried out. Careful consideration needs to be given when selecting a proper binary oxide second phase in cooperation with $EuTiO_3$ to form VAN structure, since the optimized growth condition suitable for ETO would not be always compatible with that of binary oxide second phases. After various exploration, $(ETO)_{0.5}$-$(Eu_2O_3)_{0.5}$ was successfully fabricated on (0 0 1)-oriented STO with preferred OOP orientation under careful control of growth pressure, substrate temperature and laser repetition rate. The optimized growth condition (laser repletion rate of 3 Hz, substrate temperature of 710 ^oC and growth pressure of $1\text{-}2\cdot10^{-6}$ Torr) was confirmed to make the $(ETO)_{1-x}$-$(Eu_2O_3)_x$ (x = 0.2, 0.25, 0.33, 0.5) epitaxial thin film on STO substrate with preferred OOP orientation, aiming to tune the magnetic ground states in ETO *via* progressive increasing of the vertical out-of-plane strain (while maintaining a constant in-plane strain). The VAN films were all found to be ferromagnetic. Increasing tetragonality was shown to cause an increase in magnetization M (measured at 2K, 500 Oe) to a maximum of 5.15 μ_B/Eu for x = 0.2 fraction, followed by a decrease. At the same time H_c increased across the series. The results can be explained by a progressive reduction in the Eu-Ti-Eu bond angle along {111} in the unit cell, as determined from measuring the atomic position in electronic microscopy image. This strongly influences the AF interactions along {111} direction. Consequently, modifies the competition between AF and FM interactions. Hence, for the largest volume fraction (x=0.5) of EO (larger tetragonality), the film shows strong ferromagnetic behavior because of weakened AF interactions. DFT calculations were undertaken, a threshold vertical strain of 2.5% at which ETO switch from AF to FM is proposed via investigation of site PDOS of ETO under vertical strain states (while keeping the in-plane lattice parameter fixed to that of STO or bulk ETO). This supports our magnetic properties of VAN films (different vertical strain). These results provide a new way to delicately control and tune the antiferromagnetic and ferromagnetic correlations in strongly correlated oxide, and it reveals that 3D strain, induced uniquely using VAN structures, can manipulate multifunctionalities of strong spin-lattice coupling perovskite oxides at the atomic scale. Moreover, giant magnetic entropy change ($-\Delta S_m$ = 31.4 J/kg·K at ΔH = 2T) was observed in

$(ETO)_{0.8}$-$(Eu_2O_3)_{0.2}$ VAN thin film, single crystal bulk ETO [20] ($-\Delta S_m$ = 23 J/kg·K at ΔH = 2T) or polycrystal bulk ETO [21] ($-\Delta S_m$ = 22.3 J/kg·K at ΔH = 2T). Gd-doped ETO thin films were made and found to be ferromagnetic. The valence states change of Ti ions were demonstrated using XPS. FM in $Eu_{1-x}Gd_xTiO_3$ (x = 0.3, 0.5) thin films was explained by magnetic interactions between localized Eu^{4+} 4f spins mediated by itinerant Ti 3d electrons (introduced by Gd doping). This result is important since it is the first time that valence states change of Ti ions is observed in (A=La, Gd, Dy), $EuTi_{1-x}B_xO_3$ (B=Cr, Nb, Zr) and $EuTiO_{3-x}H_x$ systems, which can prove that the emergence of FM in $Eu_{1-x}Gd_xTiO_3$ is indeed originated from magnetic interactions between localized Eu^{4+} 4f spins mediated by itinerant Ti 3d electrons, which is different from the origin of ferromagnetic interaction in $GdTiO_3$ (dominated between neighboring Ti via the ordering of Ti t_{2g} orbitals [174]). This result also presents an alternative methodology to tune the magnetic ground states (from AF to FM) of ETO besides the strain induced (or electric field induced) FM method.

7.2 Future work

Due to the complexity and diverse structural tunability of rare earth titanates, there are still a huge number of interesting topics worthy of study in the future. Here I will list some of the opportunities that emerged during my initial exploration:

Firstly, concerning ETO-EO grown on STO, only magnetic moments and coercivity fields were tuned as varying the strain states, transition temperature T_c remained unchanged. It would be worthy exploring the origin of constant T_c in the system from a fundamental perspective. Also, since FM ETOs are usually FE as well, and our thin films (x = 0.2 and x = 0.5) show Ti up-shifted nature (from atomic position recognition), it would be interesting to characterize the FE properties in this series sample.

Secondly, besides vertical strain effects, enhanced giant magnetic entropy change in $(ETO)_{0.8}$-$(Eu_2O_3)_{0.2}$ VAN thin film may be also caused by interface effects (arises from the ETO and EO interfaces), similar to the reported Mn_3O_4-$La_{0.7}Sr_{0.3}MnO_3$ system, electronic structures study of Eu^{2+} and Eu^{3+} using X-ray magnetic circular dichroism and X-ray absorption spectroscopy would give an insight into the enhanced giant magnetocaloric effect.

Lastly, transport properties characterization could be carried out on Gd-doped ETO thin films, since there are itinerant electrons on Ti 3d orbital, these films are expected to be FM metal. Also, the T_c of these two samples are different as varying the Gd doping ratio, it would be interesting to introduce Gd into the ETO-EO VAN thin film and study their magnetic properties. It should be noted that it will be challenging to get a multiferroic chemical doped ETO-based VAN system with tunable properties, since subtle balance between the interactions inside ETO and relatively strict growth condition.

References

(1) Cava, R. J.; Batlogg, B.; Van Dover, R. B.; Murphy, D. W.; Sunshine, S.; Siegrist, T.; Remeika, J. P.; Rietman, E. A.; Zahurak, S.; Espinosa, G. P. Bulk Superconductivity at 91 K in Single-Phase Oxygen-Deficient Perovskite Ba2YCu3O9-δ. *Phys. Rev. Lett.* **1987**, *58* (16), 1676–1679. https://doi.org/10.1103/PhysRevLett.58.1676.

(2) Wang, J.; Neaton, J. B.; Zheng, H.; Nagarajan, V.; Ogale, S. B.; Liu, B.; Viehland, D.; Vaithyanathan, V.; Schlom, D. G.; Waghmare, U. V.; et al. Epitaxial BiFeO3 Multiferroic Thin Film Heterostructures. *Science (80-.).* **2003**, *299* (5613), 1719–1722. https://doi.org/10.1126/science.1080615.

(3) Jin, S.; Tiefel, T. H.; McCormack, M.; Fastnacht, R. A.; Ramesh, R.; Chen, L. H. Thousandfold Change in Resistivity in Magnetoresistive La-Ca-Mn-O Films. *Science (80-.).* **1994**, *264* (5157), 413–415. https://doi.org/10.1126/science.264.5157.413.

(4) Xing, G.; Mathews, N.; Sun, S.; Lim, S. S.; Lam, Y. M.; Graẗzel, M.; Mhaisalkar, S.; Sum, T. C. Long-Range Balanced Electron-and Hole-Transport Lengths in Organic-Inorganic CH3NH3PbI3. *Science (80-.).* **2013**, *342* (6156), 344–347. https://doi.org/10.1126/science.1243167.

(5) Ishihara, T.; Matsuda, H.; Takita, Y. Doped LaGaO3 Perovskite Type Oxide as a New Oxide Ionic Conductor. *J. Am. Chem. Soc.* **1994**, *116* (9), 3801–3803. https://doi.org/10.1021/ja00088a016.

(6) Radaelli, P.; Iannone, G.; Marezio, M. Structural Effects on the Magnetic and Transport Properties of Perovskite A(1-x)A(x)'MnO3 (X=0.25, 0.30). *Phys. Rev. B - Condens. Matter Mater. Phys.* **1997**, *56* (13), 8265–8276. https://doi.org/10.1103/PhysRevB.56.8265.

(7) Uehara, M.; Mori, S.; Chen, C. H.; Cheong, S. W. Percolative Phase Separation Underlies Colossal Magnetoresistance in Mixed-Valent Manganites. *Nature* **1999**, *399* (6736), 560–563. https://doi.org/10.1038/21142.

(8) Haeni, J. H.; Irvin, P.; Chang, W.; Uecker, R.; Reiche, P.; Li, Y. L.; Choudhury, S.; Tian, W.; Hawley, M. E.; Craigo, B.; et al. Room-Temperature Ferroelectricity in Strained SrTiO3. *Nature* **2004**, *430* (7001), 758–761. https://doi.org/10.1038/nature02773.

(9) Choi, K. J.; Biegalski, M.; Li, Y. L.; Sharan, A.; Schubert, J.; Uecker, R.; Reiche, P.; Chen, Y. B.; Pan, X. Q.; Gopalan, V.; et al. Enhancement of Ferroelectricity in Strained BaTiO3 Thin Films. *Science (80-.).* **2004**, *306* (5698), 1005–1009. https://doi.org/10.1126/science.1103218.

(10) Chu, M. W.; Szafraniak, I.; Scholz, R.; Harnagea, C.; Hesse, D.; Alexe, M.; Gösele, U. Impact of Misfit Dislocation on the Polarization Instability of Epitaxial Nanostructured Ferroelectric Perovskites. *Nature Materials*. 2004, pp 87–90. https://doi.org/10.1038/nmat1057.

(11) Schlom, D. G.; Chen, L.-Q.; Eom, C.-B.; Rabe, K. M.; Streiffer, S. K.; Triscone, J.-M. Strain Tuning of Ferroelectric Thin Films. *Annu. Rev. Mater. Res.* **2007**, *37* (1), 589–626. https://doi.org/10.1146/annurev.matsci.37.061206.113016.

(12) Schlom, D. G.; Chen, L. Q.; Fennie, C. J.; Gopalan, V.; Muller, D. A.; Pan, X.; Ramesh, R.; Uecker, R. Elastic Strain Engineering of Ferroic Oxides. *MRS Bull.* **2014**, *39* (2), 118–130. https://doi.org/10.1557/mrs.2014.1.

(13) Yokoyama, Y.; Yamasaki, Y.; Taguchi, M.; Hirata, Y.; Takubo, K.; Miyawaki, J.; Harada, Y.; Asakura, D.; Fujioka, J.; Nakamura, M.; et al. Tensile-Strain-Dependent Spin States in Epitaxial LaCoO3 Thin Films. *Phys. Rev. Lett.* **2018**, *120* (20). https://doi.org/10.1103/PhysRevLett.120.206402.

(14) Katsufuji, T.; Takagi, H. Coupling between Magnetism and Dielectric Properties in Quantum Paraelectric EuTiO3. *Phys. Rev. B - Condens. Matter Mater. Phys.* **2001**, *64* (5). https://doi.org/10.1103/PhysRevB.64.054415.

(15) Fennie, C. J.; Rabe, K. M. Magnetic and Electric Phase Control in Epitaxial EuTiO3 from First Principles. *Phys. Rev. Lett.* **2006**, *97* (26), 267602. https://doi.org/10.1103/PhysRevLett.97.267602.

(16) Lee, J. H.; Fang, L.; Vlahos, E.; Ke, X.; Jung, Y. W.; Kourkoutis, L. F.; Kim, J. W.; Ryan, P. J.; Heeg, T.; Roeckerath, M.; et al. A Strong Ferroelectric Ferromagnet Created by Means of Spin-Lattice Coupling. *Nature* **2010**, *466* (7309), 954–958. https://doi.org/10.1038/nature09331.

(17) Fiebig, M. Revival of the Magnetoelectric Effect. *Journal of Physics D: Applied Physics*. 2005. https://doi.org/10.1088/0022-3727/38/8/R01.

(18) Bibes, M.; Barthélémy, A. Multiferroics: Towards a Magnetoelectric Memory. *Nature Materials*. 2008, pp 425–426. https://doi.org/10.1038/nmat2189.

(19) Ma, J.; Hu, J.; Li, Z.; Nan, C. W. Recent Progress in Multiferroic Magnetoelectric Composites: From Bulk to Thin Films. *Adv. Mater.* **2011**, *23* (9), 1062–1087. https://doi.org/10.1002/adma.201003636.

(20) Mo, Z. J.; Shen, J.; Li, L.; Liu, Y.; Tang, C. C.; Hu, F. X.; Sun, J. R.; Shen, B. G. Observation of Giant Magnetocaloric Effect in EuTiO3. *Mater. Lett.* **2015**, *158*, 282–284. https://doi.org/10.1016/j.matlet.2015.06.040.

(21) Midya, A.; Mandal, P.; Rubi, K.; Chen, R.; Wang, J. S.; Mahendiran, R.; Lorusso, G.; Evangelisti, M. Large Adiabatic Temperature and Magnetic Entropy Changes in EuTi O3. *Phys. Rev. B* **2016**, *93* (9). https://doi.org/10.1103/PhysRevB.93.094422.

(22) Rubi, K.; Kumar, P.; Maheswar Repaka, D. V.; Chen, R.; Wang, J. S.; Mahendiran, R. Giant Magnetocaloric Effect in Magnetoelectric Eu1-XBaxTiO3. *Appl. Phys. Lett.* **2014**, *104* (3). https://doi.org/10.1063/1.4862981.

(23) Rubi, K.; Midya, A.; Mahendiran, R.; Maheswar Repaka, D. V.; Ramanujan, R. V. Magnetocaloric Properties of Eu1-XLaxTiO3 ($0.01 \leq x \leq 0.2$) for Cryogenic Magnetic Cooling. *J. Appl. Phys.* **2016**, *119* (24). https://doi.org/10.1063/1.4954020.

(24) Mo, Z. J.; Sun, Q. L.; Wang, C. H.; Wu, H. Z.; Li, L.; Meng, F. Bin; Tang, C. C.; Zhao, Y.; Shen, J. Effects of Sr-Doping on the Giant Magnetocaloric Effect of EuTiO3. *Ceram. Int.* **2017**, *43* (2), 2083–2088. https://doi.org/10.1016/j.ceramint.2016.10.184.

(25) Mo, Z. J.; Hao, Z. H.; Shen, J.; Li, L.; Wu, J. F.; Hu, F. X.; Sun, J. R.; Shen, B. G. Observation of Giant Magnetocaloric Effect in EuTi1-XCrxO3. *J. Alloys Compd.* **2015**, *649*, 674–678. https://doi.org/10.1016/j.jallcom.2015.07.176.

(26) Roy, S.; Khan, N.; Mandal, P. Giant Low-Field Magnetocaloric Effect in Single-Crystalline EuTi0.85Nb0.15O3. *APL Mater.* **2016**, *4* (2). https://doi.org/10.1063/1.4940960.

(27) Zhang, W.; Mo, Z.-J.; Hao, Z.; Shen, J.; Luo, J.-W.; Chang, R.-J.; Li, L. Fe Doping Effect on EuTiO3: The Magnetic Properties and Giant Magnetocaloric Effect. *Int. J. Appl. Ceram. Technol.* **2019**, *00* (16). https://doi.org/10.1111/ijac.13180.

(28) Roy, S.; Das, M.; Mandal, P. Large Low-Field Magnetic Refrigeration in Ferromagnetic Insulator EuTi0.9V0.1O3. *Phys. Rev. Mater.* **2018**, *2* (6), 64412. https://doi.org/10.1103/PhysRevMaterials.2.064412.

(29) Tomioka, Y.; Tokura, Y. Global Phase Diagram of Perovskite Manganites in the Plane of Quenched Disorder versus One-Electron Bandwidth. *Phys. Rev. B - Condens. Matter Mater. Phys.* **2004**, *70* (1). https://doi.org/10.1103/PhysRevB.70.014432.

(30) Hemberger, J.; Krimmel, A.; Kurz, T.; Krug von Nidda, H. A.; Ivanov, V. Y.; Mukhin, A. A.; Balbashov, A. M.; Loidl, A. Structural, Magnetic, and Electrical Properties of Single-Crystalline La1-XSrxMnO3 (0.4<x<0.85). *Phys. Rev. B - Condens. Matter Mater. Phys.* **2002**, *66* (9), 1–8. https://doi.org/10.1103/PhysRevB.66.094410.

(31) Adamo, C.; Ke, X.; Wang, H. Q.; Xin, H. L.; Heeg, T.; Hawley, M. E.; Zander, W.; Schubert, J.; Schiffer, P.; Muller, D. A.; et al. Effect of Biaxial Strain on the Electrical and Magnetic Properties of (001) La0.7Sr0.3MnO3 Thin Films. *Appl. Phys. Lett.* **2009**, *95* (11). https://doi.org/10.1063/1.3213346.

(32) Thiele, C.; Dörr, K.; Bilani, O.; Rödel, J.; Schultz, L. Influence of Strain on the Magnetization and Magnetoelectric Effect in La0.7A0.3MnO3/PMN-PT (001) (A=Sr,Ca). *Phys. Rev. B - Condens. Matter Mater. Phys.* **2007**, *75* (5). https://doi.org/10.1103/PhysRevB.75.054408.

(33) Demidov, V. V.; Ovsyannikov, G. A.; Petrzhik, A. M.; Borisenko, I. V.; Shadrin, A. V.; Gunnarsson, R. Magnetic Anisotropy in Strained Manganite Films and Bicrystal Junctions. *J. Appl. Phys.* **2013**, *113* (16). https://doi.org/10.1063/1.4802659.

(34) Damodaran, A. R.; Lee, S.; Karthik, J.; MacLaren, S.; Martin, L. W. Temperature and Thickness Evolution and Epitaxial Breakdown in Highly Strained BiFeO3 Thin Films. *Phys. Rev. B - Condens. Matter Mater. Phys.* **2012**, *85* (2). https://doi.org/10.1103/PhysRevB.85.024113.

(35) Kubel, F.; Schmid, H. Structure of a Ferroelectric and Ferroelastic Monodomain Crystal of the Perovskite BiFeO3. *Acta Crystallogr. Sect. B* **1990**, *46* (6), 698–702. https://doi.org/10.1107/S0108768190006887.

(36) Zeches, R. J.; Rossell, M. D.; Zhang, J. X.; Hatt, A. J.; He, Q.; Yang, C. H.; Kumar, A.; Wang, C. H.; Melville, A.; Adamo, C.; et al. A Strain-Driven Morphotropic Phase Boundary in BifeO3. *Science (80-.).* **2009**, *326* (5955), 977–980. https://doi.org/10.1126/science.1177046.

(37) Christen, H. M.; Nam, J. H.; Kim, H. S.; Hatt, A. J.; Spaldin, N. A. Stress-Induced R-MA-MC-T Symmetry Changes in BiFeO3 Films. *Phys. Rev. B - Condens. Matter Mater. Phys.* **2011**, *83* (14). https://doi.org/10.1103/PhysRevB.83.144107.

(38) He, Q.; Chu, Y. H.; Heron, J. T.; Yang, S. Y.; Liang, W. I.; Kuo, C. Y.; Lin, H. J.; Yu, P.; Liang, C. W.; Zeches, R. J.; et al. Electrically Controllable Spontaneous Magnetism in Nanoscale Mixed Phase Multiferroics. *Nat. Commun.* **2011**, *2* (1). https://doi.org/10.1038/ncomms1221.

(39) You, L.; Chen, Z.; Zou, X.; Ding, H.; Chen, W.; Chen, L.; Yuan, G.; Wang, J. Characterization and Manipulation of Mixed Phase Nanodomains in Highly Strained BiFeO3 Thin Films. *ACS Nano* **2012**, *6* (6), 5388–5394. https://doi.org/10.1021/nn3012459.

(40) Béa, H.; Dupé, B.; Fusil, S.; Mattana, R.; Jacquet, E.; Warot-Fonrose, B.; Wilhelm, F.; Rogalev, A.; Petit, S.; Cros, V.; et al. Evidence for Room-Temperature Multiferroicity in a

Compound with a Giant Axial Ratio. *Phys. Rev. Lett.* **2009**, *102* (21). https://doi.org/10.1103/PhysRevLett.102.217603.

(41) Woo, C. S.; Lee, J. H.; Chu, K.; Jang, B. K.; Kim, Y. B.; Koo, T. Y.; Yang, P.; Qi, Y.; Chen, Z.; Chen, L.; et al. Suppression of Mixed-Phase Areas in Highly Elongated BiFeO3 Thin Films on NdAlO3 Substrates. *Phys. Rev. B - Condens. Matter Mater. Phys.* **2012**, *86* (5). https://doi.org/10.1103/PhysRevB.86.054417.

(42) Liu, H. J.; Liang, C. W.; Liang, W. I.; Chen, H. J.; Yang, J. C.; Peng, C. Y.; Wang, G. F.; Chu, F. N.; Chen, Y. C.; Lee, H. Y.; et al. Strain-Driven Phase Boundaries in BiFeO3 Thin Films Studied by Atomic Force Microscopy and x-Ray Diffraction. *Phys. Rev. B - Condens. Matter Mater. Phys.* **2012**, *85* (1). https://doi.org/10.1103/PhysRevB.85.014104.

(43) Infante, I. C.; Juraszek, J.; Fusil, S.; Dupé, B.; Gemeiner, P.; Diéguez, O.; Pailloux, F.; Jouen, S.; Jacquet, E.; Geneste, G.; et al. Multiferroic Phase Transition near Room Temperature in BiFeO3 Films. *Phys. Rev. Lett.* **2011**, *107* (23). https://doi.org/10.1103/PhysRevLett.107.237601.

(44) Chen, A.; Su, Q.; Han, H.; Enriquez, E.; Jia, Q. Metal Oxide Nanocomposites: A Perspective from Strain, Defect, and Interface. *Advanced Materials*. 2019. https://doi.org/10.1002/adma.201803241.

(45) Macmanus-Driscoll, J. L. Self-Assembled Heteroepitaxial Oxide Nanocomposite Thin Film Structures: Designing Interface-Induced Functionality in Electronic Materials. *Adv. Funct. Mater.* **2010**, *20* (13), 2035–2045. https://doi.org/10.1002/adfm.201000373.

(46) Chen, A.; Bi, Z.; Jia, Q.; Macmanus-Driscoll, J. L.; Wang, H. Microstructure, Vertical Strain Control and Tunable Functionalities in Self-Assembled, Vertically Aligned Nanocomposite Thin Films. *Acta Mater.* **2013**, *61* (8), 2783–2792. https://doi.org/10.1016/j.actamat.2012.09.072.

(47) Moshnyaga, V.; Damaschke, B.; Shapoval, O.; Belenchuk, A.; Faupel, J.; Lebedev, O. I.; Verbeeck, J.; Van Tendeloo, G.; Mücksch, M.; Tsurkan, V.; et al. Structural Phase Transition at the Percolation Threshold in Epitaxial (La0.7Ca0.3MnO3)1-x: (MgO)x Nanocomposite Films. *Nat. Mater.* **2003**, *2* (4), 247–252. https://doi.org/10.1038/nmat859.

(48) Harrington, S. A.; Zhai, J.; Denev, S.; Gopalan, V.; Wang, H.; Bi, Z.; Redfern, S. A. T.; Baek, S. H.; Bark, C. W.; Eom, C. B.; et al. Thick Lead-Free Ferroelectric Films with High Curie Temperatures through Nanocomposite-Induced Strain. *Nat. Nanotechnol.* **2011**, *6* (8), 491–495. https://doi.org/10.1038/nnano.2011.98.

(49) Lee, O.; Harrington, S. A.; Kursumovic, A.; Defay, E.; Wang, H.; Bi, Z.; Tsai, C. F.; Yan, L.; Jia, Q.; MacManus-Driscoll, J. L. Extremely High Tunability and Low Loss in Nanoscaffold Ferroelectric Films. *Nano Lett.* **2012**, *12* (8), 4311–4317. https://doi.org/10.1021/nl302032u.

(50) Yang, H.; Wang, H.; Zou, G. F.; Jain, M.; Suvorova, N. A.; Feldmann, D. M.; Dowden, P. C.; DePaula, R. F.; MacManus-Driscoll, J. L.; Taylor, A. J.; et al. Leakage Mechanisms of Self-Assembled (BiFeO3)0.5:(Sm2O3)0.5nanocomposite Films. *Appl. Phys. Lett.* **2008**. https://doi.org/10.1063/1.3000013.

(51) Fix, T.; Choi, E. M.; Robinson, J. W. A.; Lee, S. B.; Chen, A.; Prasad, B.; Wang, H.; Blamire, M. G.; Macmanus-Driscoll, J. L. Electric-Field Control of Ferromagnetism in a Nanocomposite via a ZnO Phase. *Nano Lett.* **2013**, *13* (12), 5886–5890. https://doi.org/10.1021/nl402775h.

(52) Liu, H. J.; Chen, L. Y.; He, Q.; Liang, C. W.; Chen, Y. Z.; Chien, Y. S.; Hsieh, Y. H.; Lin, S. J.; Arenholz, E.; Luo, C. W.; et al. Epitaxial Photostriction-Magnetostriction Coupled Self-Assembled Nanostructures. *ACS Nano* **2012**, *6* (8), 6952–6959. https://doi.org/10.1021/nn301976p.

(53) Harrington, S. A.; Durrell, J. H.; Maiorov, B.; Wang, H.; Wimbush, S. C.; Kursumovic, A.; Lee, J. H.; MacManus-Driscoll, J. L. Self-Assembled, Rare Earth Tantalate Pyrochlore Nanoparticles for Superior Flux Pinning in YBa2Cu3O7-δ Films. *Supercond. Sci. Technol.* **2009**, *22* (2). https://doi.org/10.1088/0953-2048/22/2/022001.

(54) Lee, S.; Sangle, A.; Lu, P.; Chen, A.; Zhang, W.; Lee, J. S.; Wang, H.; Jia, Q.; MacManus-Driscoll, J. L. Novel Electroforming-Free Nanoscaffold Memristor with Very High Uniformity, Tunability, and Density. *Adv. Mater.* **2014**, *26* (36), 6284–6289. https://doi.org/10.1002/adma.201401917.

(55) Su, Q.; Yoon, D.; Chen, A.; Khatkhatay, F.; Manthiram, A.; Wang, H. Vertically Aligned Nanocomposite Electrolytes with Superior Out-of-Plane Ionic Conductivity for Solid Oxide Fuel Cells. *J. Power Sources* **2013**, *242*, 455–463. https://doi.org/10.1016/j.jpowsour.2013.05.137.

(56) MacManus-Driscoll, J.; Suwardi, A.; Kursumovic, A.; Bi, Z.; Tsai, C. F.; Wang, H.; Jia, Q.; Lee, O. J. New Strain States and Radical Property Tuning of Metal Oxides Using a Nanocomposite Thin Film Approach. *APL Mater.* **2015**, *3* (6). https://doi.org/10.1063/1.4919059.

(57) Goldschmidt, V. M. Die Gesetze Der Krystallochemie. *Naturwissenschaften* **1926**, *14* (21), 477–485. https://doi.org/10.1007/BF01507527.

(58) Megaw, H. D. Crystal Structure of Double Oxides of the Perovskite Type. *Proc. Phys. Soc.* **1946**, *58* (2), 133–152. https://doi.org/10.1088/0959-5309/58/2/301.

(59) Jonker, G. H.; Van Santen, J. H. Ferromagnetic Compounds of Manganese with Perovskite Structure. *Physica* **1950**, *16* (3), 337–349. https://doi.org/10.1016/0031-8914(50)90033-4.

(60) Bednorz, J. G.; Müller, K. A. Possible High Tc Superconductivity in the Ba-La-Cu-O System. *Zeitschrift für Phys. B Condens. Matter* **1986**, *64* (2), 189–193. https://doi.org/10.1007/BF01303701.

(61) Von Helmolt, R.; Wecker, J.; Holzapfel, B.; Schultz, L.; Samwer, K. Giant Negative Magnetoresistance in Perovskitelike La2/3Ba1/3MnOx Ferromagnetic Films. *Phys. Rev. Lett.* **1993**, *71* (14), 2331–2333. https://doi.org/10.1103/PhysRevLett.71.2331.

(62) Greedan, J. E. The Rare Earth-Titanium (III) Perovskite Oxides-An Isostructural Series with a Remarkable Variation in Physical Properties. *J. Less-Common Met.* **1985**, *111* (1–2), 335–345. https://doi.org/10.1016/0022-5088(85)90207-3.

(63) Mochizuki, M.; Imada, M. Orbital Physics in the Perovskite Ti Oxides. *New J. Phys.* **2004**, *6*, 1–42. https://doi.org/10.1088/1367-2630/6/1/154.

(64) Zhou, H. D.; Goodenough, J. B. Localized or Itinerant TiO3 Electrons in RTiO3 Perovskites. *J. Phys. Condens. Matter* **2005**, *17* (46), 7395–7406. https://doi.org/10.1088/0953-8984/17/46/023.

(65) Varignon, J.; Grisolia, M. N.; Preziosi, D.; Ghosez, P.; Bibes, M. Origin of the Orbital and Spin Ordering in Rare-Earth Titanates. *Phys. Rev. B* **2017**, *96* (23). https://doi.org/10.1103/PhysRevB.96.235106.

(66) An, M.; Zhang, H. M.; Weng, Y. K.; Zhang, Y.; Dong, S. Possible Ferrimagnetism and Ferroelectricity of Half-Substituted Rare-Earth Titanate: A First-Principles Study on Y0.5La0.5TiO3. *Front. Phys.* **2016**, *11* (2). https://doi.org/10.1007/s11467-015-0535-4.

(67) Kubota, M.; Nakao, H.; Murakami, Y.; Taguchi, Y.; Iwama, M.; Tokura, Y. Orbital Ordering near a Mott Transition: Resonant x-Ray Scattering Study of the Perovskite Ti Oxides RTiO3 and LaTiO3.02 (R=Gd, Sm, Nd, and La). *Phys. Rev. B - Condens. Matter Mater. Phys.* **2004**, *70* (24), 1–8. https://doi.org/10.1103/PhysRevB.70.245125.

(68) Komarek, A. C.; Roth, H.; Cwik, M.; Stein, W. D.; Baier, J.; Kriener, M.; Bourée, F.; Lorenz, T.; Braden, M. Magnetoelastic Coupling in RTiO3(R=La,Nd,Sm,Gd,Y) Investigated with Diffraction Techniques and Thermal Expansion Measurements. *Phys. Rev. B - Condens. Matter Mater. Phys.* **2007**, *75* (22). https://doi.org/10.1103/PhysRevB.75.224402.

(69) Kumar, V. S.; Chukka, R.; Chen, Z.; Yang, P.; Chen, L. Strain Dependent Magnetocaloric Effect in La0.67Sr 0.33MnO3 Thin-Films. *AIP Adv.* **2013**, *3* (5). https://doi.org/10.1063/1.4807739.

(70) Takubo, K.; Shimuta, M.; Kim, J. E.; Kato, K.; Takata, M.; Katsufuji, T. Crossover Behavior of the Crystal Structure and the Relation to Magnetism in Perovskite RTiO3. *Phys. Rev. B - Condens. Matter Mater. Phys.* **2010**, *82* (2). https://doi.org/10.1103/PhysRevB.82.020401.

(71) Zhang, J. Y.; Jackson, C. A.; Raghavan, S.; Hwang, J.; Stemmer, S. Magnetism and Local Structure in Low-Dimensional Mott Insulating GdTiO 3. *Phys. Rev. B - Condens. Matter Mater. Phys.* **2013**, *88* (12). https://doi.org/10.1103/PhysRevB.88.121104.

(72) Need, R. F.; Isaac, B. J.; Kirby, B. J.; Borchers, J. A.; Stemmer, S.; Wilson, S. D. Octahedral Tilt Independent Magnetism in Confined GdTiO3 Films. *Appl. Phys. Lett.* **2018**, *112* (13). https://doi.org/10.1063/1.5016174.

(73) BROUS, J.; FANKUCHEN, I.; BANKS, E. RARE EARTH TITANATES WITH A PEROVSKITE STRUCTURE. *ACTA Crystallogr.* **1953**, *6* (1), 67–70. https://doi.org/10.1107/S0365110X53000156.

(74) Shafer, M. W. Preparation and Crystal Chemistry of Divalent Europium Compounds. *J. Appl. Phys.* **1965**, *36* (3), 1145–1152. https://doi.org/10.1063/1.1714142.

(75) McGuire, T. R.; Shafer, M. W.; Joenk, R. J.; Alperin, H. A.; Pickart, S. J. Magnetic Structure of EuTiO3. *J. Appl. Phys.* **1966**, *37* (3), 981–982. https://doi.org/10.1063/1.1708549.

(76) Chien, C. L.; DeBenedetti, S.; Barros, F. D. S. Magnetic Properties of EuTiO3, Eu2TiO4, and Eu3Ti2O7. *Phys. Rev. B* **1974**, *10* (9), 3913–3922. https://doi.org/10.1103/PhysRevB.10.3913.

(77) Millis, A. J. Lattice Effects in Magnetoresistive Manganese Perovskites. *Nature* **1998**, *392* (6672), 147–150. https://doi.org/10.1038/32348.

(78) Hill, N. A. Why Are There so Few Magnetic Ferroelectrics? *J. Phys. Chem. B* **2000**, *104* (29), 6694–6709. https://doi.org/10.1021/jp000114x.

(79) Martin, L. W.; Chu, Y. H.; Ramesh, R. Advances in the Growth and Characterization of Magnetic, Ferroelectric, and Multiferroic Oxide Thin Films. *Materials Science and Engineering R: Reports*. 2010, pp 89–133. https://doi.org/10.1016/j.mser.2010.03.001.

(80) Ryan, P. J.; Kim, J. W.; Birol, T.; Thompson, P.; Lee, J. H.; Ke, X.; Normile, P. S.; Karapetrova, E.; Schiffer, P.; Brown, S. D.; et al. Reversible Control of Magnetic Interactions by Electric Field in a Single-Phase Material. *Nat. Commun.* **2013**, *4*. https://doi.org/10.1038/ncomms2329.

(81) Lee, J. H.; Ke, X.; Podraza, N. J.; Kourkoutis, L. F.; Heeg, T.; Roeckerath, M.; Freeland, J. W.; Fennie, C. J.; Schubert, J.; Muller, D. A.; et al. Optical Band Gap and Magnetic

Properties of Unstrained EuTiO3 Films. *Appl. Phys. Lett.* **2009**, *94* (21). https://doi.org/10.1063/1.3133351.

(82) Geng, Y.; Lee, J. H.; Schlom, D. G.; Freeland, J. W.; Wu, W. Magnetic Inhomogeneity in a Multiferroic EuTiO3thin Film. *Phys. Rev. B - Condens. Matter Mater. Phys.* **2013**. https://doi.org/10.1103/PhysRevB.87.121109.

(83) Tanaka, K.; Fujita, K.; Maruyama, Y.; Kususe, Y.; Murakami, H.; Akamatsu, H.; Zong, Y.; Murai, S. Ferromagnetism Induced by Lattice Volume Expansion and Amorphization in EuTiO3 Thin Films. *J. Mater. Res.* **2013**. https://doi.org/10.1557/jmr.2013.60.

(84) Akamatsu, H.; Kumagai, Y.; Oba, F.; Fujita, K.; Murakami, H.; Tanaka, K.; Tanaka, I. Antiferromagnetic Superexchange via 3d States of Titanium in EuTiO3 as Seen from Hybrid Hartree-Fock Density Functional Calculations. *Phys. Rev. B - Condens. Matter Mater. Phys.* **2011**, *83* (21). https://doi.org/10.1103/PhysRevB.83.214421.

(85) Akamatsu, H.; Fujita, K.; Hayashi, H.; Kawamoto, T.; Kumagai, Y.; Zong, Y.; Iwata, K.; Oba, F.; Tanaka, I.; Tanaka, K. Crystal and Electronic Structure and Magnetic Properties of Divalent Europium Perovskite Oxides EuMO3 (M = Ti, Zr, and Hf): Experimental and First-Principles Approaches. *Inorg. Chem.* **2012**, *51* (8), 4560–4567. https://doi.org/10.1021/ic2024567.

(86) Mosca, D. H.; Vidal, F.; Etgens, V. H. Strain Engineering of the Magnetocaloric Effect in MnAs Epilayers. *Phys. Rev. Lett.* **2008**, *101* (12). https://doi.org/10.1103/PhysRevLett.101.125503.

(87) Shen, B. G.; Sun, J. R.; Hu, F. X.; Zhang, H. W.; Cheng, Z. H. Recent Progress in Exploring Magnetocaloric Materials. *Advanced Materials*. 2009, pp 4545–4564. https://doi.org/10.1002/adma.200901072.

(88) Warburg, E. Magnetische Untersuchungen. *Ann. Phys.* **1881**, *249* (5), 141–164. https://doi.org/10.1002/andp.18812490510.

(89) Smith, A. Who Discovered the Magnetocaloric Effect? Warburg, Weiss, and the Connection between Magnetism and Heat. *Eur. Phys. J. H* **2013**, *38* (4), 507–517. https://doi.org/10.1140/epjh/e2013-40001-9.

(90) Moya, X.; Kar-Narayan, S.; Mathur, N. D. Caloric Materials near Ferroic Phase Transitions. *Nature Materials*. 2014, pp 439–450. https://doi.org/10.1038/nmat3951.

(91) Giauque, W. F.; MacDougall, D. P. Attainment of Temperatures below 1°absolute by Demagnetization of Gd2(SO4)38H2O [12]. *Physical Review*. 1933, p 768. https://doi.org/10.1103/PhysRev.43.768.

(92) Brown, G. V. Magnetic Heat Pumping near Room Temperature. *J. Appl. Phys.* **1976**, *47* (8), 3673–3680. https://doi.org/10.1063/1.323176.

(93) Pecharsky, V. K.; Gschneidner, K. A. Giant Magnetocaloric Effect in Gd5(Si2Ge2). *Phys. Rev. Lett.* **1997**, *78* (23), 4494–4497. https://doi.org/10.1103/PhysRevLett.78.4494.

(94) Tishin, A. M.; Spichkin, Y. I. *The Magnetocaloric Effect and Its Applications*; 2016. https://doi.org/10.1887/0750309229.

(95) Von Ranke, P. J.; Alho, B. P.; Nóbrega, E. P.; De Sousa, V. S. R.; Alvarenga, T. S. T.; Carvalho, A. M. G.; De Oliveira, N. A. The Influence of Magnetic and Electric Coupling Properties on the Magnetocaloric Effect in Quantum Paraelectric EuTiO3. *J. Magn. Magn. Mater.* **2012**, *324* (7), 1290–1295. https://doi.org/10.1016/j.jmmm.2011.11.037.

(96) Dan'kov, S. Y.; Tishin, A.; Pecharsky, V.; Gschneidner, K. Magnetic Phase Transitions and the Magnetothermal Properties of Gadolinium. *Phys. Rev. B - Condens. Matter Mater. Phys.* **1998**, *57* (6), 3478–3490. https://doi.org/10.1103/PhysRevB.57.3478.

(97) Pecharsky, V. K.; Gschneidner, K. A. Tunable Magnetic Regenerator Alloys with a Giant Magnetocaloric Effect for Magnetic Refrigeration from ∼20 to ∼290 K. *Appl. Phys. Lett.* **1997**, *70* (24), 3299–3301. https://doi.org/10.1063/1.119206.

(98) Wada, H.; Tanabe, Y. Giant Magnetocaloric Effect of MnAs1-XSbx. *Appl. Phys. Lett.* **2001**, *79* (20), 3302–3304. https://doi.org/10.1063/1.1419048.

(99) Tegus, O.; Brück, E.; Buschow, K. H. J.; De Boer, F. R. Transition-Metal-Based Magnetic Refrigerants for Room-Temperature Applications. *Nature* **2002**, *415* (6868), 150–152. https://doi.org/10.1038/415150a.

(100) Hu, F. X.; Shen, B. G.; Sun, J. R.; Wu, G. H. Large Magnetic Entropy Change in a Heusler Alloy Ni52.6Mn23.1Ga24.3 Single Crystal. *Phys. Rev. B - Condens. Matter Mater. Phys.* **2001**, *64* (13). https://doi.org/10.1103/PhysRevB.64.132412.

(101) Krenke, T.; Duman, E.; Acet, M.; Wassermann, E. F.; Moya, X.; Manosa, L.; Planes, A. Inverse Magnetocaloric Effect in Ferromagnetic Ni-Mn-Sn Alloys. *Nat. Mater.* **2005**, *4* (6), 450–454. https://doi.org/10.1038/nmat1395.

(102) Krenke, T.; Duman, E.; Acet, M.; Wassermann, E. F.; Moya, X.; Mañosa, L.; Planes, A.; Suard, E.; Ouladdiaf, B. Magnetic Superelasticity and Inverse Magnetocaloric Effect in Ni-Mn-In. *Phys. Rev. B - Condens. Matter Mater. Phys.* **2007**, *75* (10). https://doi.org/10.1103/PhysRevB.75.104414.

(103) Sandeman, K. G.; Daou, R.; Özcan, S.; Durrell, J. H.; Mathur, N. D.; Fray, D. J. Negative Magnetocaloric Effect from Highly Sensitive Metamagnetism in CoMnSi1-x Gex. *Phys. Rev. B - Condens. Matter Mater. Phys.* **2006**, *74* (22). https://doi.org/10.1103/PhysRevB.74.224436.

(104) Trung, N. T.; Zhang, L.; Caron, L.; Buschow, K. H. J.; Brück, E. Giant Magnetocaloric Effects by Tailoring the Phase Transitions. *Appl. Phys. Lett.* **2010**, *96* (17). https://doi.org/10.1063/1.3399773.

(105) Fujieda, S.; Fujita, A.; Fukamichi, K. Large Magnetocaloric Effect in La(FexSi1-x) 13 Itinerant-Electron Metamagnetic Compounds. *Appl. Phys. Lett.* **2002**, *81* (7), 1276–1278. https://doi.org/10.1063/1.1498148.

(106) Babkin, E. V; Urinov, K. O. Anisotropic Magnetocaloric Effect in Thin Magnetic Films. *Sov. Phys. J.* **1989**, *32* (11), 899–902.

(107) Morelli, D. T.; Mance, A. M.; Mantese, J. V.; Micheli, A. L. Magnetocaloric Properties of Doped Lanthanum Manganite Films. *J. Appl. Phys.* **1996**, *79* (1), 373–375. https://doi.org/10.1063/1.360840.

(108) Mansanares, A. M.; Gandra, F. C. G.; Soffner, M. E.; Guimarães, A. O.; Da Silva, E. C.; Vargas, H.; Marin, E. Anisotropic Magnetocaloric Effect in Gadolinium Thin Films:

Magnetization Measurements and Acoustic Detection. *J. Appl. Phys.* **2013**, *114* (16). https://doi.org/10.1063/1.4826909.

(109) Miller, C. W.; Williams, D. V.; Bingham, N. S.; Srikanth, H. Magnetocaloric Effect in Gd/W Thin Film Heterostructures. In *Journal of Applied Physics*; 2010; Vol. 107. https://doi.org/10.1063/1.3335515.

(110) Maat, S.; Thiele, J. U.; Fullerton, E. E. Temperature and Field Hysteresis of the Antiferromagnetic-to-Ferromagnetic Phase Transition in Epitaxial FeRh Films. *Phys. Rev. B - Condens. Matter Mater. Phys.* **2005**, *72* (21). https://doi.org/10.1103/PhysRevB.72.214432.

(111) Kumar, V. S.; Chukka, R.; Chen, Z.; Yang, P.; Chen, L. Strain Dependent Magnetocaloric Effect in La0.67Sr0.33MnO3 Thin-Films. *AIP Adv.* **2013**, *3* (5). https://doi.org/10.1063/1.4807739.

(112) Moya, X.; Hueso, L. E.; Maccherozzi, F.; Tovstolytkin, A. I.; Podyalovskii, D. I.; Ducati, C.; Phillips, L. C.; Ghidini, M.; Hovorka, O.; Berger, A.; et al. Giant and Reversible Extrinsic Magnetocaloric Effects in La0.7Ca0.3MnO3 Films Due to Strain. *Nat. Mater.* **2013**, *12* (1), 52–58. https://doi.org/10.1038/nmat3463.

(113) Zhang, Q.; Thota, S.; Guillou, F.; Padhan, P.; Hardy, V.; Wahl, A.; Prellier, W. Magnetocaloric Effect and Improved Relative Cooling Power in (La 0.7Sr0.3MnO3/SrRuO3) Superlattices. *J. Phys. Condens. Matter* **2011**, *23* (5). https://doi.org/10.1088/0953-8984/23/5/052201.

(114) Belyea, D. D.; Santos, T. S.; Miller, C. W. Magnetocaloric Effect in Epitaxial La 0.56Sr0.44MnO3 Alloy and Digital Heterostructures. In *Journal of Applied Physics*; 2012; Vol. 111. https://doi.org/10.1063/1.3677670.

(115) Vandrangi, S. K.; Yang, J. C.; Zhu, Y. M.; Chin, Y. Y.; Lin, H. J.; Chen, C. Te; Zhan, Q.; He, Q.; Chen, Y. C.; Chu, Y. H. Enhanced Magnetocaloric Effect Driven by Interfacial Magnetic Coupling in Self-Assembled Mn3O4-La0.7Sr0.3MnO3 Nanocomposites. *ACS Appl. Mater. Interfaces* **2015**, *7* (48), 26504–26511. https://doi.org/10.1021/acsami.5b07585.

(116) Ellmer, K. Magnetron Sputtering of Transparent Conductive Zinc Oxide: Relation between the Sputtering Parameters and the Electronic Properties. *J. Phys. D. Appl. Phys.* **2000**, *33* (4). https://doi.org/10.1088/0022-3727/33/4/201.

(117) Kachlik, M.; MacA, K.; Goian, V.; Kamba, S. Processing of Phase Pure and Dense Bulk EuTiO3 Ceramics and Their Infrared Reflectivity Spectra. *Mater. Lett.* **2012**, *74*, 16–18. https://doi.org/10.1016/j.matlet.2012.01.055.

(118) Seshendra Reddy, C.; Ashoka Reddy, C.; Sivasankar Reddy, A.; Sreedhara Reddy, P. Investigations of LBMO Thin Films Deposited on Different Substrates by Electron Beam Evaporation. *Applied Nanoscience (Switzerland)*. 2016, pp 461–466. https://doi.org/10.1007/s13204-015-0462-2.

(119) Kumar, R.; Kumar, G.; Umar, A. Pulse Laser Deposited Nanostructured ZnO Thin Films: A Review. *Journal of Nanoscience and Nanotechnology*. 2014, pp 1911–1930. https://doi.org/10.1166/jnn.2014.9120.

(120) Eason, R. *Pulsed Laser Deposition of Thin Films: Applications-Led Growth of Functional Materials*; 2006. https://doi.org/10.1002/9780470052129.

(121) Bragg, W. H.; Bragg, W. L. The Reflection of X-Rays by Crystals. *Proc. R. Soc. LONDON Ser. A-CONTAINING Pap. A Math. Phys. CHARACTER* **1913**, *88* (604), 428. https://doi.org/10.1098/rspa.1913.0040.

(122) Nord, M.; Vullum, P. E.; MacLaren, I.; Tybell, T.; Holmestad, R. Atomap: A New Software Tool for the Automated Analysis of Atomic Resolution Images Using Two-Dimensional Gaussian Fitting. *Adv. Struct. Chem. Imaging* **2017**, *3* (1). https://doi.org/10.1186/s40679-017-0042-5.

(123) Lichtert, S.; Verbeeck, J. Statistical Consequences of Applying a PCA Noise Filter on EELS Spectrum Images. *Ultramicroscopy* **2013**, *125*, 35–42. https://doi.org/10.1016/j.ultramic.2012.10.001.

(124) Einstein, A. Über Einen Die Erzeugung Und Verwandlung Des Lichtes Betreffenden Heuristischen Gesichtspunkt. *Ann. Phys.* **1905**, *322* (6), 132–148. https://doi.org/10.1002/andp.19053220607.

(125) Khatkhatay, F.; Chen, A.; Lee, J. H.; Zhang, W.; Abdel-Raziq, H.; Wang, H. Ferroelectric Properties of Vertically Aligned Nanostructured BaTiO3-CeO2 Thin Films and Their Integration on Silicon. *ACS Appl. Mater. Interfaces* **2013**, *5* (23), 12541–12547. https://doi.org/10.1021/am403834k.

(126) Yashima, M.; Kobayashi, S. Positional Disorder of Oxygen Ions in Ceria at High Temperatures. *Appl. Phys. Lett.* **2004**, *84* (4), 526–528. https://doi.org/10.1063/1.1644053.

(127) Chtoun, E. H.; Hanebali, L.; Garnier, P. Analyse Par Diffraction Des Rayons X, Méthode de Rietveld, de La Structure Des Solutions Solides (1-x)A2Ti2O7-XFe2TiO5 A=Eu,Y. *Ann. Chim. Sci. des Mater.* **2001**, *26* (3), 27–32. https://doi.org/10.1016/S0151-9107(01)80057-X.

(128) Fujita, K.; Wakasugi, N.; Murai, S.; Zong, Y.; Tanaka, K. High-Quality Antiferromagnetic EuTiO3 Epitaxial Thin Films on SrTiO3 Prepared by Pulsed Laser Deposition and Postannealing. *Appl. Phys. Lett.* **2009**, *94* (6). https://doi.org/10.1063/1.3072598.

(129) Sun, Z.; Zhang, Q.; Li, Y.; Wang, H. Thermal Stable La2Ti2O7:Eu3+ Phosphors for Blue-Chip White LEDs with High Color Rendering Index. *J. Alloys Compd.* **2010**, *506* (1), 338–342. https://doi.org/10.1016/j.jallcom.2010.06.203.

(130) Henderson, N. L.; Baek, J.; Halasyamani, P. S.; Schaak, R. E. Ambient-Pressure Synthesis of SHG-Active Eu2Ti2O7 with a [110] Layered Perovskite Structure: Suppressing Pyrochlore Formation by Oxidation of Perovskite-Type EuTiO3. *Chem. Mater.* **2007**, *19* (8), 1883–1885. https://doi.org/10.1021/cm062934d.

(131) Kumar, S.; Prakash, R.; Choudhary, R. J.; Phase, D. M. Structural, Morphological And Electronic Properties Of Pulsed Laser Grown Eu2O3 Thin Films. In *2ND INTERNATIONAL CONFERENCE ON CONDENSED MATTER AND APPLIED PHYSICS (ICC-2017)*; Shekhawat, MS and Bhardwaj, S and Suthar, B, Ed.; AIP Conference Proceedings; AMER INST PHYSICS: 2 HUNTINGTON QUADRANGLE, STE 1NO1, MELVILLE, NY 11747-4501 USA, 2018; Vol. 1953. https://doi.org/10.1063/1.5032948.

(132) Watson, S. M.; Santos, T. S.; Borchers, J. A.; Moodera, J. S. Relationship between Tunnel Magnetoresistance and Magnetic Layer Structure in EuO-Based Tunnel Junctions Investigated Using Polarized Neutron Reflectivity. *J. Appl. Phys.* **2008**, *103* (7). https://doi.org/10.1063/1.2837873.

(133) Phani, K. K.; Niyogi, S. K. Elastic Modulus-Porosity Relation in Polycrystalline Rare-Earth Oxides. *J. Am. Ceram. Soc.* **1987**, *70* (12), C-362-C-366. https://doi.org/10.1111/j.1151-2916.1987.tb04920.x.

(134) Bessas, D.; Rushchanskii, K. Z.; Kachlik, M.; Disch, S.; Gourdon, O.; Bednarcik, J.; Maca, K.; Sergueev, I.; Kamba, S.; Ležaić, M.; et al. Lattice Instabilities in Bulk EuTiO3. *Phys. Rev. B - Condens. Matter Mater. Phys.* **2013**, *88* (14). https://doi.org/10.1103/PhysRevB.88.144308.

(135) Concas, G.; Dewhurst, J. K.; Sanna, A.; Sharma, S.; Massidda, S. Anisotropic Exchange Interaction between Nonmagnetic Europium Cations in Eu2O3. *Phys. Rev. B - Condens. Matter Mater. Phys.* **2011**, *84* (1). https://doi.org/10.1103/PhysRevB.84.014427.

(136) Yakel, H. L. A Refinement of the Crystal Structure of Monoclinic Europium Sesquioxide. *Acta Crystallogr. Sect. B Struct. Crystallogr. Cryst. Chem.* **1979**. https://doi.org/10.1107/s0567740879004167.

(137) Lee, S.; Zhang, W.; Khatkhatay, F.; Jia, Q.; Wang, H.; Macmanus-Driscoll, J. L. Strain Tuning and Strong Enhancement of Ionic Conductivity in SrZrO3-RE2O3 (RE = Sm, Eu, Gd, Dy, and Er) Nanocomposite Films. *Adv. Funct. Mater.* **2015**, *25* (27), 4328–4333. https://doi.org/10.1002/adfm.201404420.

(138) Akamatsu, H.; Kumagai, Y.; Oba, F.; Fujita, K.; Tanaka, K.; Tanaka, I. Strong Spin-Lattice Coupling through Oxygen Octahedral Rotation in Divalent Europium Perovskites. *Adv. Funct. Mater.* **2013**, *23* (15), 1864–1872. https://doi.org/10.1002/adfm.201202477.

(139) Anderson, P. W. Antiferromagnetism. Theory of Superexchange Interaction. *Phys. Rev.* **1950**, *79* (2), 350–356. https://doi.org/10.1103/PhysRev.79.350.

(140) Goodenough, J. B. Theory of the Role of Covalence in the Perovskite-Type Manganites [La,M(II)]MnO3. *Phys. Rev.* **1955**, *100* (2), 564–573. https://doi.org/10.1103/PhysRev.100.564.

(141) Kanamori, J. Superexchange Interaction and Symmetry Properties of Electron Orbitals. *J. Phys. Chem. Solids* **1959**, *10* (2–3), 87–98. https://doi.org/10.1016/0022-3697(59)90061-7.

(142) Anderson, P. W. Theory of Magnetic Exchange Interactions:Exchange in Insulators and Semiconductors. *Solid State Phys. - Adv. Res. Appl.* **1963**, *14* (C), 99–214. https://doi.org/10.1016/S0081-1947(08)60260-X.

(143) Lebedev, O. I.; Verbeeck, J.; Van Tendeloo, G.; Shapoval, O.; Belenchuk, A.; Moshnyaga, V.; Damashcke, B.; Samwer, K. Structural Phase Transitions and Stress Accommodation in (Formula Presented) Composite Films. *Phys. Rev. B - Condens. Matter Mater. Phys.* **2002**, *66* (10), 1–10. https://doi.org/10.1103/PhysRevB.66.104421.

(144) MacManus-Driscoll, J. L.; Zerrer, P.; Wang, H.; Yang, H.; Yoon, J.; Fouchet, A.; Yu, R.; Blamire, M. G.; Jia, Q. Strain Control and Spontaneous Phase Ordering in Vertical Nanocomposite Heteroepitaxial Thin Films. *Nat. Mater.* **2008**, *7* (4), 314–320. https://doi.org/10.1038/nmat2124.

(145) Miller, C. W.; Belyea, D. D.; Kirby, B. J. Magnetocaloric Effect in Nanoscale Thin Films and Heterostructures. *J. Vac. Sci. Technol. A Vacuum, Surfaces, Film.* **2014**, *32* (4), 040802. https://doi.org/10.1116/1.4882858.

(146) Lytle, F. W. X-Ray Diffractometry of Low-Temperature Phase Transformations in Strontium Titanate. *J. Appl. Phys.* **1964**, *35* (7), 2212–2215. https://doi.org/10.1063/1.1702820.

(147) Llordés, A.; Palau, A.; Gázquez, J.; Coll, M.; Vlad, R.; Pomar, A.; Arbiol, J.; Guzmán, R.; Ye, S.; Rouco, V.; et al. Nanoscale Strain-Induced Pair Suppression as a Vortex-Pinning Mechanism in High-Temperature Superconductors. *Nat. Mater.* **2012**, *11* (4), 329–336. https://doi.org/10.1038/nmat3247.

(148) Orihashi, T.; Nakamura, T.; Adachi, S.; Srivastava, A. Synthesis and Unique Photoluminescence Properties of Eu2Ti2O7 and Eu2TiO5. *J. Am. Ceram. Soc.* **2016**, *99* (9), 3039–3046. https://doi.org/10.1111/jace.14318.

(149) Li, W.; Zhao, R.; Wang, L.; Tang, R.; Zhu, Y.; Lee, J. H.; Cao, H.; Cai, T.; Guo, H.; Wang, C.; et al. Oxygen-Vacancy-Induced Antiferromagnetism to Ferromagnetism Transformation in Eu0.5Ba0.5TiO3-δ Multiferroic Thin Films. *Sci. Rep.* **2013**, *3*. https://doi.org/10.1038/srep02618.

(150) Li, W.; He, Q.; Wang, L.; Zeng, H.; Bowlan, J.; Ling, L.; Yarotski, D. A.; Zhang, W.; Zhao, R.; Dai, J.; et al. Manipulating Multiple Order Parameters via Oxygen Vacancies: The Case of Eu0.5Ba0.5TiO3-δ. *Phys. Rev. B* **2017**, *96* (11). https://doi.org/10.1103/PhysRevB.96.115105.

(151) Kresse, G.; Hafner, J. Ab Initio Molecular Dynamics for Liquid Metals. *Phys. Rev. B* **1993**, *47* (1), 558–561. https://doi.org/10.1103/PhysRevB.47.558.

(152) Kresse, G.; Furthmüller, J. Efficient Iterative Schemes for Ab Initio Total-Energy Calculations Using a Plane-Wave Basis Set. *Phys. Rev. B - Condens. Matter Mater. Phys.* **1996**, *54* (16), 11169–11186. https://doi.org/10.1103/PhysRevB.54.11169.

(153) Rushchanskii, K. Z.; Spaldin, N. A.; Leaić, M. First-Principles Prediction of Oxygen Octahedral Rotations in Perovskite-Structure EuTiO3. *Phys. Rev. B - Condens. Matter Mater. Phys.* **2012**, *85* (10). https://doi.org/10.1103/PhysRevB.85.104109.

(154) Crandles, D. A.; Desroches, B.; Razavi, F. S. A Search for Defect Related Ferromagnetism in SrTiO3. *J. Appl. Phys.* **2010**, *108* (5). https://doi.org/10.1063/1.3481344.

(155) Allieta, M.; Scavini, M.; Spalek, L. J.; Scagnoli, V.; Walker, H. C.; Panagopoulos, C.; Saxena, S. S.; Katsufuji, T.; Mazzoli, C. Role of Intrinsic Disorder in the Structural Phase Transition of Magnetoelectric EuTiO3. *Phys. Rev. B - Condens. Matter Mater. Phys.* **2012**, *85* (18). https://doi.org/10.1103/PhysRevB.85.184107.

(156) Shimamoto, K.; Hatabayashi, K.; Hirose, Y.; Nakao, S.; Fukumura, T.; Hasegawa, T. Full Compensation of Oxygen Vacancies in EuTiO3 (001) Epitaxial Thin Film Stabilized by a

SrTiO3 Surface Protection Layer. *Appl. Phys. Lett.* **2013**, *102* (4). https://doi.org/10.1063/1.4789778.

(157) Dilawar, N.; Varandani, D.; Pandey, V. P.; Kumar, M.; Shivaprasad, S. M.; Sharma, P. K.; Bandyopadhyay, a K. Structural Transition in Nanostructured Eu2O3 under High Pressures. *Journal of nanoscience and nanotechnology*. 2006.

(158) Padmanabhan, R.; Bhat, N.; Mohan, S. High-Performance Metal-Insulator-Metal Capacitors Using Europium Oxide as Dielectric. *IEEE Trans. Electron Devices* **2012**, *59* (5), 1364–1370. https://doi.org/10.1109/TED.2012.2188329.

(159) Pkaa, M. Magnetic Field Dependence of Magnetic Entropy Change in Nanocrystalline and Polycrystalline Manganites La1-XMxMnO3 (M=Ca,Sr). *J. Appl. Phys.* **2010**, *108* (11). https://doi.org/10.1063/1.3517831.

(160) Wang, X.; Zhen, S.; Min, Y.; Zhou, P.; Huang, Y.; Li, J.; Zhong, C.; Dong, Z. Magnetic Phase Transitions and Giant Magnetocaloric Effect of EuTiO3 Nanowires. *J. Alloys Compd.* **2016**, *689*, 63–68. https://doi.org/10.1016/j.jallcom.2016.07.305.

(161) Katsufuji, T.; Tokura, Y. Transport and Magnetic Properties of a Ferromagnetic Metal: Eu1-XRxTiO3. *Phys. Rev. B* **1999**, *60* (22), R15021–R15023. https://doi.org/10.1103/PhysRevB.60.R15021.

(162) Yoshii, K.; Mizumaki, M.; Nakamura, A.; Abe, H. Structure and Magnetism of Eu1-XDyxTiO3. In *Journal of Solid State Chemistry*; 2003; Vol. 171, pp 345–348. https://doi.org/10.1016/S0022-4596(02)00231-1.

(163) Wei, T.; Song, Q. G.; Zhou, Q. J.; Li, Z. P.; Qi, X. L.; Liu, W. P.; Guo, Y. R.; Liu, J. M. Cr-Doping Induced Ferromagnetic Behavior in Antiferromagnetic EuTiO3 Nanoparticles. *Appl. Surf. Sci.* **2011**, *258* (1), 599–603. https://doi.org/10.1016/j.apsusc.2011.07.129.

(164) Kususe, Y.; Murakami, H.; Fujita, K.; Kakeya, I.; Suzuki, M.; Murai, S.; Tanaka, K. Magnetic and Transport Properties of EuTiO3 Thin Films Doped with Nb. In *Japanese Journal of Applied Physics*; 2014; Vol. 53. https://doi.org/10.7567/JJAP.53.05FJ07.

(165) Li, L.; Zhou, H.; Yan, J.; Mandrus, D.; Keppens, V. Research Update: Magnetic Phase Diagram of EuTi1-XBxO3 (B = Zr, Nb). *APL Mater.* **2014**, *2* (11). https://doi.org/10.1063/1.4902137.

(166) Yamamoto, T.; Yoshii, R.; Bouilly, G.; Kobayashi, Y.; Fujita, K.; Kususe, Y.; Matsushita, Y.; Tanaka, K.; Kageyama, H. An Antiferro-to-Ferromagnetic Transition in EuTiO3-XHx Induced by Hydride Substitution. *Inorg. Chem.* **2015**, *54* (4), 1501–1507. https://doi.org/10.1021/ic502486e.

(167) Kugimiya, K.; Fujita, K.; Tanaka, K.; Hirao, K. Preparation and Magnetic Properties of Oxygen Deficient EuTiO3-δ Thin Films. *J. Magn. Magn. Mater.* **2007**, *310* (2 SUPPL. PART 3), 2268–2270. https://doi.org/10.1016/j.jmmm.2006.10.839.

(168) Grisolia, M. N.; Bruno, F. Y.; Sando, D.; Zhao, H. J.; Jacquet, E.; Chen, X. M.; Bellaiche, L.; Barthélémy, A.; Bibes, M. Structural, Magnetic, and Electronic Properties of GdTiO3 Mott Insulator Thin Films Grown by Pulsed Laser Deposition. *Appl. Phys. Lett.* **2014**, *105* (17). https://doi.org/10.1063/1.4899277.

(169) Heredia, A. R.; García, M. Q.; Mazariego, J. L. P.; Escamilla, R. X-Ray Diffraction and Raman Spectroscopy on Gd2(Ti 2-YTey)O7 Prepared at High Pressure and High Temperature. *J. Alloys Compd.* **2010**, *504* (2), 446–451. https://doi.org/10.1016/j.jallcom.2010.05.143.

(170) Sheu, H. S.; Shih, W. J.; Chuang, W. T.; Li, I. F.; Yeh, C. S. Crystal Structure and Phase Transitions of Gd(CO3)OH Studied by Synchrotron Powder Diffraction. *J. Chinese Chem. Soc.* **2010**, *57* (4 B), 938–945. https://doi.org/10.1002/jccs.201000130.

(171) Kreller, C. R.; Valdez, J. A.; Holesinger, T. G.; Mukundan, R.; Brosha, E. L.; Williamson, T.; Wang, Y. Q.; Uberuaga, B. P. Synthesis and Characterization of Dense Gd2Ti2O7 Pyrochlore Thin Films Deposited Using RF Magnetron Sputtering. *Solid State Ionics* **2018**, *314*, 36–40. https://doi.org/10.1016/j.ssi.2017.10.009.

(172) Pertosa, P.; Michel-Calendini, F. M. X-Ray Photoelectron Spectra, Theoretical Band Structures, and Densities of States for BaTiO3 and KNbO3. *Phys. Rev. B* **1978**. https://doi.org/10.1103/PhysRevB.17.2011.

(173) Nasser, S. A. X-Ray Photoelectron Spectroscopy Study on the Composition and Structure of BaTiO3 Thin Films Deposited on Silicon. *Appl. Surf. Sci.* **2000**, *157* (1–2), 14–22. https://doi.org/10.1016/S0169-4332(99)00495-X.

(174) Mizokawa, T.; Fujimori, A. Electronic Structure and Orbital Ordering in Perovskite-Type 3d Transition-Metal Oxides Studied by Hartree-Fock Band-Structure Calculations. *Phys. Rev. B - Condens. Matter Mater. Phys.* **1996**, *54* (8), 5368–5380. https://doi.org/10.1103/PhysRevB.54.5368.

(175) Mauger, A.; Godart, C. The Magnetic, Optical, and Transport Properties of Representatives of a Class of Magnetic Semiconductors: The Europium Chalcogenides. *Physics Reports*. 1986. https://doi.org/10.1016/0370-1573(86)90139-0.

(176) McGuire, T. R.; Shafer, M. W. Ferromagnetic Europium Compounds. *J. Appl. Phys.* **1964**. https://doi.org/10.1063/1.1713568.